
Deactivation mechanisms and timescales of nickel electrodes in alkaline water electrolysis

by

Lotte Vijverberg

to obtain the degree of Master of Science
at the Delft University of Technology,
to be defended on Monday January 22, 2023 at 12:15PM

Student number: 4753062
Project duration: May 2023 - January 2023
Thesis committee: Willem Haverkort Supervisor
David Vermaas
Ruud Kortlever



Acknowledgements

I would like to take this opportunity to express my sincere appreciation to those contributed to this thesis. Their guidance, support, and collaborative efforts over the past months have been of great value to me.

In particular, I would like to thank my supervisor, Dr. Ir. J. W. Haverkort, for his guidance and support throughout this project. Additionally, I would like to thank Araz for assisting with the setup and addressing my questions and Anamika for proofreading my thesis. I thank Emil, Hein, Gillis, Jeroen, and Dirk for their companionship and collaboration in the lab. But I also want to thank everyone in the Process and Energy Group for their contributions.

I appreciate the time and effort of my thesis committee, Dr. Ir. D. A. Vermaas and Dr. Ir. R. Kortlever, to review my work. I also thank Ruud Hendrikx and Kees Kwakernaak for their assistance with material analysis, Jacques from the Meetshop for helping with electrical questions, and all individuals at IWS for their support and collaboration.

Lastly, I am grateful to Marten for daily lunches and to Killian, my roommates, family, and other friends for their support during this project.

Abstract

Alkaline water electrolysis emerges as a promising technology for green hydrogen production, playing a significant role in global decarbonization. Nickel-based electrodes are widely used in alkaline water electrolysis due to their excellent catalytic properties for the hydrogen evolution reaction (HER) and oxygen evolution reaction (OER). However, nickel electrodes often experience a decrease in activity over time. Attempts of existing literature to investigate nickel deactivation employ conditions that differ from industry standards. Therefore, a more profound understanding of these phenomena under industry-relevant conditions is crucial for averting specific degradation pathways in future electrode design. This thesis investigates the deactivation phenomena and the timescales of untreated nickel electrodes during the OER and HER at 323 K and 30 wt% KOH, employing a current density of 1 A cm^{-2} . The electrolyte concentration and current density match industry standards, and the temperature aligns more with industrial practices than literature.

A simple electrolysis cell design facilitates this investigation. The experimental approach consists of two primary methodologies, each using fresh untreated nickel electrodes. The first consists of a constant current test of 2.5-hour followed by 15-minute rest, utilizing material analysis techniques before and after the test (X-ray fluorescence, scanning electron microscopy, and X-ray diffraction). The experiment was executed three times at a current density of 1 A cm^{-2} to validate reproducibility. Additionally, the test is repeated with current densities of 0.3 and 0.5 A cm^{-2} to investigate the effect of current density on electrode deactivation. The second methodology is the interval test, comprising 0.5-hour electrolysis periods at 1 A cm^{-2} combined with electrochemical characterization methods between the intervals (cyclic voltammetry, electrochemical impedance spectroscopy, and polarization curve analysis).

The constant current test reveals in 2.5 hours an increased overpotential of 0.19 V for the OER, which is still increasing after this period. The HER overpotential increases by 0.65 V and stabilizes after 20 minutes. The deactivation trend gradually increases, with a substantial potential jump occurring between 200 and 700 seconds, responsible for most deactivation. The overall trend in the performance of untreated nickel electrodes proves reproducible. At the different current densities, the deactivation trends align with the inserted charge density for the OER. For the HER, the timing is non-reproducible, but the deactivation extent is higher for increasing current densities. The interval test reveals that the deactivation is predominately recoverable for the OER and HER upon cycling between -1 and 3.1 V cell potential using cyclic voltammetry. Therefore, the primary deactivation is likely a redox reaction.

For the OER, no clear source for deactivation is found. The following explanation is mainly based on the literature review, which is in correspondence with the experimental data: The initial deactivation occurring within a subsecond timeframe is expected to be the formation of $\gamma \text{ NiOOH}$ from $\alpha \text{ Ni(OH)}_2$. Thickening of NiO layer is suggested to cause subsequent deactivation.

For the HER, a distinct cyclic voltammetry peak between -1.5 to -1.3 V vs. Hg/HgO forms after the electrolysis intervals. This peak links to the formation of beta nickel hydride based on literature, which is known to cause deactivation. A new equilibrium potential is also established after the electrolysis interval within a region similar to the peak. This shift is accompanied by a decreased exchange current density, signifying deactivation. Based on these findings and literature, the following deactivation sequence is proposed: The reduction of Ni(OH)_2 to less active metallic nickel together with hydrogen incorporation into the nickel lattice causes the first decrease in efficiency. A substantial potential jump between 200 and 700 seconds causes the major deactivation and is linked to the formation of β nickel hydride.

Contents

1	Introduction	1
1.1	Alkaline Water Electrolysis	2
1.2	Challenges of Nickel Electrodes during Alkaline Water Electrolysis	3
1.2.1	Voltage losses at Nickel Anodes	4
1.2.2	Voltage losses at Nickel Cathodes	5
1.2.3	General Voltage losses	6
1.3	Thesis Scope	7
1.4	Thesis Outline	8
2	Theory	9
2.1	AWE Fundamentals	9
2.1.1	Equilibrium Potential	9
2.1.2	Activation overpotential	10
2.1.3	Concentration Overpotential	10
2.1.4	Ohmic losses	11
2.2	HER	11
2.3	OER	12
2.4	Electrochemical Methods: CV	13
2.5	Electrochemical Methods: EIS	14
2.5.1	Impedance Response of an AWE cell	14
2.5.2	Conditions for good EIS measurements	16
3	Methodology	17
3.1	Preparation Setup	17
3.1.1	Electrode Design	17
3.1.2	Cell Design	18
3.1.2.1	Cell Container with Lid	20
3.1.2.2	Electrode-Diaphragm Configuration	20
3.1.3	Temperature Control	20
3.1.4	Data Acquisition	21
3.1.5	Data Acquisition Setup	21
3.1.5.1	Auxiliary Devices Settings	22
3.1.5.2	(Reference) Electrode Verification	23
3.2	Experiments	23
3.2.1	Galvanostatic Duration Tests	24
3.2.2	Interval Test	24
3.2.2.1	Cyclic Voltammetry	24
3.2.2.2	Tafel Analysis and EIS	24
3.2.3	Electrochemical Surface Characterization: SEM, XRF, and XRD	24
3.3	Data Processing	24
3.3.1	Treatment Individual Potential Data	25
3.3.2	EIS Processing	25
4	Results and Discussion	26
4.1	Reproducibility of Untreated Nickel Electrodes	26
4.2	Effect of high load (1 A cm^{-2}) on the Nickel Electrode Characteristics	29
4.2.1	Surface Characteristics: XRF	29
4.2.2	Surface Characteristics: SEM	30
4.2.3	Interval Test: Cyclic Voltammetry	32
4.2.3.1	Extraction Anodic and Cathodic CVs	32

4.2.3.2 Anode Deactivation Mechanism.	33
4.2.3.3 Cathode Deactivation Mechanism	34
4.2.4 Interval Test: Tafel Slopes	36
4.2.4.1 Extraction of Polarization Curves	36
4.2.4.2 Anode	37
4.2.4.3 Cathode	38
4.2.5 Interval Test: EIS	39
4.2.5.1 Validation and Fitting of Data	39
4.2.5.2 Ohmic Resistance	40
4.2.5.3 Anode Results	41
4.2.5.4 Cathode Results	42
4.2.6 Galvanostatic Long-Duration Tests	42
4.2.6.1 Anode Voltage-Time Development	42
4.2.6.2 Cathode Voltage-Time development	44
4.3 Effect of Current Density on the Voltage Losses over Time	46
4.3.1 Anode	46
4.3.2 Cathode	47
5 Conclusions and Recommendations	49
Bibliography	51
A Electrolyte Impurities	56
B Veco Electrode Specifications	57
C Problems with NI DAQ 6008	58
D Conversion of Reference Electrode Potentials	59
E Temperature of Results of Long-Duration Test	60
F Pourbaix Diagrams of Impurities	61
G XRD Results	64
H SEM Results	66
I Additional Electrochemical Results	67

Introduction

Since 2010, the National Oceanic and Atmospheric Administration has recorded the ten warmest years in the historical record [1]. The extensive use of fossil fuels and subsequent emission of greenhouse gases significantly contributes to the rising temperatures. We face the challenge of decarbonizing our worldwide energy consumption to mitigate further global temperature increases. Hydrogen emerges as a crucial player in global decarbonization, distinguished by its utilization without emitting greenhouse gases. As illustrated in Figure 1.1, hydrogen's substitutive potential is evident through its versatility in various use cases. As such, hydrogen can help decarbonize challenging industries such as iron, steel, cement, and chemicals [2]. It can also remedy the intermittent nature of renewable energy sources like wind and solar power, acting as an energy storage solution balancing the grid during surpluses and converting back to electricity during shortages. Additionally, hydrogen holds promise in long-distance transport, addressing challenges associated with battery range limitations [3].

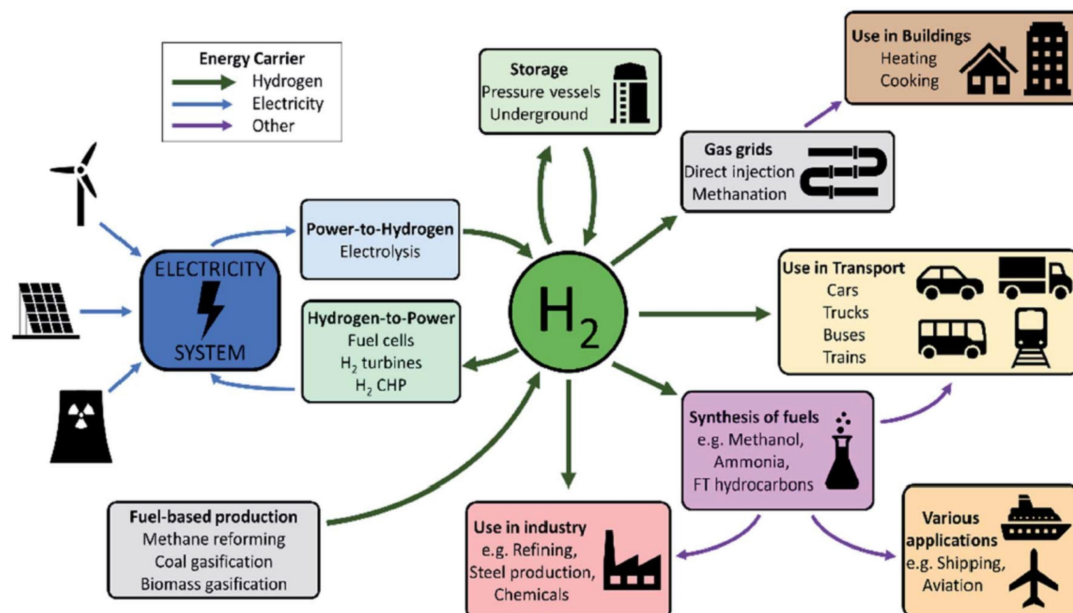


Figure 1.1: A schematic visualizing the various use cases of hydrogen. Source: Panchenko et al., 2023 [3].

Given hydrogen's various applications and promising nature, a significant increase in consumption is expected. However, only 5% of hydrogen is currently produced carbon-neutral, while the vast majority is still produced using fossil fuels. A prospective solution to this challenge is to expand the production of green hydrogen through water electrolysis. This process utilizes electricity generated from renewable sources, such as solar, wind, or hydropower, to split water into hydrogen and oxygen, as described by the following reaction [4]:



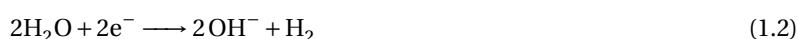
The primary hindrance to large-scale implementation of electrolysis is the 3 to 6 times higher production costs compared to hydrogen production through conventional fossil fuel-based methods. This increased cost is attributed mainly to the materials required to facilitate the electrolysis reaction [4]. The necessity for a highly corrosive alkaline or acidic environment, crucial for achieving high reaction efficiencies, restricts the choice of suitable materials [5]. Materials required for efficient hydrogen production in acidic environments are rare and

expensive, limiting widespread use. Conversely, in alkaline water electrolysis (AWE), less expensive and widely abundant materials, such as nickel and steel, can be effectively utilized. Nevertheless, each material presents challenges, including operation at lower currents per area, lower overall efficiencies, and stability issues. Despite these challenges, AWE is still considered a more economically viable option for scaling green hydrogen production [6, 7].

1.1. Alkaline Water Electrolysis

To be competitive with other hydrogen production methods, AWE aims to run at a current density of 1 A cm^{-2} [8]. Operating at a temperature of 80°C in a highly alkaline environment (25-30 wt% potassium hydroxide, KOH) helps mitigate losses [7]. The losses in AWE can come from different sources, and understanding these requires delving into the basics.

Figure 1.2 illustrates a simple AWE schematic with two electrodes submerged into an alkaline electrolyte connected to an external power supply. The power source gives the electrons enough energy to participate in the reactions. Electrons (e^-) flow from the negative terminal of the power source to the cathode, causing the reduction of water (H_2O) into hydrogen (H_2) and hydroxide ions (OH^-). The hydrogen evolution reaction (HER) is as follows:



The hydrogen gas forms bubbles that leave the electrolyte. Hydroxide ions move through the electrolyte to the anode, taking over the current transfer from electrons. Cations in the electrolyte move along with the negatively charged hydroxide anions to balance the charge. At the anode, they participate in the oxidation reaction, producing oxygen (O_2) and water. The oxygen evolution reaction (OER) is as follows:



The released electrons in the anode complete the circuit by flowing to the positive terminal of the power supply. Overall, more water molecules are consumed at the cathode than are produced at the anode, resulting in a net water consumption. The oxygen gas forms bubbles that leave the electrolyte. A diaphragm/separator prevents gas mixing while facilitating the passage of ions and water. Typically, such a diaphragm is made of ZrO_2 embedded in a polymer matrix due to its durability and high conductivity [9].

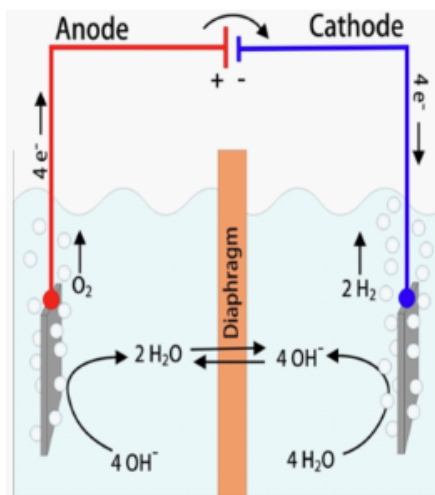


Figure 1.2: A schematic of alkaline water electrolysis. Water splits into hydrogen (H_2) and hydroxide ions (OH^-), which then produce oxygen (O_2) and water (H_2O). Source: Fraunhofer, n.d. [10].

1.2. Challenges of Nickel Electrodes during Alkaline Water Electrolysis

Nickel-based electrodes show potential in AWE applications due to their excellent catalytic properties for the HER [7, 11–13] and OER [6, 14, 15]. The AWE industry already utilizes nickel in the electrodes [16], given nickel's abundance and cost-effectiveness [7]. However, nickel electrodes present a significant challenge as their activity diminishes over time.

Deactivation becomes evident through either a current loss at a fixed electrode potential or an increase in potential at a constant current, particularly notable at the cathode [17–20]. Under certain polarizations, the cathode experiences a 50% decrease in current, stabilizing after a specific duration [21, 22]. The occurrence of distinct deactivation phenomena at various timescales becomes apparent in a constant potential experiment (Figure 1.3). Within the initial moments, a drop in current is quickly followed by stabilization, signifying the completion of a deactivation. After 200 seconds, the current suddenly drops, indicating a second deactivation, after which the current stabilizes again [23].

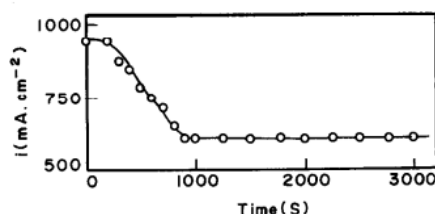


Figure 1.3: Current-time dependence plot at 325K for a nickel cathode after potentiostatic control at -1.40 V vs. Hg/HgO for 30 minutes. Source: Kibria et al., 1995 [23].

The deactivation of the anode is also observed [24, 25]. The deactivation mechanism is believed to depend on the current or potential application method, varying from linear sweeps to constant current/potential and pulses [24]. An overview of the various deactivation mechanisms of nickel electrodes, along with their corresponding timescales under industry-relevant conditions, is still lacking. Enhanced insights can guide electrode design to prevent such deactivation, boosting efficiency and making green hydrogen more competitive.

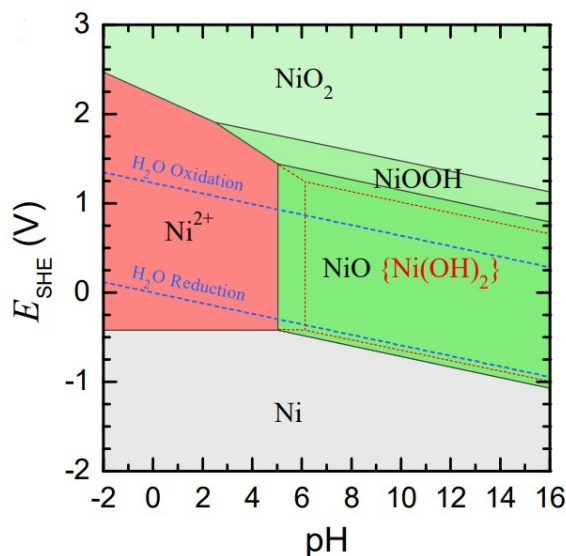


Figure 1.4: Electrode potential-pH Pourbaix diagrams of nickel in aqueous environment obtained from DFT simulations and verified with electrochemical experiments. Simulation conditions include a temperature of 298.15 K and a pressure of 1.0 bar. The red dashed lines indicate the $\text{Ni}(\text{OH})_2$ phase often found experimentally coexisting with NiO. Modified from source: Huang et al., 2017 [26].

A significant contribution to the still unknown deactivation mechanisms of nickel electrodes during water electrolysis is the various forms in which nickel can exist: metallic nickel (Ni), nickel oxides (NiO), nickel hydroxides ($\text{Ni}(\text{OH})_2$), nickel oxyhydroxides (NiOOH), and nickel hydrides (NiH_x). Upon exposure to air, a thin layer of NiO is formed on top of the nickel electrode [27, 28]. Medway et al. [28] found that this layer has a thickness of 2 to 4 atomic layers. When the nickel electrode is immersed in an alkaline hydrous solution, its behavior depends on the

applied potential and pH. Pourbaix phase diagrams are essential for illustrating the most stable phase depending on potential and pH (Figure 1.4). The diagram shows that the most stable compound is NiO when no potential is applied. Huang et al. [26] revealed thermodynamical blurring of phase boundaries with a phase probability analysis, meaning that multiple phases can exist simultaneously. This is in correspondence with the finding that part of the NiO layer is converted to Ni(OH)₂ when immersed in an alkaline hydrous solution [28].

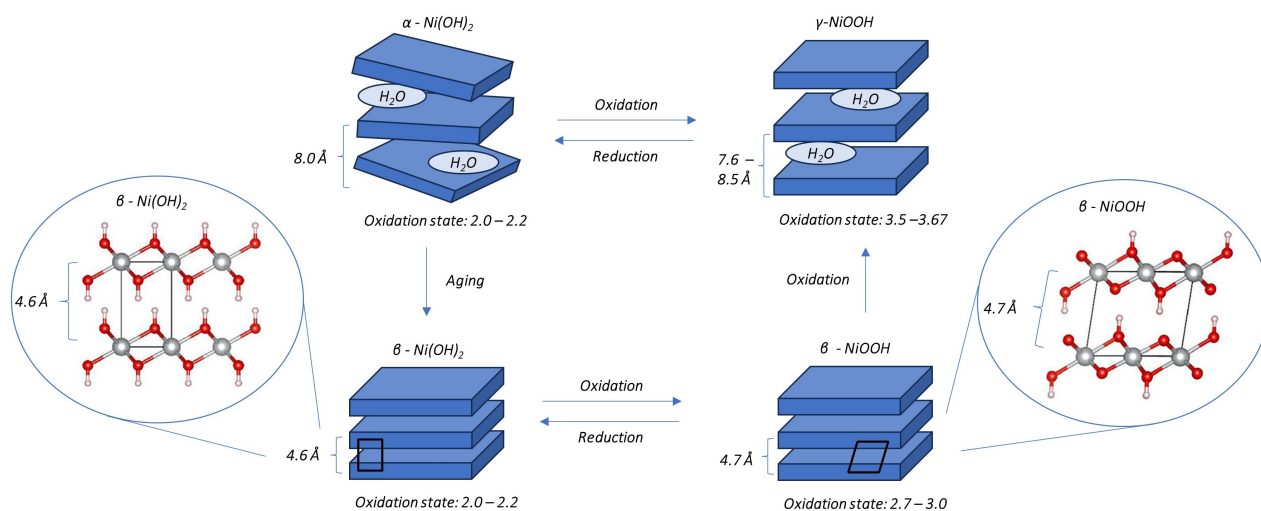


Figure 1.5: Schematic showing the behaviour of Ni(OH)₂ and NiOOH according to the Bode scheme. A zoomed-in schematic shows the Ni(OH)₂ and NiOOH lattice structure with silver, red and white atoms representing Ni^{2/3+}, O²⁻, and H⁺. The lattice structures are adapted from Tkalych et al., 2015 [29].

Figure 1.5 shows the structure of the morphologies of Ni(OH)₂. When the nickel electrode is immersed in an alkaline hydrous solution, part of the initially formed NiO layer gradually transforms Ni(OH)₂ with the alpha (α) crystalline structure. Layers of Ni(OH)₂ exhibit a hexagonal planar arrangement of Ni²⁺-oxygen octahedra. The layers are stacked in a relatively loose and disordered manner. The interlamellar distance, representing the spacing between the layers, is approximately 8 Å. The presence of water molecules between the layers is likely the cause of the relatively large interlamellar distance. During aging in alkaline electrolyte α -Ni(OH)₂ irreversibly undergoes dehydration, resulting in perfectly stacked Ni(OH)₂ layers with a decreased distance of 4.6 Å [30]. This transformation is typically observed at elevated temperatures, such as aging for 2 to 3 hours at 90°C. In contrast, one study shows no transformation after 16 hours at 22°C electrolyte [31].

Figure 1.6 shows a simplified schematic illustrating the behavior of the various forms before current insertion. Under the effect of applied current or potential, a spectrum of additional nickel phases is introduced, contributing to the intricate nature of the electrochemical response.

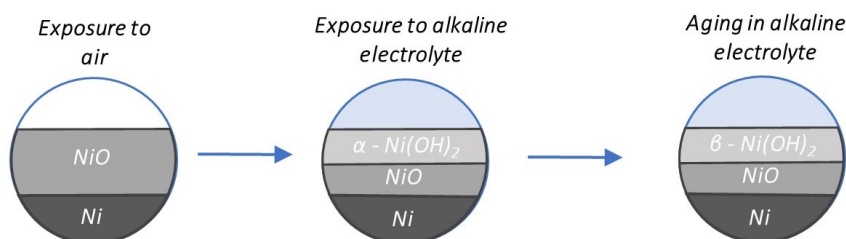


Figure 1.6: Schematic depicting the behavior of nickel under various conditions: exposure to air, immersion in alkaline electrolyte, and aging in alkaline electrolyte. This is a simplified representation, and multiple phases coexist rather than a single phase.

1.2.1. Voltage losses at Nickel Anodes

Voltage losses during the OER are mainly affected by redox transitions and thickening of the insulating NiO layer (Figure 1.7). At sufficiently anodic electrode potentials, the Ni(OH)₂ phase oxidizes to form NiOOH [28]. The Ni(OH)₂ phase determines the morphology of NiOOH, with β -Ni(OH)₂ producing β -NiOOH and α -Ni(OH)₂

producing gamma (γ)-NiOOH [27]. Overcharging β -NiOOH can also result in γ -NiOOH, which has a higher oxidation state [30] and intermellar distance [9]. This is explained by the increased amount of Ni^{4+} centers in γ -NiOOH [30]. The interplay between the four phases is often presented in the Bode scheme (Figure 1.5). While the Bode scheme is a useful simplification, it is important to note that multiple phases coexist rather than a single phase or compound.

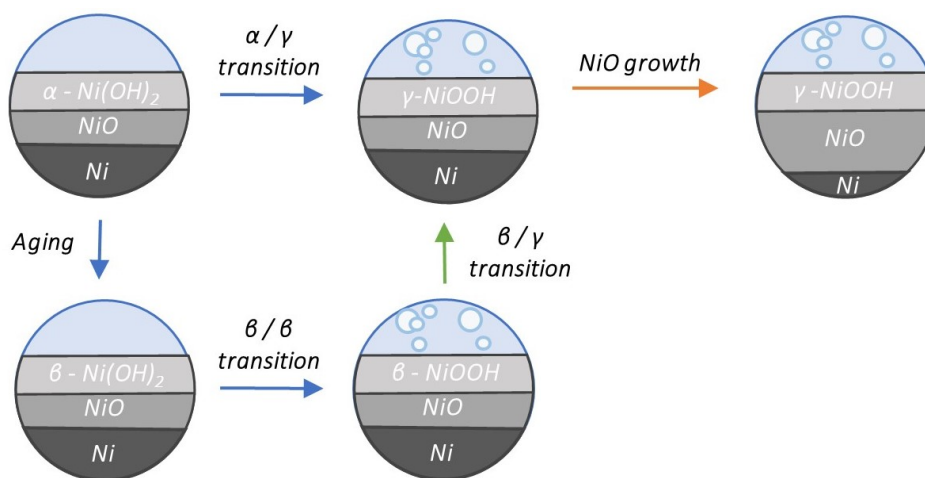


Figure 1.7: Schematic illustrating the behavior of nickel as an anode. Orange arrows indicate an increase in voltage losses, while green arrows represent a decrease. Blue arrows mean an uncertain effect on the voltage losses. This is a simplified representation, and multiple phases coexist rather than a single phase.

In the context of high current densities expected in industry, the formation of γ -NiOOH is likely regardless of the initial state, given the propensity for overcharging. The increased disorder in γ -NiOOH, compared to β -NiOOH, is suggested in the literature as a contributing factor to its enhanced activity towards the OER [32]. The activity towards the OER of $\text{Ni}(\text{OH})_2$ is less understood due to the conversion to NiOOH within this region. Figure 1.7 indicates transitions upon anodic polarizations between different phases that positively or negatively affect the potential, marked in green and orange arrows, respectively. The blue arrows indicate an uncertain effect.

A recent discovery has brought attention to a significant deactivation effect observed in extended galvanostatic tests, attributed to the thickening of the poorly conducting NiO layer [24]. Thickening of the NiO layer under linear potential sweeps over the $\text{Ni}(\text{OH})_2/\text{NiOOH}$ redox peak has already been recognized [27, 28]. It is hypothesized that this thickening of the compact inner oxide ultimately leads to a self-limiting oxide growth phenomenon [27].

1.2.2. Voltage losses at Nickel Cathodes

Voltage losses during the HER are attributed to the reduction of $\text{Ni}(\text{OH})_2$ and NiO to less active metallic nickel and the formation of NiH (Figure 1.8). NiO and $\text{Ni}(\text{OH})_2$ can be converted to metallic nickel upon exposure to cathodic polarization [28]. Diard et al. [21] observed that oxidized nickel exhibits greater activity towards the HER. Hence, the transition from oxidized forms to metallic nickel causes a decrease in efficiency, as indicated by the orange arrow in Figure 1.8.

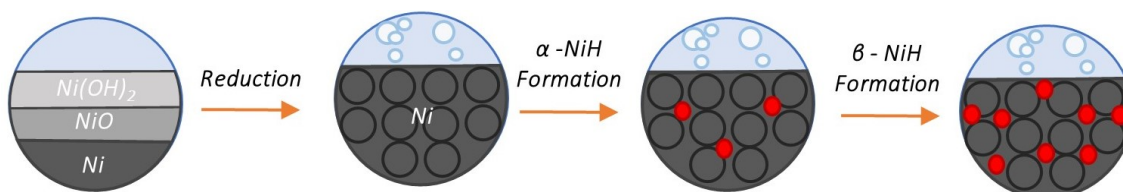


Figure 1.8: Schematic illustrating the behavior of nickel as a cathode. The orange arrow indicates an increase in voltage losses. The open black circles present Nickel atoms in a lattice structure. The red circles represent incorporated hydrogen atoms in the nickel lattice structure. This is a simplified representation, and multiple phases coexist rather than a single phase.

Long-term deactivation of nickel cathodes is attributed to hydrogen absorption into the metal lattice, forming NiH. The formation of hydrides under high-pressure conditions is already well known. Firstly, α -NiH is formed, consisting of a solid solution of atomic hydrogen in nickel with H/Ni smaller than 0.1. This phase can transform

into β -NiH with H/Ni larger than 0.6 [33]. The NiH system exhibits a significant hysteresis of about 300 MPa for the formation and decomposition of the hydride, possibly due to self-stress resulting from volume change and creation of dislocations [19]. Further hydrogen absorption at higher pressures continues through the dissolution of atomic hydrogen in the new hydride phase. A similar mechanism is suggested to occur under cathodic polarization [17, 20, 34–36].

Evidence of NiH formation under cathodic polarization has been collected through X-ray diffraction (XRD) patterns and electrochemical tests [17, 34]. Nickel cathodes displayed transient anodic currents at potentials still negative to the hydrogen reversible potential. These anodic currents are attributed to the decomposition of the hydride phase, resulting in the formation of metallic nickel and/or water and hydrogen. Furthermore, an additional experiment demonstrated a sustained H_2 evolution even after the current was switched off, providing further support for the hypothesis of hydride decomposition into hydrogen. Concurrently, a slow open potential decay persisted, remaining above the hydrogen evolution reaction equilibrium [35, 36].

The deactivation by hydrides is attributed to changes in the electronic structure. The incorporation of hydrogen into the nickel lattice causes the filling of the nickel d-band by the formation of nickel-hydrogen bonds. The catalytic activity for the HER rises with an increase in the number of d-band electrons but sharply decreases upon complete filling [17].

1.2.3. General Voltage losses

Beyond the voltage losses associated with the nickel material itself, there are several general losses:

- **Depletion of reactants:** Reaction concentrations within the electrolyte are uniform before initiating electrolysis. However, the onset of electrolysis can lead to the depletion of reactants near the electrode, resulting in reduced efficiency and increased potential. The reactants of the OER and HER are hydroxide ions and water, respectively (Equation 1.2 and 1.3). The depletion effect is expected to be minimal in industrial settings with high concentrations of both reactants [8].
- **Gas evolution effects:** At the beginning of electrolysis, the produced O_2 and H_2 dissolve into the electrolyte till saturation is reached. Since electrolysis typically operates beyond the reversible potential range, the increased product concentration has minimal impact on efficiency. However, the electrolyte saturation leads to the formation of gas bubbles, negatively impacting performance. Gas bubbles near the electrode can create a screening effect, expelling liquid reactants from the electrode surface, thereby increasing local current density. Additionally, the disruption of ion paths by bubbles increases the local current density in the electrolyte. These gas evolution effects manifest on a timescale of several seconds [37, 38].

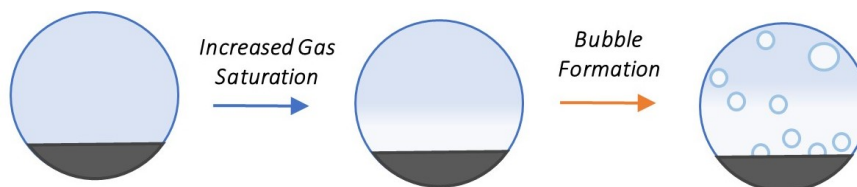


Figure 1.9: Schematic illustrating the effect of gas evolution during the moment of current insertion. The orange arrow indicates an increase in voltage losses of the reaction. Blue means an uncertain effect on the voltage losses. Note that gas saturation only negatively influences the performance at equilibrium conditions [8].

- **Double layer capacitance:** When an electric potential is applied during electrolysis, the cathode becomes negatively charged, and the anode becomes positively charged. To counteract these charges, ions from the electrolyte collect at the electrode surface, forming the double layer capacitance (typically $10\text{--}40 \mu F cm^{-2}$). The formation of these layers happens within the sub-millisecond range. This capacitance comprises distinct layers. The inner Helmholtz layer consists of solvent molecules (H_2O in aqueous solution) and contains specifically adsorbed species such as reaction products, reactants, and intermediates of the OER and HER. The outer Helmholtz layer mainly comprises solvated counter ions that neutralize the electrode charge. A diffuse layer of loosely alternating layers of anions and cations maintains charge neutrality throughout the double layers, accounting for the exponential decay of the potential away from the electrode. Beyond the diffuse layer is the bulk solution where the electrode's potential no longer affects the electrolyte structure [8].

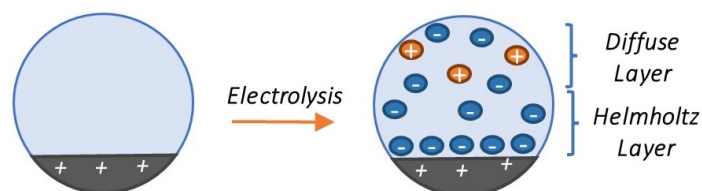


Figure 1.10: Schematic illustrating the electric double layer formation upon current insertion at the anode. The orange arrow indicates an increase in voltage losses of the reaction.

- Impurities:** Impurities in the nickel lattice can significantly alter the efficiency during water electrolysis. Impurities already present in the nickel lattice structure can leach out of the electrode. However, impurities present in the electrolyte can also be incorporated into the nickel lattice structure. The effect on the efficiency of the water-splitting reaction depends on the type of impurity. Iron impurities are noteworthy due to extensive research on their effects, as illustrated in Figure 1.11. However, the literature does not specify the exact time scale for these processes.

The presence of iron in nickel is known to improve the performance significantly during the OER. Even low concentrations of iron impurities have been found to affect the performance of $\text{Ni}(\text{OH})_2$ films [25, 32]. The method of polarization influences the fate of iron in the lattice structure, with iron uptake occurring in linear sweeps over the $\text{Ni}(\text{OH})_2/\text{NiOOH}$ redox peaks. Iron leaching is observed under constant polarization or on-off conditions, leading to decreased activity [24]. During the HER, iron deposits on top of the electrode can form, preventing hydride formation and thus deactivation [25, 39]. The polarization method likely influences this behavior similarly to what is observed in the OER. Iron dendrite formations are seen under constant current conditions followed by cycling [25]. In contrast, prolonged constant cathodic current tests revealed iron leaching [24].

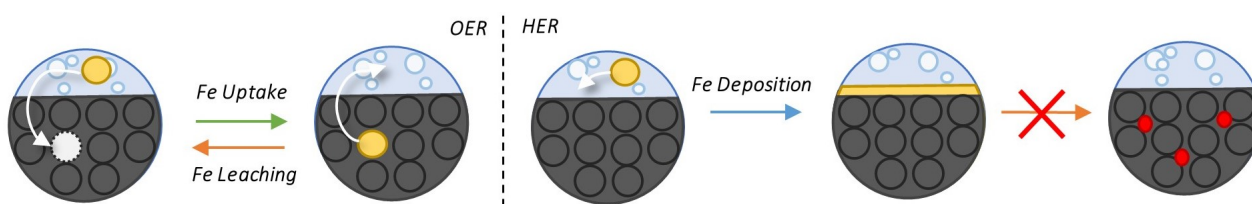


Figure 1.11: Schematic illustrating the effect of iron as an impurity on the performance during electrolysis. The orange arrow indicates an increase in voltage losses, while the green arrow represents a decrease. Blue means an uncertain effect. For the OER, iron can leach out or incorporate in the nickel lattice. For the HER, iron can deposit on top of the nickel to prevent NiH formation. It depends on the polarization method if the reactions are happening. The orange arrow indicates an increase in voltage losses, while the green arrow represents a decrease. Other types of impurities can have different effects on the voltage losses.

1.3. Thesis Scope

Nickel electrodes often exhibit a significant decrease in activity towards the OER and HER after extended electrolysis in alkaline conditions [17–20, 24]. The various potential deactivation mechanisms, ranging from intricate surface behaviors to more general voltage losses, each operating on its distinct timescale, complicate understanding the underlying processes. Moreover, existing knowledge about nickel deactivation often pertains to conditions at room temperature and lower electrolyte concentrations of typically around 1 M KOH. A more profound understanding of these phenomena under industry-relevant conditions is crucial for averting specific degradation pathways in future electrode design.

This thesis aims to provide an overview of various deactivation phenomena and their corresponding timescales of nickel anodes and cathodes. The emphasis will be on conditions relevant to industry practices, involving elevated temperatures, highly concentrated alkaline electrolyte (30 wt% KOH, 6 M KOH), and typical current densities of 1 A cm^{-2} .

Given the difficulty of achieving reproducible results with nickel, particular attention will be directed towards validating the test methods and setup. Whether the electrolyte exposure time is a significant factor to take into account will be investigated. Deactivation mechanisms will be studied through extended constant current (galvanostatic) tests lasting several hours. This investigation will be complemented by electrochemical characterization employing techniques such as Electrochemical Impedance Spectroscopy (EIS), Cyclic

Voltammetry (CV), and Tafel slope analysis. Surface analysis will be conducted using Scanning Electron Microscopy (SEM), X-ray Diffraction (XRD), and X-ray Fluorescence (XRF).

This leads to the main research questions:

- Can untreated, fresh nickel electrodes in alkaline water electrolysis yield reproducible results?
- What deactivation phenomena are observed in nickel electrodes during galvanostatic charging in alkaline water electrolysis at an industry-relevant current density of 1 A cm^{-2} ? What are the corresponding timescales of these deactivation phenomena?
- How does the current density impact the voltage losses of the anode and cathode over long-duration tests at industry-relevant current densities?

1.4. Thesis Outline

The report is organized into the following chapters:

- Chapter 2 delves into electrochemical fundamentals, OER and HER details, and laying the groundwork for understanding complex electrochemical characterization methods such as CV and EIS.
- Chapter 3 presents the methodology for preparing the test setup, extracting desired data, and processing the data. Electrochemical tests include galvanostatic tests, CV, and EIS, while surface characteristics are examined using XRD, XRF, and SEM.
- Chapter 4 discusses the results. The reproducibility of the method and setup is tested with a short and prolonged electrolyte exposure time. Additionally, various hypotheses related to deactivation phenomena are examined. The chapter concludes with a discussion of the impact of current density on voltage losses over time.
- Chapter 5 concludes the report with key findings, conclusions drawn from the results, and recommendations for future research.

2

Theory

This chapter establishes a foundational understanding of electrochemistry and electrochemical analysis methods. The goal is to provide a robust basis for comprehending the deactivation mechanism of nickel electrodes.

First, it delves into the fundamental principles of electrochemistry, explicitly focusing on elucidating the diverse types of voltage losses that may arise in AWE cells. Secondly, the discussion explores the characteristics of the HER and OER. Lastly, the chapter establishes a framework for comprehending complex electrochemical characterizations, focusing on CV and EIS. These advanced techniques will play a pivotal role in unraveling the complexities of electrode deactivation processes.

2.1. AWE Fundamentals

Understanding the diverse elements that contribute to the overall cell voltage is crucial for grasping the impact of a specific deactivation mechanism on cell voltage. The total cell voltage in an AWE cell arises from distinct sources, namely the equilibrium potential (E_{eq}), activation overpotential (η_{act}), concentration overpotential (η_{conc}), and ohmic losses (IR) [40]. The summation of these contributions yields the overall cell voltage:

$$E_{cell} \approx E_{eq} + \eta_{act} + \eta_{conc} + IR \quad (2.1)$$

Figure 2.1 illustrates how these losses depend on current density. The y-axis initiates from the equilibrium potential onward. In this example, bubble effects are considered independently despite their influence on the three distinct losses [37]. Subsequent sections will provide an in-depth exploration of each contribution outlined in Equation 2.1.

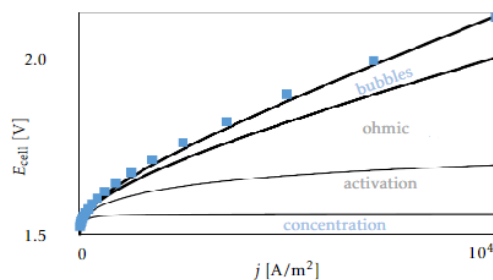


Figure 2.1: Graph depicting the potential dependencies on current density for the total cell voltage, encompassing concentration losses, activation losses, ohmic losses, and bubble losses in a zero-gap cell at room temperature. Source: Haverkort et al., 2021 [37].

2.1.1. Equilibrium Potential

Equilibrium thermodynamics determines the minimum voltage required to split water. No net current flow is present under these conditions, indicating the absence of concentration gradients that could cause irreversibilities. Even without net current flow, each electrode/electrolyte interface has a dynamic equilibrium, and the charges (electrons) cross this interface in both directions. The exchange current density (i_0) expresses this balanced faradaic activity. Calculating the equilibrium potential (E_{cell}°) for the overall water-splitting reaction involves deriving it from the change in Gibbs free energy at standard conditions (ΔG°) associated with the reaction:

$$E_{cell}^{\circ} \approx -\frac{\Delta G^{\circ}}{nF} \approx \frac{237}{2 \cdot 96485} \approx 1.23 \text{ V} \quad (2.2)$$

Here, n is the number of electrons exchanged per mole of product, and F is the Faraday constant (96485 C mol^{-1}), representing the charge of one mole of electrons. Operating the cell close to the equilibrium voltage results in an endothermic process, causing local cooling and absorbing heat from the surroundings. The reaction enthalpy (ΔH) considers the additional heat needed to bring the reaction products to the same temperature as the reactants:

$$\Delta H = \Delta G + T \cdot \Delta S \quad (2.3)$$

Here, ΔS is the entropy change of the reaction associated with the higher entropy of gases compared to liquids. Operating the cell at the "thermoneutral potential" of 1.48 V at room temperature causes the additional heat to dissipate internally. An exothermic reaction occurs in industrial settings where operation above the thermoneutral potential is typical. This reaction produces excess heat beyond what is strictly necessary for the chemical transformation to take place [8].

2.1.2. Activation overpotential

Many electrochemical reactions involve multiple subsequent steps where several electrons are transferred. Among these steps, a single electron transfer step is often more sluggish than others (rate-determining step), dictating the overall reaction kinetics. Within this view, the activation overpotential represents the additional potential needed to overcome the activation energy barrier of the rate-determining step. The widely used Butler-Volmer equation expresses the relationship of current density (i) and overpotential (η) [40]:

$$i = i_0 \left[\frac{C_R}{C_{R,eq}} \exp\left(\frac{\alpha F \eta}{RT}\right) - \frac{C_O}{C_{O,eq}} \exp\left(\frac{-(1-\alpha)F \eta}{RT}\right) \right] \quad (2.4)$$

Here, the transfer coefficient α indicates the symmetry of the energy barrier and usually falls between 0.3 and 0.7. $C_{O,eq}$ and $C_{R,eq}$ denote the surface concentrations of the reducing and oxidizing species in equilibrium, respectively. C_O and C_R resemble the deviating concentrations from equilibrium. The exchange current density (i_0), unlike rate constants in chemical reactions, is concentration-dependent and can be further expressed as:

$$i_0 = F k_0 C_{O,eq}^{(1-\alpha)} C_{R,eq}^{\alpha} \quad (2.5)$$

A high standard rate constant k_0 and i_0 system indicates a good catalyst, resulting in a low activation overpotential. Conversely, a system with low k_0 and i_0 has a high activation overpotential and requires more extreme potentials relative to E_{eq} to drive the reaction.

For larger η , the first or second term of the Butler-Volmer Equation 2.4 can be neglected depending on the sign of the current. For anodic currents, this leads to:

$$i = i_0 \frac{C_R}{C_{R,eq}} \exp\left(\frac{\alpha F \eta}{RT}\right) \quad (2.6)$$

When there are no appreciable concentration gradients throughout the cell, the concentration-independent Tafel equation can be obtained:

$$\eta_{act} = \frac{RT}{\alpha F} \ln(i_0) - \frac{RT}{\alpha F} \ln(i) = a + b \cdot \log(i) \quad (2.7)$$

Tafel behavior serves as an indicator of entirely irreversible kinetics with an effectively unidirectional faradaic process. The value for the Tafel slope (b) relates to a specific rate-determining step and is often used in the kinetics analysis. The Tafel slope b shown in Equation 2.7 has units V per dec and is equal to $\frac{2.3RT}{\alpha F}$ [8].

2.1.3. Concentration Overpotential

Concentration overpotentials represent potential differences arising from the concentration gradients near the electrode surface. At extremely low overpotentials, approaching equilibrium conditions results in the Nernst equation. The Nernst equation incorporates the concentrations of reactants and products near the electrode surface into the equilibrium potential and is given for single electron transfer by:

$$\eta_{conc} = \frac{RT}{F} \ln\left(\frac{C_{O,eq}}{C_{R,eq}}\right) \quad (2.8)$$

In irreversible kinetics at higher overpotentials, the Nernst equation does not apply. In these conditions, the neglected concentration gradient when deriving Equation 2.7 from Equation 2.6 provides information on the

concentration-dependent behavior. The following term adds in that case to the anodic overpotential considering a single electron transfer step:

$$\eta_{\text{conc}} = \frac{RT}{\alpha F} \ln \left(\frac{C_R}{C_{R, \text{eq}}} \right) \quad (2.9)$$

2.1.4. Ohmic losses

Ohmic losses in an electrochemical cell arise from ionic and electronic resistances within the cell and its setup. These resistances adhere to Ohm's law, representing the product of current and resistance ($I \cdot R$). The primary contributors to these losses are pathways with high current flow, such as the electrolyte region between the anode and cathode.

The electrolyte resistance originates from the hindrance hydroxide ions encounter during their journey through the electrolyte. The solution resistance R_{sol} (Ω) for a planar electrode usually arises because of the distance l (m) between the electrodes with area A (m^2) and the finite ionic conductivity κ ($\Omega^{-1} \text{m}^{-1}$) [8]:

$$R_{\text{sol}} = \frac{l}{\kappa A} \quad (2.10)$$

The conductivity of electrolyte can be approximated based on the KOH concentration c (M) and the temperature T (K) with the formula [41]:

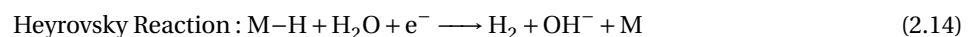
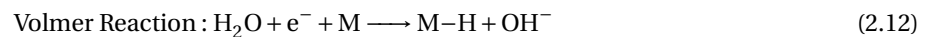
$$\kappa = -204c - 0.28c^2 + 0.5332cT + 20720cT + 0.1043c^3 - 310^{-5}c^2 T^2 \quad (2.11)$$

6.9 M KOH (30 wt%) at 323 K results in conductivity of $95.3 \Omega^{-1} \text{m}^{-1}$. An increase in gas (H_2 or O_2) concentrations in the electrolyte or the presence of bubbles can lead to an increase in solution resistance [37, 38].

The ohmic resistance also consists of other resistances from cables, electrodes, the diaphragm, and other connections. The measured cell potential is often corrected for the ohmic resistance (IR-corrected) to create a more accurate representation of the potential difference required to drive the electrolysis reaction.

2.2. HER

The cathodic reaction in AWE involves splitting water into hydrogen and hydroxide ions. The HER consists of the Volmer step, followed by the Heyrovsky or Tafel step. In alkaline conditions, the following equations describe the steps, where "M" represents the metal substrate and "M-H" denotes the adsorbed state:



The Volmer step involves the reduction of an adsorbed water molecule on the catalyst surface, yielding an adsorbed hydrogen atom and a hydroxide ion. Subsequently, the adsorbed hydrogen atom can either combine with another adsorbed hydrogen atom to generate a hydrogen molecule (Tafel step) or react with another water molecule to produce a hydrogen molecule and a hydroxide ion (Heyrovsky step) [40].

The specific mechanism depends on the electrode material and experimental conditions. The strength of the metal-hydrogen (M-H) bond helps predict the HER rate-determining step. Volcano plots illustrate the correlation between catalytic activity and M-H binding strength and offer valuable insights into the steps involved (see Figure 2.2). Platinum sits at the top of the volcano, indicating an optimal adsorption energy for catalytic performance. Metals on the right side of the plot are more likely to have desorption of H as the rate-determining step, meaning Heyrovsky or Tafel, due to their higher M-H bond energy. Conversely, metals on the left side of the volcano are more likely to have the Volmer step as the rate-determining step due to their lower M-H bond energy. Based on this theory, the HER rate-determining step on nickel is drawn to the Volmer step due to its position on the left side [42].

However, the HER mechanism on nickel varies with experimental conditions and applied potentials. Table 2.1 presents Tafel slopes that provide insights into the rate-determining step. Krstajic et al. [44] observed Tafel slopes of -121 mV per decade on nickel in 1 M NaOH at room temperature in the overpotential region exceeding -0.4 V (IR-corrected). Their findings align with the kinetics of the Volmer-Heyrovsky mechanism, with the latter serving as rate-limiting. Kreysa et al. [45] discovered similar Tafel slopes in a comparable potential region. The experiments at 50°C in 1 M KOH yielded slopes of -137 mV per decade for polycrystalline and -125 mV per decade for amorphous

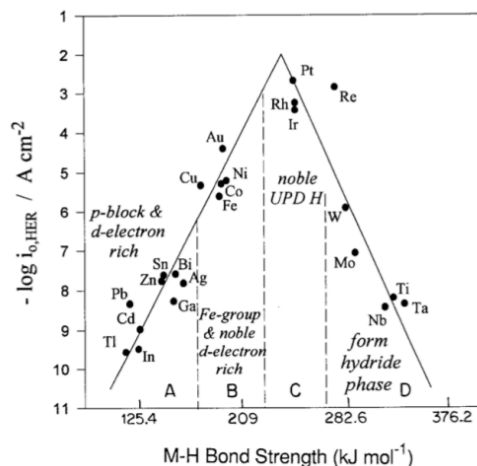


Figure 2.2: Comparison between M-H bond strength vs exchange current density for HER for different metals. Higher exchange current density equals a higher catalytic activity. Source: Mahmood et al., 2017 [42].

Rate determining step	Tafel slope (mV per dec) Increasing overpotential →
Volmer: Equation 2.12	120
Tafel: Equation 2.13	30
Heyrovsky: Equation 2.14	40 120

Table 2.1: Proposed theoretical tafel slopes for the reaction steps of the HER. Assumes increased adsorbed hydrogen surface coverage at higher overpotentials, with the Heyrovsky step shifting to 120 mV per dec tafel slope beyond a 0.6 surface coverage [43].

nickel electrodes. The data from this study supported a kinetic model based on the Volmer-Tafel steps. So, a clear consensus on the mechanism of nickel at higher overpotentials still needs to be made.

2.3. OER

The anodic OER is a crucial process in electrochemical water splitting. The most common pathway consists of the four-electron transfer mechanism, described in Equation 1.3. Similar to the HER, the OER involves multiple steps. Literature suggested the following mechanism of the OER, where "M" represents the metal oxide catalyst and "M-O" denotes the adsorbed state:



The assignment of Tafel slopes to specific rate-determining steps is a complex process influenced by multiple factors. Shinagawa et al. [43] proposed a model that considers the impact of potential on the reaction rate and the influence of different intermediate coverages on the electrocatalyst surface. They emphasized the necessity of a more nuanced model, cautioning against oversimplification that could lead to misinterpretation of results. The Tafel slopes demonstrate a general trend where higher overpotentials correspond to higher Tafel slopes (Table 2.2).

This observed increase in Tafel slope aligns with findings for nickel anodes, where a Tafel slope of 60 mV per dec is observed at low overpotentials (0.3 to 0.4 V), while at high overpotentials (> 0.5 V), it increases to 120 mV per

Rate determining step	Tafel slope (mV per dec)			
	Increasing overpotential →			
Equation 2.15	120			
Equation 2.16	30	120		
Equation 2.17	21	40	120	
Equation 2.18	22	30	60	120
Equation 2.19	22	40	120	

Table 2.2: Proposed theoretical tafel slopes for the reaction steps of the OER [43].

dec [27]. Additionally, the literature reports a reaction order of 1 regarding hydroxide ions, supporting the proposed mechanism [30, 46]. Moreover, the literature reveals various Tafel slopes for the OER on nickel, with values of 40 mV per dec [30] and 60 mV per dec [46] being observed. Different extents of iron in the nickel electrodes have been a source of the various Tafel slopes mentioned in the literature, where the effect became apparent in the last decade [32, 47, 48].

The complex kinetics of the OER on nickel anodes, dependent on surface characteristics and overpotential, can lead to changes in the reaction mechanism over time, complicating the understanding of voltage losses.

2.4. Electrochemical Methods: CV

Cyclic Voltammetry (CV) is a powerful electrochemical technique to probe reduction and oxidation processes of materials. CV involves sweeping the potential applied to an electrode linearly with time while measuring the resulting current. During this potential sweep, the system can undergo redox reactions, leading to changes in the current at the electrode surface. The cyclic nature allows for observing reversible redox processes. The plot of current versus applied potential (voltammogram) provides valuable insights into the electrochemical behavior of the system [49].

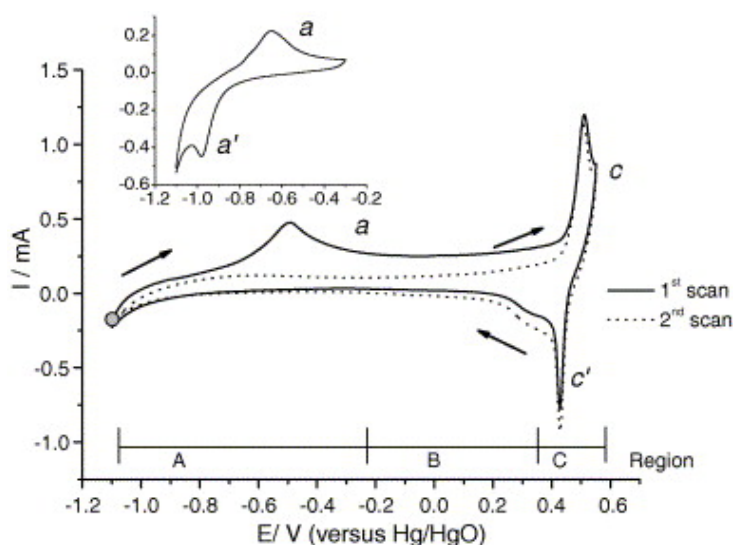


Figure 2.3: Cyclic voltammogram illustrating the behavior of nickel electrodes. Source: Medway et al., 2006 [28].

Voltammograms of nickel reveal distinctive peaks indicative of various redox processes. Figure 2.3 represents a voltammogram capturing the electrochemical behavior of nickel. Table 2.3 provides an overview of the redox reactions occurring at nickel electrodes, accompanied by their respective potentials. These potentials are predominantly derived from experiments conducted at room temperature in a 1 M KOH solution. Potentials highlighted in red signify oxidative currents, whereas those in blue denote reductive ones.

Reaction	E Hg/HgO	Notes
$\beta\text{NiOOH} - \longrightarrow \gamma\text{NiOOH} + x e^-$	0.7	Ni ³⁺ to Ni ^{3+/4+} [32].
$\text{NiO}(\text{OH})_2 + 2\text{OH}^- \longrightarrow \text{NiOO}_2 + 2\text{H}_2\text{O} + 2e^-$	0.6	Ni ²⁺ to Ni ⁴⁺ ; speculated formation of Ni ⁴⁺ in γ NiOOH phase [32, 50].
$\alpha\text{Ni}(\text{OH})_2 + \text{OH}^- \longrightarrow \gamma\text{NiOOH} + \text{H}_2\text{O} + e^-$	0.54	Ni ²⁺ to Ni ^{3+/4+} (peak c) [32].
$\beta\text{Ni}(\text{OH})_2 + \text{OH}^- \longrightarrow \beta\text{NiOOH} + \text{H}_2\text{O} + e^-$	0.48	Ni ²⁺ to Ni ³⁺ (peak c) [32].
$\gamma\text{NiOOH} + \text{H}_2\text{O} + e^- \longrightarrow \alpha\text{Ni}(\text{OH})_2 + \text{OH}^-$	0.44	Ni ^{3+/4+} to Ni ²⁺ (peak c') [27].
$\beta\text{NiOOH} + \text{H}_2\text{O} + e^- \longrightarrow \beta\text{Ni}(\text{OH})_2 + \text{OH}^-$	0.34	Ni ³⁺ to Ni ²⁺ (peak c') [27].
OER: $4\text{OH}^- \longrightarrow \text{O}_2 + 2\text{H}_2 + 4e^-$	0.173	OER equilibrium potential at 50 °C and 30 wt% KOH (see Appendix D for more details).
$\alpha\text{Ni}(\text{OH})_2 \longrightarrow \beta\text{Ni}(\text{OH})_2$	-0.2 - 0.3	No redox reaction; observed during aging in alkaline electrolyte and anodic sweeping through this region [28, 31].
$\text{Ni} + 2\text{OH}^- \longrightarrow \text{NiO} + \text{H}_2\text{O} + 2e^-$	0.05	Ni to Ni ²⁺ [51].
$\text{Ni} + 2\text{OH}^- \longrightarrow \alpha\text{Ni}(\text{OH})_2 + 2e^-$	-0.6	Ni to Ni ²⁺ (peak a) [27].
$\alpha\text{NiH} + x \text{OH}^- \longrightarrow \text{Ni} + x \text{H}_2\text{O} + x e^-$	-0.84 *	Ni ⁻ to Ni; speculated to cause the observed large hysteresis at more positive potentials than -0.84 V vs. Hg/HgO after extended polarization at -1.42 V vs. Hg/HgO [44]. The reaction can occur in either a reductive or oxidative manner [36].
$\alpha\text{NiH} + x \text{H}_2\text{O} + x e^- \longrightarrow \text{Ni} + \text{H}_2 + x \text{OH}^-$	-0.84 *	
$\alpha\text{Ni}(\text{OH})_2 + 2e^- \longrightarrow \text{Ni} + 2\text{OH}^-$	-1.0	Ni ²⁺ to Ni (peak a'); speculated that only the α , and not the β phase can be reduced [28].
HER: $2\text{H}_2\text{O} + 2e^- \longrightarrow 2\text{OH}^- + \text{H}_2$	-1.052 *	HER equilibrium potential at 50 °C and 30 wt% KOH (see Appendix D for more details).
$\text{Ni} + x \text{H}_2\text{O} + x e^- \longrightarrow \alpha\text{NiH} + x \text{OH}^-$	-1.2 *	Ni to Ni ⁻ ; 0.13 V more negative than the HER potential [33, 51].
$\beta\text{NiH} + x \text{OH}^- \longrightarrow \text{Ni} + x \text{H}_2\text{O} + x e^-$	>-1.3 *	Ni ⁻ to Ni; speculated to decompose at a less negative potential than the formation potential of β NiH. The reaction can occur in either a reductive or oxidative manner [36].
$\beta\text{NiH} + x \text{H}_2\text{O} + x e^- \longrightarrow \text{Ni} + \text{H}_2 + x \text{OH}^-$	>-1.3 *	
$\text{Ni} + x \text{H}_2\text{O} + x e^- \longrightarrow \beta\text{NiH} + x \text{OH}^-$	-1.3 *	Ni to Ni ⁻ ; speculated to cause the observed large hysteresis at more negative potentials than -1.3 V vs. Hg/HgO [44].

Table 2.3: Overview of the redox processes of nickel in alkaline conditions, mainly in 1 M KOH. Oxidative reactions are highlighted in red, and reductive reactions are highlighted in blue. All potentials are based on the mercury oxide (Hg/HgO) electrode standard. For details on converting reference electrode potentials from other studies to the Hg/HgO standard, see Appendix D. * Although specific values for these potentials are not directly mentioned in the literature, they are deduced based on observations from previous studies.

2.5. Electrochemical Methods: EIS

Electrochemical Impedance Spectroscopy (EIS) is a technique used to characterize the behavior of electrochemical systems by perturbing them with sinusoidal signals and analyzing their response. EIS provides insights into various electrochemical processes, such as charge transfer reactions and adsorption/desorption phenomena. This section considers the impedance response of an AWE cell and lists the conditions for reliable impedance measurements. The book 'Electrochemical Impedance Spectroscopy and its Applications' [52] and an EIS tutorial [53] provide the concepts used.

2.5.1. Impedance Response of an AWE cell

Impedance is the opposition to electrical flow and has a real (Z') frequency-independent part and an imaginary (Z'') part that varies with frequency. When an alternating voltage signal is applied (Equation 2.20), the resulting current has a similar frequency ω . However, the current is shifted by the angle ϕ concerning the voltage signal (Equation 2.21). Equation 2.22 shows the impedance calculation. Using Euler's formula, $e^{ix} = \cos(x) + i\sin(x)$, impedance can be expressed as a complex equation, where i is the imaginary unit, $i^2 = -1$.

$$V = V_0 \cos(\omega t) = V_0 e^{i\omega t} \quad (2.20)$$

$$I = I_0 \cos(\omega t + \phi) = I_0 e^{i\omega t} e^{i\phi} \quad (2.21)$$

$$Z = \frac{V}{I} = \frac{V_0 e^{i\omega t}}{I_0 e^{i\omega t} e^{i\phi}} = \frac{V_0}{I_0} e^{-i\phi} = |Z| (\cos(\phi) + i \sin(\phi)) = Z' + iZ'' \quad (2.22)$$

The AWE cell's impedance response mirrors the behaviors seen in resistors and capacitors. Therefore, an equivalent circuit can be constructed to represent this behavior. The impedance response of these components is first discussed before exploring the overall AWE cell behavior:

- **Resistor (R)**

In DC circuits, only resistors oppose the flow of current. Ohm's law defines resistance as:

$$R = \frac{V}{I} \quad (2.23)$$

In AC circuits, the impedance response of a resistor remains unaffected by frequency, leading to a purely real impedance equal to the resistance:

$$Z_R = R \quad (2.24)$$

- **Capacitor (C)**

Capacitors block constant current flow but store electrical charge q based on the applied voltage and capacitance:

$$q = CV \quad (2.25)$$

The AC opposition presented by capacitors is called reactance. Reactance shares the same units as resistance. When an AC opposition is applied to a capacitor, the resulting response is due to the change of the stored charge. The impedance expression for a capacitor is:

$$Z_C = \frac{1}{2\pi fC} \quad (2.26)$$

This implies that the imaginary part varies inversely with frequency while the real impedance remains zero.

The most straightforward impedance representation of an AWE cell's electrode/electrolyte interface combines parallel ideal capacitors and resistors. The ideal capacitor models the double-layer charging and an ideal resistor accounts for charge transfer reactions. This combination will be referred to as a RC circuit with its characteristics time constant τ , which follows from the multiplication of the resistance with the capacitance.

Furthermore, introducing an ohmic resistance in series captures the linear scaling of resistances with current. This ohmic resistance accounts for ion and electron conduction within the entire cell, involving processes such as the movement of hydroxide ions and electron transfer within electrodes and cables. Figure 2.4 depicts the resulting equivalent circuit and its typical response. In the following paragraphs the impedance response will be discussed using the Nyquist plot, mapping Z'' against Z' for different excitation frequencies.

At frequencies approaching infinity, the capacitive reactance tends to zero. So, the current can freely pass through the capacitor in the RC circuit. Thus, only the ohmic resistance (R_0) is measured at frequencies approaching infinity.

Traversing to lower frequencies, the capacitive reactance of the RC circuit with the lowest time constant becomes larger. Simultaneously, the current passes through both the capacitor (C_1) and the resistor (R_1). The characteristic frequency, equal to the reciprocal of the time constant, is where the reactance equals the resistance, resulting in the maximum imaginary part of the impedance.

Further decreasing frequency reaches a point where the frequency is much lower than the characteristic frequency of the RC circuit. At this stage, the current for the RC circuit seems stable, resulting in all the current passing through the resistor. The intercept equals to $R_0 + R_1$ in that case. The reasoning above also applies to the RC circuit with a higher time constant, giving rise to a second semicircle in the Nyquist plot. When the time constants of the RC circuits are similar, the semicircles may merge. The merging of semicircles complicates the impedance interpretation and parameter extraction process.

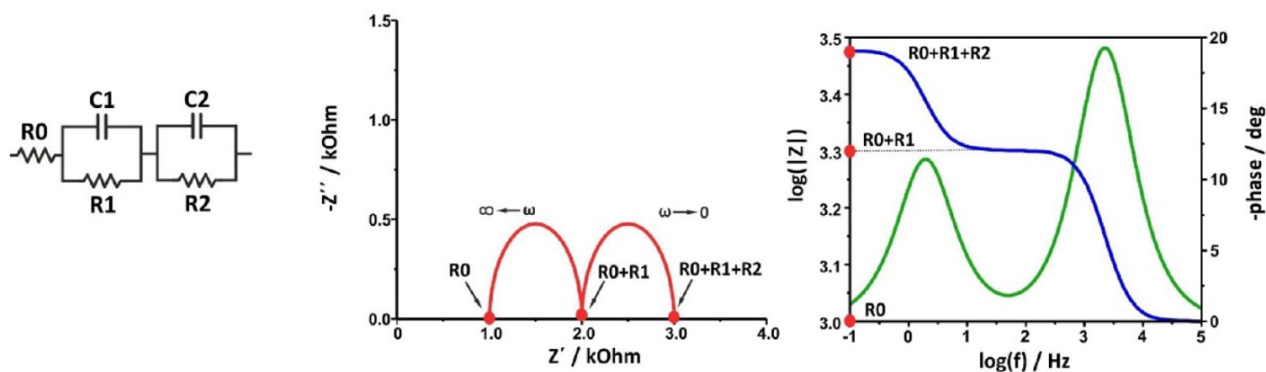


Figure 2.4: Simple electrolysis cell equivalent circuit (left) alongside Nyquist (middle) and Bode magnitude and phase angle plots (right). R_0 denotes the ohmic resistance, while R_1 and R_2 represent the charge transfer resistances of electrodes with the lowest and highest RC time constants, respectively. The capacitors C_1 and C_2 depict the double-layer capacitors associated with their respective electrodes. All resistances are one k Ω . Source: Lazanas et al., 2023 [53].

2.5.2. Conditions for good EIS measurements

A great benefit of EIS is the ability to determine the quality of the obtained data. Kramers-Kronig relations are often used to evaluate the data quality of complex functions. The real part of the impedance can be obtained by integrating the imaginary part and vice versa. The relations demand integration from 0 to infinity, which is experimentally impossible. Various methods have been proposed to carry out the relations in practice [54, 55]. The data is formally correct and Kramers-Kronig compliant when the results from the calculation agree with the experimental data. For these relations to yield reliable insights, specific criteria must be fulfilled, emphasizing the linear time invariance of the system.

Linearity: A prerequisite for EIS measurements is establishing pseudo-linear behavior. While specific electrochemical processes, such as Butler-Volmer kinetics, introduce nonlinearity, small-amplitude perturbations can be carefully selected to yield an approximate linear response. This approach focuses on a zoomed-in region of the I-V curve where linearity is approached.

Causality: Ensuring a time-invariant response is crucial in EIS measurements. The system's behavior should exhibit an exclusive cause-and-effect relationship between the applied perturbation and the resulting response. External factors, such as bubbles formed during water electrolysis or electrical noise, can introduce disturbances and blur this relationship. Measures to mitigate such influences include increasing perturbation amplitudes to enhance signal-to-noise ratios, averaging techniques to smooth out noise, and employing Faraday cages to shield against electrical interference.

Stability: EIS measurements, particularly at low frequencies causing long testing times, demand a steady-state system throughout the testing duration. A drift in open circuit voltage or measured current over time indicates an unstable system, leading to erroneous outcomes. Repetitive recording of EIS data serves as validation to ensure the system operates under steady-state conditions.

Finiteness: Impedance measurements should adhere to the finiteness principle. The real and imaginary impedance components must possess finite values across the frequency range. Moreover, impedance should converge to a constant value as the frequency approaches zero and infinity. This finiteness ensures that the system's electrical behavior remains well-behaved and interpretable across the spectrum of frequencies.

3

Methodology

This chapter outlines the methodology for investigating voltage losses in nickel electrodes, covering the experimental setup, procedures, and data extraction.

3.1. Preparation Setup

This section presents the experimental setup of a water electrolysis cell. The electrolyte in the cell is a 30 wt% KOH solution prepared by mixing KOH pellets (ACS reagent [56], ≥ 85 wt% purity) with demineralized water. Any impurities present in the pellets are detailed in Table A.1. The remaining 15 wt% of the pellets are assumed to be water in the mixing procedure to obtain the desired concentration. Figure 3.1 shows the complete experimental setup, which includes electrode design, cell design, temperature control, and data acquisition, all of which will be elaborated upon in the following sections.



Figure 3.1: The experimental setup includes the cell, hot plate, water bath, and electrical connections.

3.1.1. Electrode Design

A simple electrolysis cell requires two fundamental components: the anode and the cathode. Figure 3.2 shows the final electrode design. The electrode design is driven by four requirements, which will be discussed here:

- **Material Selection:** The electrode material must be high-purity nickel, as the scope of this study is to investigate nickel electrodes. Even trace amounts of impurities can significantly affect the electrolysis performance. XRF analysis shows the electrodes sourced from Veco Precision have 99.77 ± 0.4 wt% purity. The electrode material has a porous structure with pillars on one side and a flat surface on the other. More details on the material can be found in Appendix B.

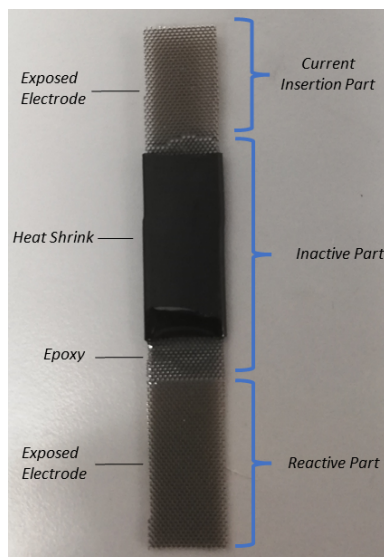


Figure 3.2: Electrode design.

- **Ease of Production:** A basic rectangular design was chosen to simplify production, enabling a cutting machine to produce the electrodes.
- **Reactive Area:** The reactive area is set at 2 cm^2 , optimized for a current density of 1 A cm^{-2} given the potentiostat's 2 A maximum output. This area, measuring 1 cm in width and 2 cm in length, is part of a three-sectioned electrode design. The other sections include a current insertion segment and an inactive zone. The central part is made inactive by applying a two-component epoxy layer covered with heat shrink, which is sealed off with the epoxy again. This protective method was confirmed using a color-sensitive coating beneath the epoxy, which showed no degradation after 5 hours of testing.
- **Uniform Current Distribution:** Ensuring equal activity across the electrode's height is crucial when inserting current from the top. Uniform current distribution is assumed to be achieved when the voltage loss over the reactive area is well below the Tafel slope. A voltage loss of 5 mV per electrode is deemed acceptable considering typical Tafel slopes in AWE ranging from $\frac{30}{2.3} = 13$ to $\frac{120}{2.3} = 52$ mV per e^- (Sections 2.2 and 2.3). Correspondingly, a resistance limit of $2.5 \text{ m}\Omega$ ensures this voltage constraint at the maximum used current of 2 A. A colleague measured the resistance of a 1 cm by 17.5 cm strip yielding $16 \text{ m}\Omega$. This measurement is adjusted for a 2 cm length resulting in $\frac{16 \text{ m}\Omega \cdot 2 \text{ cm}}{17.5 \text{ cm}} = 1.8 \text{ m}\Omega$, confirming uniform distribution as it remains below the $2.5 \text{ m}\Omega$ threshold.

3.1.2. Cell Design

The primary role of the cell is to maintain the correct configuration of all individual components. These components include the anode and cathode, as discussed in the preceding section. Additionally, two Hg/HgO reference electrodes will be used to measure the individual contributions of the anode and cathode to the cell potential. Zirfron serves as the diaphragm to separate the anodic and cathodic compartments. All of these components are submerged in 30 wt% KOH electrolyte.

The cell design is divided into two main components: the cell container with a lid and the electrode-diaphragm configuration. The former holds the electrolyte, prevents spillage, and mitigates gas buildup. The latter focuses on the arrangement of electrodes and the diaphragm to minimize the effects of bubbles on performance. The separation of the design into two distinct parts allows easy removal and replacement of electrodes and the diaphragm.

The final design is presented in Figure 3.3. Due to its resistance to alkaline conditions, the grey components are made of Poly(methyl methacrylate) (PMMA). Further details about the practical implementation of this design will be covered in subsequent sections.

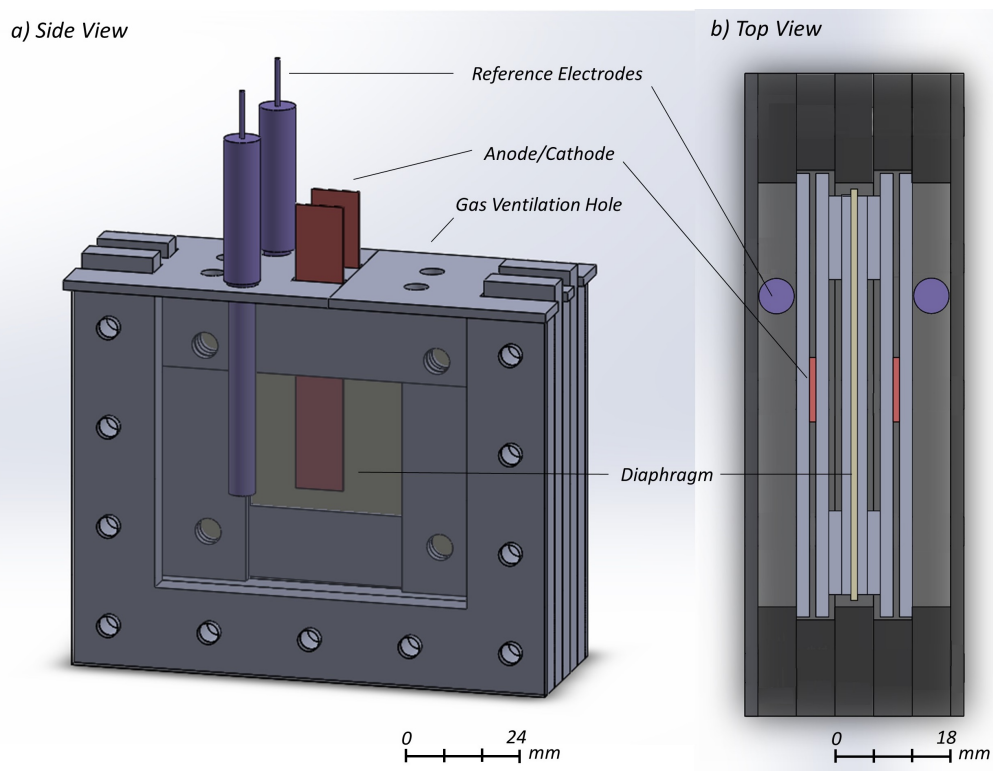


Figure 3.3: The cell assembly containing an anode, cathode, and two reference electrodes in a container. The end plate is made see-through, and the bolts are not depicted.

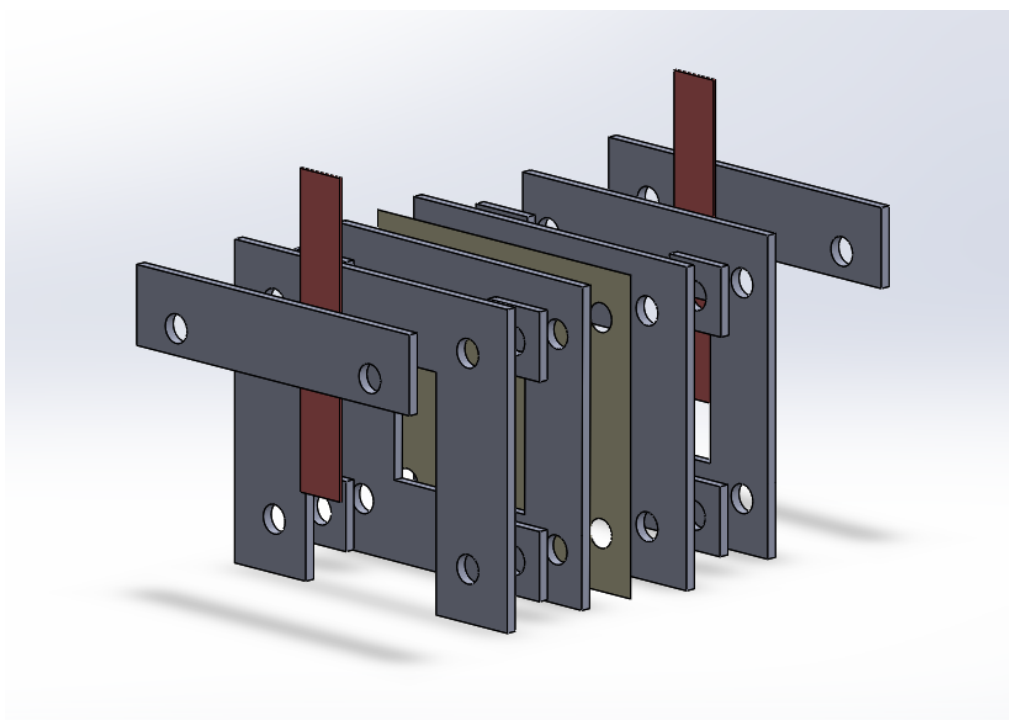


Figure 3.4: Assembly of the electrode-diaphragm configuration.

3.1.2.1. Cell Container with Lid

The cell container consists of five u-shaped PMMA plates with a thickness of 6 mm clamped between two 2 mm end plates. To ensure leak tightness, Ethylene Propylene Diene Monomer (EPDM) is placed between all contact points of two PMMA plates. Stainless steel bolts with a 5 mm diameter fasten the plates together. In this context, stainless steel is suitable since it does not come into direct contact with the electrolyte, eliminating the risk of contamination.

The internal dimensions of the cell container are as follows: the average length is 68 mm, the width measures 30 mm, and the height is 63 mm, resulting in a total internal volume of 129 cm³. The u-shaped plates alternate in width, forming two slits providing a stable position for the electrode-diaphragm configuration. Two of the u-shaped plates are taller to hold the lid in place securely.

The lid prevents the splashing of the electrolyte by the rising bubbles. For ease of assembly, the lid is designed in two separate parts. It features multiple holes, each serving specific functions. Two central slits in the lid allow the cathode and anode to protrude, facilitating cable connections. Additionally, two holes are designated for the reference electrodes. The four remaining holes, with a 5 mm diameter, provide a safe release of the gases that are produced.

3.1.2.2. Electrode-Diaphragm Configuration

The electrode-diaphragm configuration is designed as a single symmetrical piece, illustrated in Figure 3.4. Nylon bolts, with a 5 mm diameter, connect all the components. Nylon is used to prevent electrolyte contamination. The anode and cathode are "sandwiched" between two PMMA plates within this assembly. Four 2 mm spacers are positioned around the bolts to allow extra space between the electrode and the diaphragm to ensure the proper release of produced gases and minimize the influence of bubbles on the cell's performance. Following this arrangement, a diaphragm holder is placed, along with the diaphragm itself. This process is repeated with another diaphragm holder, the spacers, and the sandwiched electrode between the PMMA plates, completing the symmetrical piece. The assembled configuration can be easily inserted into the container. The slits within the container support this consistent positioning, as depicted in Figure 3.3 (b).

3.1.3. Temperature Control

Figure 3.5 shows the temperature control setup. Temperature regulation is achieved using a water bath on a hot plate. A broad glass beaker serves as the water bath. The cell is positioned on an open PMMA stand within the water bath to avoid direct contact with the hot plate. The open space underneath the cell allows for stirring using a magnetic stirrer. The stirring and temperature regulation are facilitated by the ika RCT Basic hot plate. The ika ETS-d4 Fuzzy temperature probe is placed inside the water bath and is connected to the hot plate, allowing temperature feedback control.

Inside the cell, a NiCr/NiSi thermocouple is placed in the electrolyte. The thermocouple is positioned in a small opening between the lids, inside the cathodic compartment, and around the outer edge of the nylon lower bolts of the electrode-diaphragm configuration. Convection driven by gas bubbles in the cell is expected to result in a reasonably uniform temperature profile.

The temperature of the electrolyte is controlled at 50 °C due to limitations in the temperature control system and the hot plate's capacity, even though an industry-relevant temperature would ideally be around 80 °C. The temperature control method is as follows: Temperatures are measured in the cell and the water bath. The water bath temperature is manually adjusted if the cell temperature deviates from the desired range. In cases of excessive overheating, ice can be added to the water bath to cool it down. It is important to note that temperature changes have a delay due to the insulating PMMA material of the cell, so adjustments should not be too extreme. Typically, adding ice is only necessary when the cell is turned on, as the water bath switches from heating to cooling. This temperature control method maintains the cell's temperature within a range of $\pm 2^{\circ}\text{C}$.

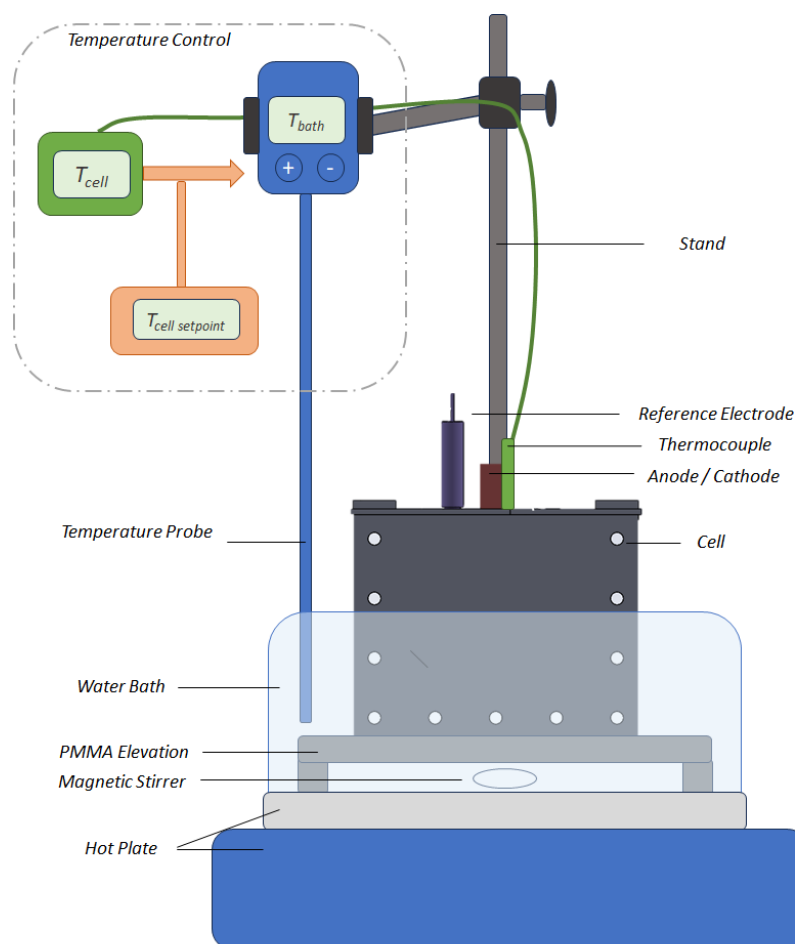


Figure 3.5: Temperature control setup utilizing an ika RCT basic hot plate combined with an ETS-d4 Fuzzy temperature probe.

3.1.4. Data Acquisition

In this section, the data acquisition setup and process are explained. Four data types are collected: current, voltage, impedance, and temperature. The following section discusses the electrical setup of all auxiliary devices that facilitate data acquisition. Additionally, the most important internal settings of the devices are discussed. The section closes by describing the verification method of the functionality of the reference electrodes and the overall cell voltage.

3.1.5. Data Acquisition Setup

The Solartron 1287a Potentiostat is utilized for current supply and logging but is limited to monitoring only one voltage channel. Given this limitation, an additional device is required to distinguish the voltage variations of the anode, cathode, and diaphragm. The DAQ 6001 from National Instruments is employed to overcome this limitation. An elaborate explanation of this choice and the challenges associated with measuring the additional potentials can be found in Appendix C. Figure 3.6 provides a visual overview of the distinct voltage measurements. The cell potential is measured by the potentiostat and the DAQ 6001, allowing for verification of the data obtained from the DAQ. Moreover, aligning these voltage readings facilitates data synchronization between the DAQ 6001 and the potentiostat.

The impedance measurements are facilitated by combining the potentiostat with the Solartron Frequency Response Analyzer (FRA) 1255B. Additionally, temperature monitoring is facilitated by the National Instruments cDAQ-9171, which connects to a thermocouple immersed in the electrolyte. All these instruments - FRA, potentiostat, DAQ 6001, and cDAQ-9171 - are interfaced with a laptop. The potentiostat can be controlled with 'Corrware' software, the FRA with 'Zplot' software, and the latter two devices from National Instruments with 'LabView' software.

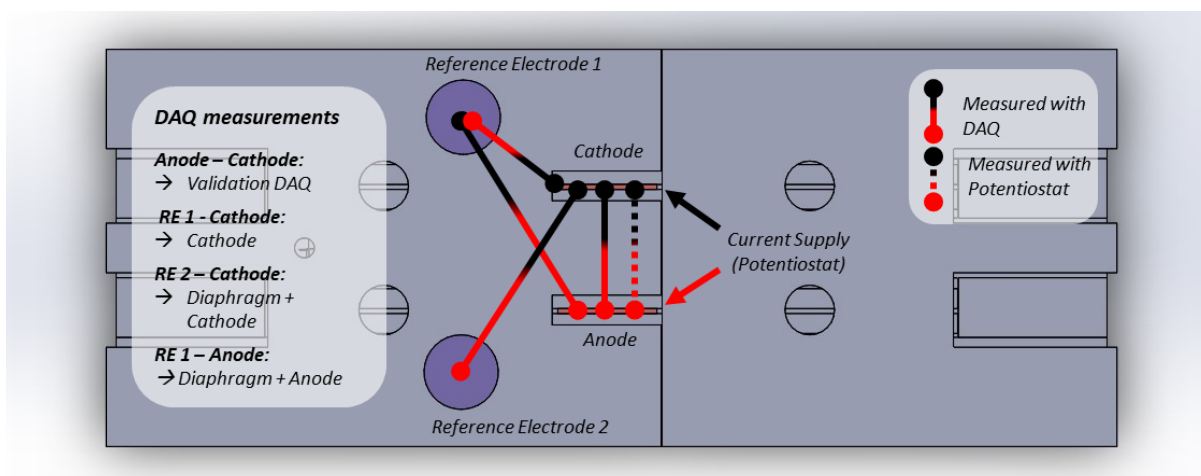


Figure 3.6: Cell connections, Red is the positive, and black is the negative. The dotted line is the sense potential of the potentiostat. The continuous lines are potentials measured by the data acquisitions card (DAQ). The current is supplied by the potentiostat.

3.1.5.1. Auxiliary Devices Settings

The most important settings of the auxiliary devices are listed:

- **Potentiostat**

- **Acquisition rate** is set on the maximum value of 12 points per second, which is achievable when the low pass filter is disabled [57].

- **FRA**

- **Frequency range** of 0.1 to 10^5 Hz will be used based on the accuracy contour plot in Figure 3.7. Given the typical cell impedance readings of 0.1-10 Ω , the upper-frequency limit of 10^5 Hz is selected to prevent excessive error inaccuracies. The lower limit of 0.1 Hz avoids prolonged tests, which can cause problems if the system is slightly unstable.
- **AC amplitude** of 1 % of the DC is selected, which falls within the specified guideline to ensure compliance with linearity requirements and to achieve a favorable signal-to-noise ratio [58].
- **The number of measurements** is 10 measurements per decade to ensure robust data collection [58].
- **Integration of signal** measures impedance over multiple perturbation cycles. Longer integration times generally enhance accuracy. Auto-integration is employed to optimize efficiency but avoids long testing times. An integration time of maximum 10 seconds is used per frequency but advances to the next point when the standard deviation of three cycles on the sensing current is less than 10%. This duration is not sufficient for capturing three complete cycles below 0.3 Hz. However, this integration time is still utilized to avoid prolonged testing durations. The maximum experiment duration is around 8 minutes (10 seconds per measurement x 10 measurements per decade x 5 decades).

- **DAQ 6001**

- **The data acquisition rate** is set at 1000 samples per second.
- **The resolution** is 0.6 mV. The measuring range determines the resolution as it needs to be distributed across the available 14 bits. A range of -5 to 5 V covers all the expected potentials. With 14 bits, there are 16384 levels, resulting in a resolution of 0.6 mV (10 V divided by 16 384 levels) [59].

- **cDAQ-9171**

- **The data acquisition rate** is set at a similar rate of 1000 samples per second as the DAQ 6001 used for potential measurements.
- **The calibration factor** in the 'Labview' software adjusts the offsets of the thermocouple readings and is set to 20. For precise temperature measurement, the thermocouple requires calibration. This calibration

is performed using an ice bath, where the temperature is approximately 0 °C with minimal error. After placing the sensor inside the bath, adjustments are made to the calibration value until the thermocouple reads 0 °C. The temperature reading is compared to the EDS-4 Fuzzy temperature probe within the same water bath to validate the calibration at different temperatures.

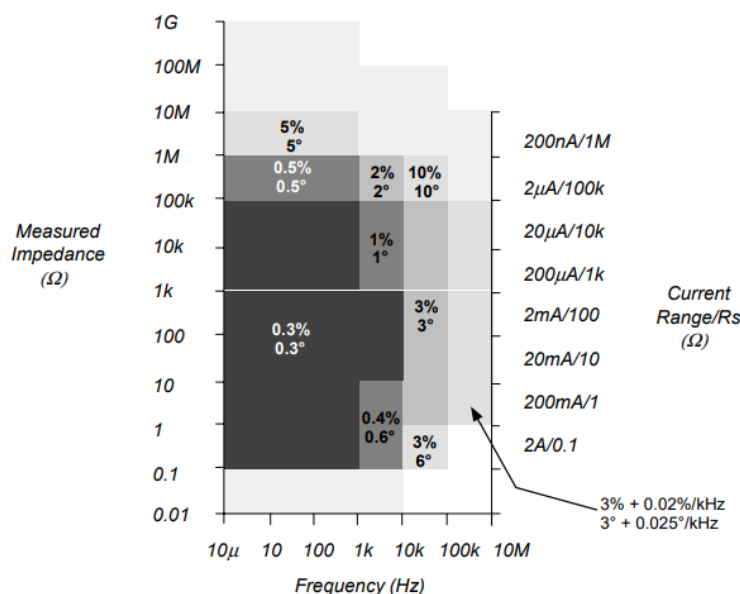


Figure 3.7: Accuracy contour plot of the FRA 1255b. Source: Manual [60].

3.1.5.2. (Reference) Electrode Verification

To ensure reliable voltage data, verification of the reference electrode functionality is important. Extended use can introduce voltage deviations due to ion crossover between the electrolyte and the reference electrode's internal solution [61]. As the internal solution concentration is 1 M NaOH and the electrolyte concentration is 6.9 M KOH, species and concentration differences can impact the reference electrode potential. The reference electrodes are compared for validation against a similar but unused Hg/HgO reference electrode. A voltage difference under 4 mV is deemed acceptable. Otherwise, the reference electrode internal solution is refreshed, and the potential difference is reevaluated after a day.

A method to detect issues with cell voltage measurements is to perform an EIS measurement just before the electrolysis test when the electrolyte is stable at 50 °C. The open circuit potential (OCP) measurement with an AC amplitude of 5 mV determines the total cell resistance. Significant deviations in resistance may indicate issues with temperature readings, electrode assembly, or electrical connections.

3.2. Experiments

This section details the conducted tests, categorized into two types as illustrated in Figure 3.8: the galvanostatic duration and interval tests. These tests exhibit variations, which will be elaborated on in the following sections. The galvanostatic mode, featuring a constant current, is selected to ensure consistency in gas formation and mass transfer effects. Fresh electrodes are used for every test. The section closes by briefly mentioning the surface characterization techniques that were used.

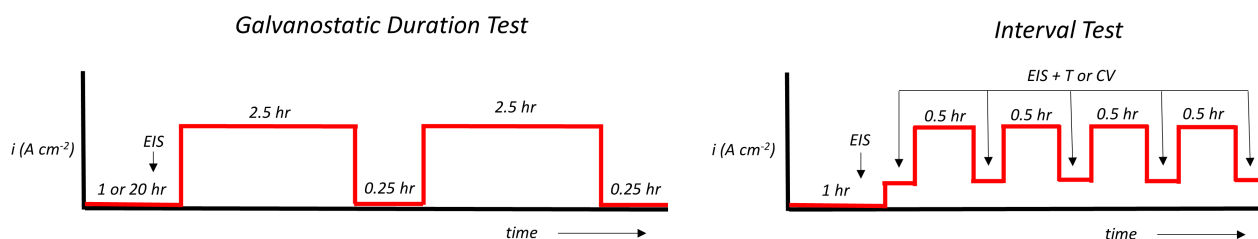


Figure 3.8: Two variations of the electrochemical tests performed in this research. In the interval test, the electrochemical characterization methods used are CV, EIS, and Tafel slope analysis (T) by using potential steps

3.2.1. Galvanostatic Duration Tests

The galvanostatic duration test aims to monitor the potential evolution of nickel electrodes over time. The period from immersing the electrode-diaphragm configuration into the electrolyte to current insertion defines the electrolyte exposure time. A constant current is applied to the cell for 2.5 hours, followed by a 15-minute rest at open circuit. This sequence is repeated. Current densities of 0.3, 0.5, and 1 A cm⁻² are examined, with the latter repeated twice for reproducibility. An additional test involves an extended electrolyte exposure time of 20 hours to observe its significance on the test method. These current densities align with European testing guidelines for AWE tests [58].

3.2.2. Interval Test

The interval test uses electrochemical characterization methods to assess the effects of high current density on electrode deactivation. Initially, electrochemical characterization is conducted. Subsequently, a 0.5-hour electrolysis interval at 1 A cm⁻² is applied, after which electrochemical characterization is performed again. This cycle is repeated three times, resulting in a total electrolysis time of 2 hours. The electrochemical methods include cyclic voltammetry, EIS, and Tafel slope analysis using potential steps. The latter two methods are combined in a single experiment.

3.2.2.1. Cyclic Voltammetry

The initial sweep cycle begins at the OCP. An anodic sweep is conducted, cycling five times between 2.2 and -1 V cell potential. Subsequently, the cycling range is expanded to 3.1 and -1 V for three additional cycles. Following this, a 0.5-hour electrolysis interval is implemented at 1 A cm⁻². For the next set of cycles, the sweep initiates at the upper anodic potential, spanning between 3.1 and -1 V for three cycles. The electrolysis interval, along with CV analysis, is repeated three times. The sweep rate is set at 20 mV s⁻¹, in line with the recommendations from the European guidelines [58].

3.2.2.2. Tafel Analysis and EIS

The cell is set at 0.05 A cm⁻² for 10 minutes to reach a semi-constant potential. An EIS measurement is performed with an AC amplitude of 0.5 mA cm⁻², adhering to 1% of the current density requirement mentioned in Section 3.1.5.1. The EIS measurement is followed by a potential step sequence from 1.8 V to 3.2 V with steps of 0.1 V to generate a polarization curve. The uncompensated potential is held for 15 seconds to allow for the stabilization of the voltage. After completing the potential steps, a high current density of 1 A cm⁻² is held for 30 minutes. Subsequently, similar potential step measurements are performed but with decreasing potential. The low current density of 0.05 A cm⁻² is held for 1 minute, after which another EIS measurement is executed. This sequence is repeated three times.

3.2.3. Electrochemical Surface Characterization: SEM, XRF, and XRD

For material characterization, Scanning Electron Microscopy (SEM), X-ray Diffraction (XRD), and X-ray Fluorescence (XRF) are used on fresh nickel electrode samples and samples exposed to the galvanostatic duration test of 1 A cm⁻².

3.3. Data Processing

This section describes the process of extracting useful information from the experiments mentioned in the previous section. The section focuses on the extraction of the individual potentials and the treatment of impedance data.

3.3.1. Treatment Individual Potential Data

The voltage data of interest includes the anodic, cathodic, cell, and diaphragm voltage measurements. The overview of the measured cell potentials is given in Figure 3.6. The DAQ and the potentiostat measure the cell potential to validate the DAQ measurements. The DAQ cell voltage measurement is used in further data analysis as no synchronization is required to compare with the other potentials. The cathode cell potential is easily determined as it is measured directly. The anodic cell potential is determined by subtracting the cathode with diaphragm potential from the cell potential. The diaphragm potential is determined by subtracting the cathode potential from the cathode with diaphragm potential.

3.3.2. EIS Processing

The processing of impedance data obtained from EIS measurements involves data validation, followed by fitting it to an equivalent circuit. A common approach to validate the data is to perform the Kramers-Kronig test, detailed in Section 2.5.2. Z-plot incorporates a built-in function that applies this test by calculating the real part of the impedance from the imaginary part. Data that adheres to this relation is further processed by fitting it to an equivalent circuit.

The simple equivalent circuit in Figure 2.4 is used for this fitting procedure. It consists of a resistance simulating the ohmic resistance in the cell. The other two RC elements have a time constant and represent the charge transfer resistance of the half-reaction, along with the corresponding double-layer capacitance. The obtained parameters will be used for analysis. Assigning the RC elements to the anode or cathode is based on trends observed in the potentials during the EIS measurements and supported by data from other experiments.

4

Results and Discussion

This chapter delves into the results and discussion of the experimental research, all conducted at 50 °C in 30 wt% KOH electrolyte. The first section assesses the reproducibility of the test method and setup. The second section employs electrochemical techniques (CV, EIS, Potential steps) and surface characterization methods (XRF and SEM) to pinpoint deactivation mechanisms during electrolysis at 1 A cm⁻² in nickel electrodes. The galvanostatic long-duration test at 1 A cm⁻² unveils different timescales associated with these mechanisms. The chapter concludes by exploring the impact of varying current densities (0.3, 0.5, 1 A cm⁻²) on voltage development over time.

4.1. Reproducibility of Untreated Nickel Electrodes

This section evaluates the reproducibility of the test method and setup for untreated nickel electrodes. The validation method employs the long-duration test at 1 A cm⁻² (Section 3.2.1) with an electrolyte exposure time of 1 hour executed twice. Comparisons between short (1 hr) and prolonged (20 hr) electrolyte exposure times aim to assess the variable's impact on results.

Potential differences during electrolysis may arise from variations in charge transfer or ohmic resistance. The ohmic cell resistance, determined through EIS before the first current insertion, is examined to discern the contribution of ohmic resistance. The ohmic resistance results are detailed in the first column of Table 4.1. Figure 4.1 visually represents the components influencing the ohmic resistance of the cell. The subsequent discussion will explore the factors contributing to potential inconsistencies in the anode, cathode, and diaphragm potential measurements. For a discussion on interpreting the results and potential sources of deactivation, refer to Section 4.2.6. As temperature influences the resistance in various ways, the discussion starts with examining the impact of temperature on total resistance.

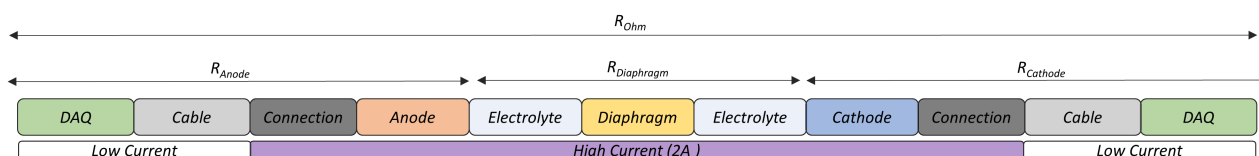


Figure 4.1: A schematic representing the different contributions affecting the cell voltage measurements. Starting from the DAQ internals, where the cables are connected, through the connection to the anode, the anode itself, the electrolyte, the diaphragm, another layer of electrolyte, the cathode, the connection of the cathode to the cables, and finally back to the internals of the DAQ. The path where high current flows is shown in purple.

- **Temperature:** Temperature can significantly influence the total resistance by changing the conductivity or the reaction kinetics. The temperature in the cathodic compartment was within the 50 ± 2 °C margins for the first cycle (see Figure E.1 in the appendix). The second cycle began at 44°C because the heating system could not quickly compensate for the heat lost during the 15-minute rest period with the current turned off. Although the temperatures in the second cycle exceeded the 50 ± 2 °C range for the first ten minutes in all cycles, the extent of the deviation between all tests was similar. Therefore, the temperature variations are not expected to cause the observed inconsistencies.
- **Cathode:** Figure 4.2 (a) shows a consistent potential development during the charging of the duplicates. However, the deactivation pattern exhibits differences in both timing and extent. This flexibility is evident from the 20 mV lower potential observed at the end of the first cycle in one of the duplicates (*). Importantly, this difference in extent vanishes in the second cycle, suggesting that the inconsistencies in the first cycle stem from the slight flexibility inherent in the deactivation mechanism of nickel cathodes.

The variability of the cathode becomes apparent from the moment the current is switched off, as illustrated in Figure 4.2 (b). The significant drop in potential indicates a change in surface characteristics. Notably, the prolonged-aged sample exhibits behavior similar to the shortly-aged samples, implying that prolonged aging is not a significant factor for the cathode when examining the deactivation mechanism.

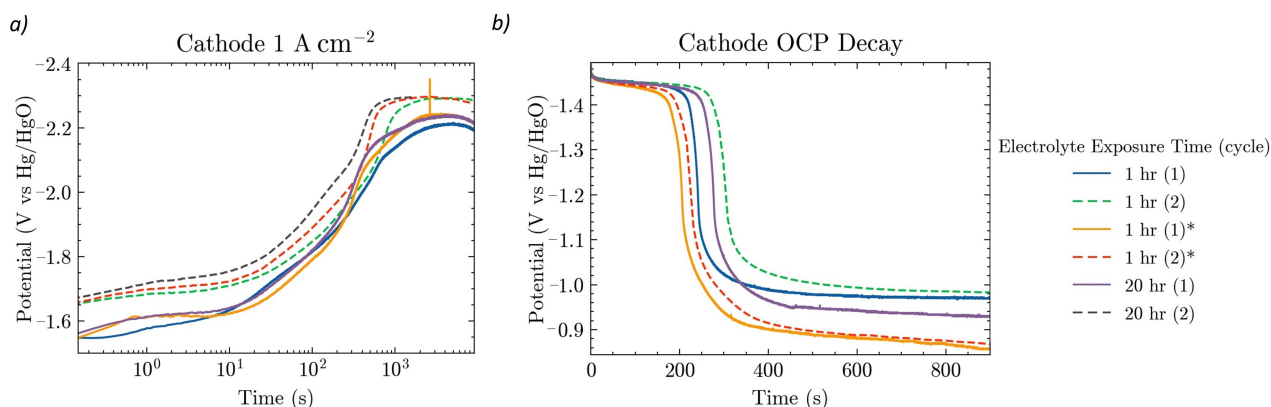


Figure 4.2: Long-duration test of the cathode at 1 A cm^{-2} at 50°C using fresh samples. Panel (a) displays the 2.5-hour charging cycles and panel (b) illustrates the 15-minute rest after the charging period. The electrolyte exposure time is either 1 hour or 20 hours. The * denotes a duplicate test. Dotted lines visualize the second cycle.

- **DAQ + Cables + Connection:** The DAQ internals, cables to the DAQ, and the connection from the cables to the electrode are implemented similarly for both electrodes. Therefore, these components are expected to similarly affect the anodic and cathodic potential. The connection and electrode resistance, with a current of 2 A running through them, are expected to exert the most substantial impact on the potential. As discussed previously, the inconsistencies in cathode potential primarily stem from the intrinsic behavior of the cathode itself. This implies that resistances related to the DAQ, cables, and the connection from the cables to the electrodes remain consistent between tests. Consequently, deviations in these resistances are not expected on the anode side.

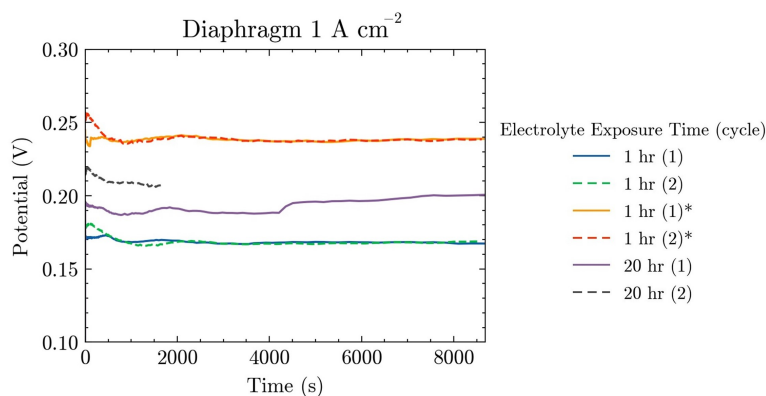


Figure 4.3: Long-duration test of the diaphragm voltage drop at 1 A cm^{-2} at 50°C using fresh Zirfron. The graph displays the 2.5-hour charging cycles. The electrolyte exposure time is either 1 hour or 20 hours. The * denotes a duplicate test. Dotted lines visualize the second cycle.

- **Electrolyte + diaphragm:** Figure 4.3 illustrates the influence of electrolyte and diaphragm resistances on potential measurements. These measurements are derived by subtracting the potential cathode-reference electrode 1 from cathode-reference electrode 2 (see Figure 3.6). The consistent 70 mV difference between the duplicates throughout the test underscores the non-reproducible effects of the electrolyte or the diaphragm. In the second column of Table 4.1, the initial resistance of the electrolyte + diaphragm is determined by dividing the initial potential by the current running through it.

The electrolyte is expected to exert minimal influence on the potential/resistance differences due to the anticipated similar conductivity, which depends on concentration and temperature. No deviation in concentration should be present as electrolytes from a similar batch are used. Additionally, temperature

effects are assumed to be minimal, as discussed earlier. Therefore, potential deviations arise mainly from the diaphragm by assuming similar electrolyte resistance. What causes this resistance difference remains uncertain. The resistance of the prolonged aging test falls between the values observed in the two shortly-aged duplicate tests, suggesting no significant impact of prolonged electrolyte exposure time on the diaphragm resistance.

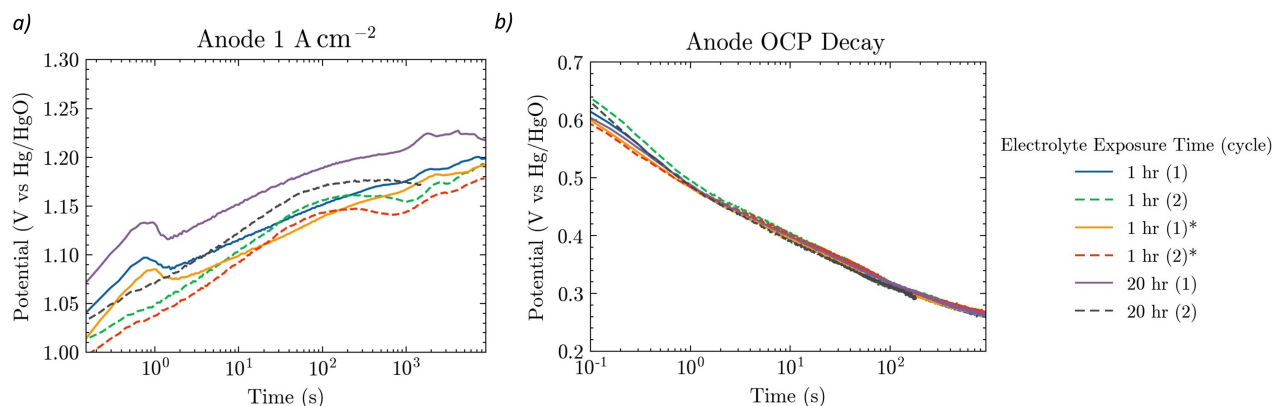


Figure 4.4: Long-duration test of the anode at 1 A cm^{-2} at $50 \text{ }^\circ\text{C}$ using fresh samples. Panel (a) displays the 2.5-hour charging cycles and panel (b) illustrates the 15-minute rest after the charging period. The electrolyte exposure time is either 1 hour or 20 hours. The * denotes a duplicate test. Dotted lines visualize the second cycle.

- **Anode:** Figure 4.4 (a) shows the anodic long-duration test results, where a consistent voltage development with an offset is observed. The comparable voltage development, even as the consistent OCP decay within the rest period after electrolysis (Figure 4.4 (b)), suggests that deactivation behavior is similar for the three tests. The ohmic resistance of the anode will be estimated to identify if this, or the charge transfer resistance, is the primary cause of the anodic potential offset during electrolysis.

Subtracting the diaphragm + electrolyte resistance from the ohmic cell resistance yields the cathode's and anode's resistance (third column Table 4.1). If the cathode does not contribute to the observed resistance differences, the differences are attributed to the anode. These differences, calculated with the 1-hour aged duplicate (*) as a reference (fourth column Table 4.1), follow a similar trend to the differences observed in the potential offsets during the charging tests of the anode (fifth column Table 4.1). Therefore, the difference in ohmic loss could explain the anodic inconsistencies.

A possible explanation is that the insulating NiO layer thickness forms arbitrarily, resulting in different ohmic resistance. During anodic polarization, this NiO layer persists and may even grow. It is important to note that the growth must occur at a similar rate to explain the constant offset maintained during the charging test. The measured potential difference, approximately half of the estimated potential difference, can be attributed to the initial NiO layer on the cathode. The presence of the initial NiO layer contributes to the measured ohmic resistance before any current insertion. The NiO layer on the cathode is reduced during electrolysis, leading to no offset in potential. The highest resistance of the prolonged aged anode is as expected, as the NiO layer has more time to develop. Although the NiO layer thickness deviations can explain the results, it is crucial to acknowledge that this is just one hypothesis.

	R_{Ohm} (Ω)	R_{Dia} (Ω) (V_{Dia} (V))	$R_{\text{Cat + An}}$ (Ω)	$\Delta R_{\text{Cat + An}}$ (Ω) ($\Delta V_{\text{Cat + An}}$ (V))	ΔV_{An} (V)
20 hr aged	0.33	0.10 (0.20)	0.23	0.05 (0.1)	0.05
1 hr aged duplicate (*)	0.30	0.12 (0.24)	0.18	0	0
1 hr aged	0.28	0.085 (0.17)	0.195	0.015 (0.03)	0.02

Table 4.1: Table listing estimated resistances in the cell: R_{Ohm} represents the overall ohmic resistance obtained through EIS; R_{Dia} is the resistance of the diaphragm + electrolyte, determined by dividing initial potential (V_{Dia}) by the total current of 2 A; $R_{\text{Cat + An}}$ is the combined resistance of the anode and cathode, calculated by subtracting R_{Dia} from R_{Ohm} ; $\Delta R_{\text{Cat + An}}$ indicates the difference in $R_{\text{Cat + An}}$ with the 1-hour aged duplicate (*) as a zero reference. $\Delta V_{\text{Cat + An}}$ represents the estimated potential by multiplying with 2 A; ΔV_{An} is the estimated constant voltage offset of the anodic charging curves shown in Figure 4.4. The color gradient from green to red illustrates the lowest to highest resistance.

This research focuses primarily on the deactivation mechanisms in nickel anodes and cathodes. Despite minor inconsistencies, the deactivation trend is observed similarly in both the anode and cathode, with unclear

dependence on prolonged aging time. The results are deemed reproducible, aligning with the research focus. However, conclusions regarding the exact time and extent of cathode deactivation need careful consideration, as they appear to deviate within the tests. For the anode, conclusions about the extent should be drawn cautiously when different samples are used, as variations could occur.

4.2. Effect of high load (1 A cm⁻²) on the Nickel Electrode Characteristics

This section overviews nickel electrode deactivation mechanisms and corresponding timescales during galvanostatic charging at an industry-relevant current density of 1 A cm⁻². The following subsections employ various surfaces and electrochemical characterization methods to address the research question:

- **XRF Analysis:** Fresh electrode material, anode, and cathode undergo XRF analysis to detect any impurities leaching out or being incorporated into the lattice, potentially causing deactivation.
- **SEM Imaging:** This subsection investigates changes in surface characteristics through SEM imaging of fresh electrode material and an anode and cathode.
- **Interval Test with CV:** Deactivation timescales are examined using CV, focusing on redox peaks and their variations over different timescales.
- **Interval Test with Polarization Curves:** The same interval test assesses deactivation by examining polarization curves and extracting kinetic parameters.
- **Interval Test with EIS:** Employing EIS, this section studies the effect of electrolysis on charge transfer resistance and electrodes' double-layer capacitance.
- **Galvanostatic Long-Duration Test:** The section explores the galvanostatic long-duration test, utilizing the obtained information to unravel the different deactivation timescales and corresponding phenomena.

4.2.1. Surface Characteristics: XRF

Atomic Content (wt%)			
	Fresh	Anode	Cathode
Ni	99.769	78.734	89.999
Fe	0.074	-	-
Si	0.054	-	0.05
Al	0.043	-	0.038
Cl	0.032	0.091	0.043
S	0.028	0.022	0.054
K	-	20.692	9.468
P	-	0.192	0.202
Mg	-	0.27	0.146

Table 4.2: XRF data for fresh nickel electrode material, a nickel anode, and a nickel cathode after the galvanostatic long-duration test of the short-aged duplicate samples (*). The values are normalized to 100 wt%. Uncertainties are not provided as they are expected to be significantly larger due to salt formation on the electrodes.

The XRF analysis, depicted in Table 4.2, offers a comparative view of the material composition before and after subjecting it to a long-duration test at 1 A cm⁻². Due to salt presence and porous electrode geometry, interpreting shifts in impurity quantities is challenging. Consequently, this discussion centers on impurities that either disappeared or emerged, assessing their potential roles in nickel electrodes' (de)activation processes. The observed (dis)appearance will be examined using Pourbaix diagrams to discern if the changes align with expectations under the highly alkaline conditions and cathodic or anodic polarization:

- **Anode iron (Fe) leaching:** Iron is expected to dissolve into (Fe₄O₄)²⁻ (Figure E1). Iron leaching from nickel anodes during extended galvanostatic charging is a recognized phenomenon [24]. Since iron in the lattice structure of nickel enhances the OER, the leaching of iron leads to deactivation [25, 32].
- **Anode aluminium (Al) leaching:** Aluminium is expected to dissolve into AlO₂⁻ (Figure E3). Due to its high tendency for dissolution, aluminium leaching is often employed intentionally to create a large surface area and

porous structure [62]. It is somewhat surprising that aluminium persists at the cathode. Aluminium enhances the OER kinetics when incorporated into the Ni-Fe-OOH structure [63]. Therefore, leaching is assumed to result in deactivation.

- Anode silicon (Si) leaching: Silicon is expected to dissolve into H_7SiO_6^- (Figure F.2). Silicon leaching is observed in nickel alloys in alkaline conditions, increasing the electrode surface's roughness [64]. The initial small amounts of silicon present are not expected to cause significant alteration in surface roughness.
- Cathode iron (Fe) leaching: The most stable phase of iron under cathodic conditions could be metallic Fe, HFeO_2^- , or $(\text{Fe}_4\text{O}_4)^{2-}$ dependent on the extent of cathodic polarization (Figure F.1). Iron leaching out and not depositing on top of the electrode could be due to the polarization method. The constant current application resulted in iron leaching while cycling increased iron content [24]. Existing literature does not distinctly indicate whether iron impurities positively or negatively affect the HER kinetics, only that an iron layer on top prevents deactivation [25, 39]. Therefore, no proper conclusions can be drawn.
- Cathode/anode potassium (K) appearance: Potassium is in significant quantities present on the anode and cathode. It is known to form potassium carbonate due to the reaction of KOH electrolyte with CO_2 from the air. This salt is also observed in the XRD analysis (Section G) of the same anode and cathode sample used in the XRF analysis. Potassium is expected to be only present in the salt and not incorporated into the nickel lattice.
- Cathode/anode phosphorus (P) appearance: The most stable phase is PO_4^{-3} (Figure F.4). Literature does not mention phosphorus's incorporation into the nickel lattice structure. Therefore, phosphorus is assumed in the form of phosphate salt precipitates. The low quantities compared to potassium carbonate and nickel could explain the absence in the XRD measurements.
- Cathode/anode magnesium (Mg) appearance: The most stable form under both anodic and cathodic polarization is $\text{Mg}(\text{OH})_2$ (Figure F.5). The formation of $\text{Mg}(\text{OH})_2$ can passivate the surface, deactivating the HER and OER [65].

In conclusion, the leaching of iron and aluminum impurities could be a potential deactivation mechanism for the anode. Magnesium impurities in the electrolyte could be a deactivation mechanism for both electrodes by passivating the surface.

4.2.2. Surface Characteristics: SEM

SEM is employed to investigate potential changes in the surface characteristics of the nickel electrodes due to electrolysis. These changes may include increased surface roughness attributed to factors such as impurity leaching [24, 64]. Examining SEM images of the fresh nickel electrode material and those subjected to the long-duration test at 1 A cm^{-2} enables the characterization of possible surface structure changes caused by electrolysis. Using similar samples as in the XRF analysis links the composition to the structure. Unfortunately, the cathode samples were lost after the XRF analysis and could not be examined.

Figure 4.5 (left) displays the SEM image of the flat side of the fresh electrode material, while Figure H.1 shows images of the pillar side. Only the flat side is analyzed for the anode due to time constraints on the SEM device. This side is chosen for analysis due to the expected increased reactivity as it points towards the diaphragm. Figure 4.5 (right) displays SEM images of the flat side of the anode. The images show a slight deviation in angle and different light contrast, making conclusions challenging. However, in the x5000 image, dents are visible in the anode, while not in the fresh material. A potential cause could be the leaching of impurities such as iron, silicon, and aluminium, identified in the XRF analysis (Section 4.2.1).

Additionally, a closer inspection of Figure 4.5 reveals some white patches in the SEM image of the anode. White patches result from increased electron beam backscattering due to reduced conductivity in these areas. A reduced conductivity can come from salt formation or an increased thickness of NiO.

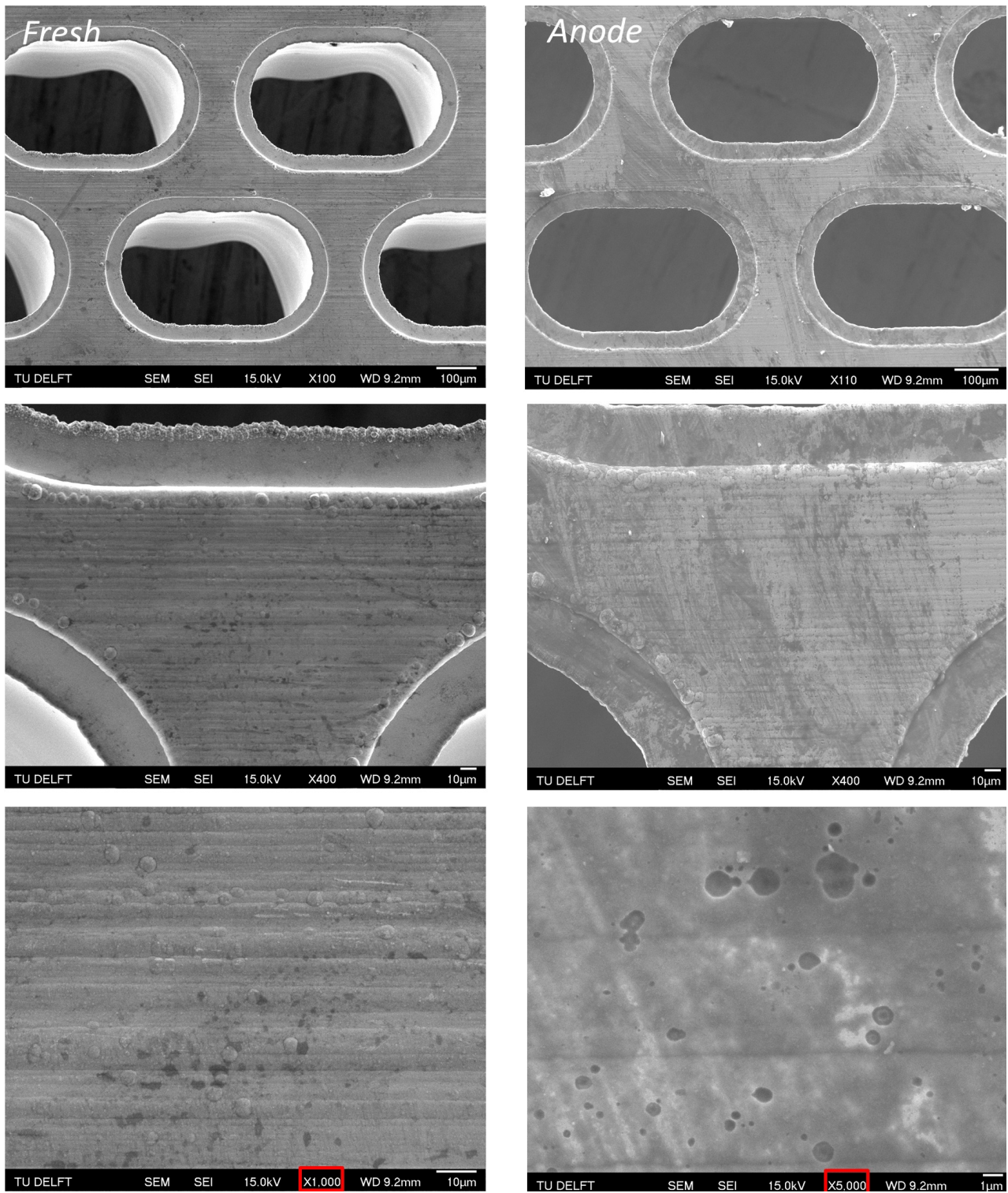


Figure 4.5: SEM images of the flat side of the fresh electrode material (left) and of the anode after a long-duration test at 1 A cm^{-2} at different magnifications. Note that the lowest pictures have different magnifications of x1000 (left) and x5000 (right).

4.2.3. Interval Test: Cyclic Voltammetry

During the interval test, cyclic voltammetry investigates deactivation at nickel electrodes on different timescales by looking at the redox peaks. The outlined sweeps occur after each electrolysis interval:

- 0 hr: Five sweeps between -1 and 2.2 V cell potential.
- 0 hr: Three sweeps between -1 and 3.1 V cell potential.
- 0.5, 1, 1.5, 2 hr: Three sweeps between -1 and 3.1 V cell potential.

Cyclic voltammograms (CVs) before any electrolysis interval (0 hr) are studied to isolate the deactivation effects of short exposure to electrolysis. The effects of deactivation originate in this case only from the electrolysis within the period of the sweep above the equilibrium potential. Comparing CVs before and after each electrolysis interval assesses the effect of longer electrolysis durations.

This section outlines the extraction method for anodic and cathodic CVs from the overall cell CV. Subsequently, the anode and cathode deactivation are identified, and potential reasons for this deactivation are sought within the CV data. The deactivation extent is quantified using anodic and cathodic potentials at 30 mA cm^{-2} . This chosen current density is higher than the CV peak current to mitigate interference but remains within a range that ensures observation across all CV sweeps. The 30 mA cm^{-2} threshold is crossed twice in every CV: once when the electrolysis extent increases and once when it decreases.

4.2.3.1. Extraction Anodic and Cathodic CVs

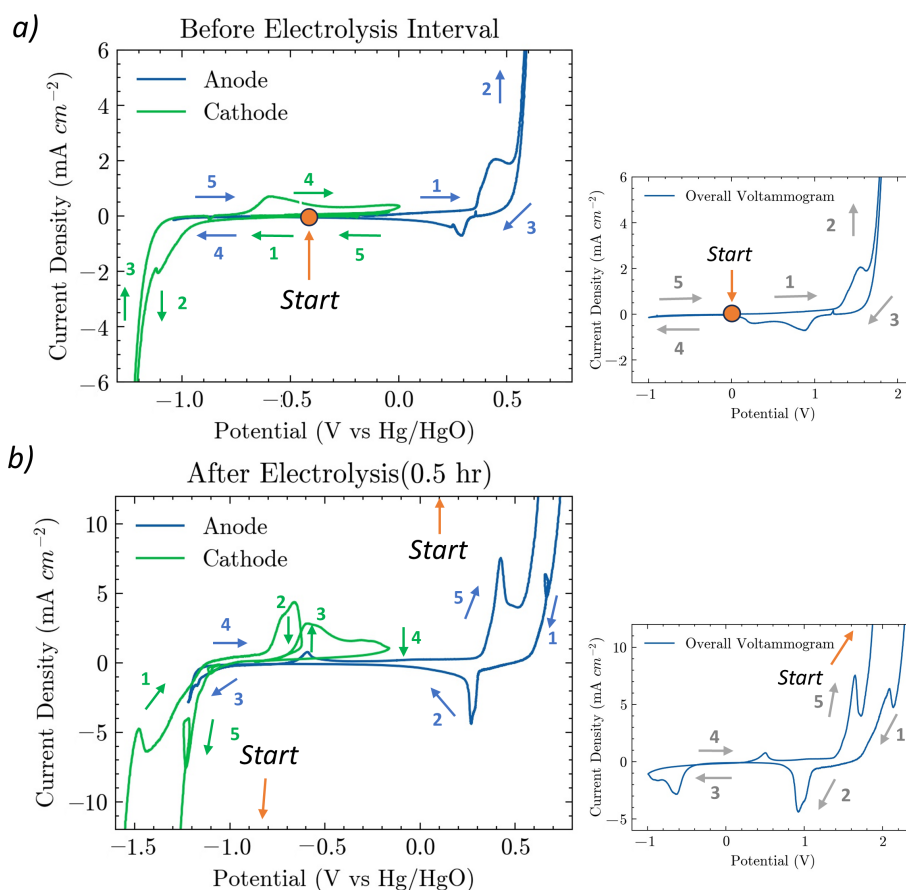


Figure 4.6: Cyclic voltammetry profiles of the anode and cathode derived from the overall cell voltage. Subfigure (a) depicts CVs measured before any electrolysis interval, featuring a distinct starting point. Scanning rate = 20 mV s^{-1} . Voltage range sweep = 2.2 to -1 V (cell potential). In contrast, subfigure (b) illustrates CVs measured after the electrolysis intervals. Scanning rate = 20 mV s^{-1} . Voltage range sweep = 3.1 to -1 V (cell potential). The numbered arrows denote the sequence of the sweeps.

This section details the extraction process of individual anodic and cathodic CVs from the overall CV as the potential undergoes a linear sweep across the entire cell. Figure 4.6 (a) visually represents how the anodic and

cathodic CVs shape before any electrolysis interval (0-hr interval). The sweeping begins at a cell potential of 0 V, corresponding to its OCP. The numbers on the arrows indicate the sequence of cycling. Figure 4.6 (b) illustrates the shaping of anodic and cathodic CVs by the overall cell CV after electrolysis intervals. The CVs commence at the upper cell potential.

It is crucial to emphasize that the cell potential, not the anodic or cathodic potential, directly controls the potential. Consequently, individual electrode CVs assume counterintuitive shapes as they mutually influence each other. This mutual influence is evident in the cathode CV in Figure 4.6 (b). The dominance of anodic behavior results in the cathodes deviating peaks. The formed oxides at the anode need to be reduced, necessitating an oxidative current at the cathode to complete the circuit. This process happens twice where NiOOH decomposes to Ni(OH)₂ (blue arrow 2) and Ni(OH)₂/NiO decomposes to metallic nickel (blue arrow 3). Both times, the cathode enters a region where oxidative currents are allowed (green arrows 2 and 3).

It is noteworthy that the cathode can also influence the anode, as demonstrated in arrow 1 (blue). The reductive peak at the cathode induces a loop in the anodic CV at arrow 1 (green), highlighting the interconnected nature of the electrode behaviors in this electrochemical system.

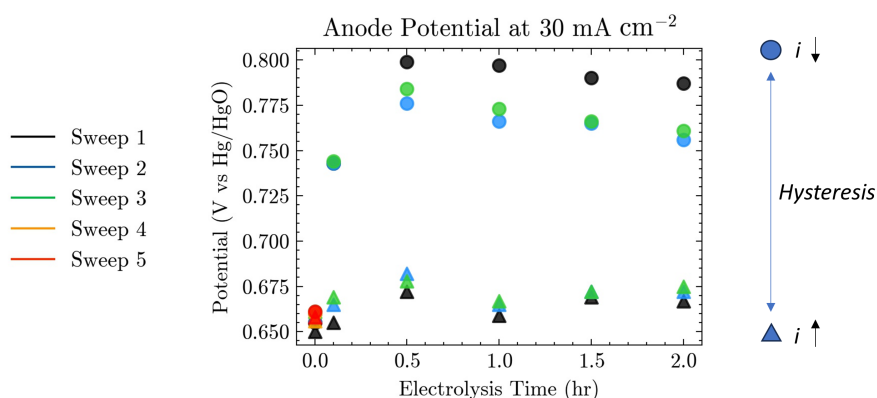


Figure 4.7: The anodic potentials corresponding to 30 mA cm⁻² during the CV sweep. Triangles denote an increasing electrolysis extent, while circles a decreasing one.

4.2.3.2. Anode Deactivation Mechanism

Figure 4.7 shows the anodic potentials at 30 mA cm⁻². The following key observations are made:

- **No deactivation observed below 0.67 V vs. Hg/HgO:** The anode was swept up to 0.67 V vs. Hg/HgO (equivalent to a cell potential of 2.2 V) during the initial five cycles at the 0-hr interval. In these cycles, the anode exhibited a consistent potential when crossing the 30 mA cm⁻² threshold. This consistent behavior confirms the absence of deactivation below this voltage.
- **Hysteresis of 0.15 V emerges within several minutes:** A hysteresis effect of 0.1 V appeared when the sweeping range was extended to 2 V vs. Hg/HgO (equivalent to a cell potential of 3.1 V) during the 0-hr interval. Figure 4.8 shows the specific region of the CVs characterized by the Ni(OH)₂/NiOOH transition for the limited and extended sweep at the 0-hr electrolysis interval. For the limited sweep where almost no deactivation occurred, oxidative peak c and reductive peak c' exhibit an increasing trend over consecutive sweeps. The increase in both peaks suggests a balanced electrochemical process where the formed oxidized species are also reduced back [27, 30].

On the contrary, Figure 4.8 (b) shows that the oxidative peak c is growing for the extended sweeps, but the reductive peak c' is not. As peak c' is associated with the reduction of NiOOH, it is suspected that this phase is less likely to be reduced due to overcharging and, therefore, being stabilized. As the sweep reaches potentials of -1.15 V vs. Hg/HgO, the NiOOH and other highly oxidized species can still be reduced due to the more aggressive cathodic polarization. The recovery of the activity suggests deactivation due to an oxidation process. However, which species form during this oxidation process has not been determined.

Reactions above 0.67 V vs. Hg/HgO include the formation from β to γ NiOOH. As γ NiOOH is more active than β NiOOH, this oxidation cannot explain the deactivation observed during overcharging [32]. Another reaction that is suggested to happen during overcharging is the formation of NiOO₂ related to the γ NiOOH structure

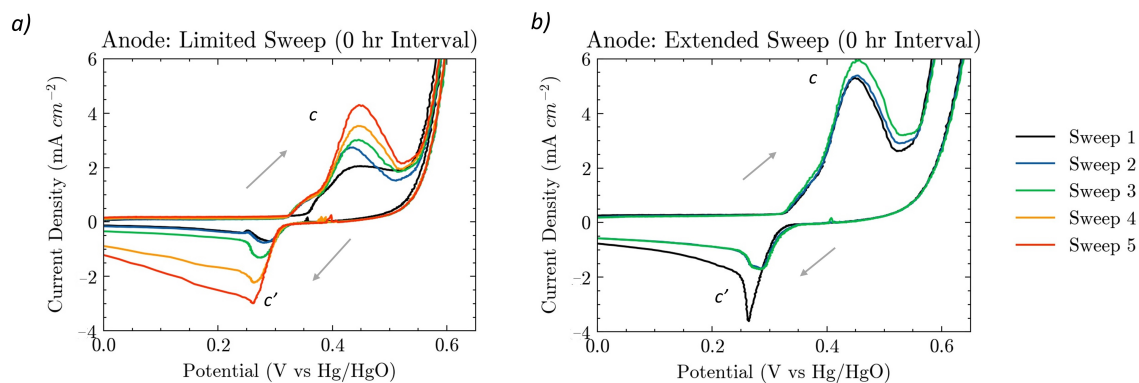


Figure 4.8: Cyclic voltammetry profiles of the anode and cathode derived from the overall cell voltage. Subfigure (a) depicts CVs measured before any electrolysis interval, featuring a distinct starting point. Scanning rate = 20 mV s^{-1} . Voltage range sweep = 2.2 to -1 V (cell potential). In contrast, subfigure (b) illustrates CVs measured after the charging intervals. The numbered arrows denote the sequence of the sweeps. Full CV in Figure I.1. Scanning rate = 20 mV s^{-1} . Voltage range sweep = 3.1 to -1 V (cell potential)

[32, 50]. The formation happens at 0.6 V vs. Hg/HgO, and the corresponding peak is visible after the 2-hr electrolysis interval indicated with * in Figure 4.9. Given that NiOO_2 was already present at the first crossing of the 30 mA cm^{-2} threshold, its formation cannot account for the observed hysteresis. Another process that could be the source of the deactivation is thickening of the NiO layer. From the current data there cannot be concluded if this is the source of deactivation.

The timescale of the development of the deactivation of 0.1 V within the extended sweep at 0-hr electrolysis interval is estimated at 3 minutes. This period aligns with the duration of potentials exceeding 0.67 V vs. Hg/HgO during the extended sweep. At the 0.5-hr interval, the hysteresis increased to 0.15 V. Despite a tenfold increase in electrolysis duration, hysteresis only grew by 1.5 times, suggesting its primary development occurs within the initial minutes. The effects beyond the 0.5-hr electrolysis interval remain ambiguous. This uncertainty arises because the potential impact of the CVs between the electrolysis intervals on the deactivation cannot be excluded.

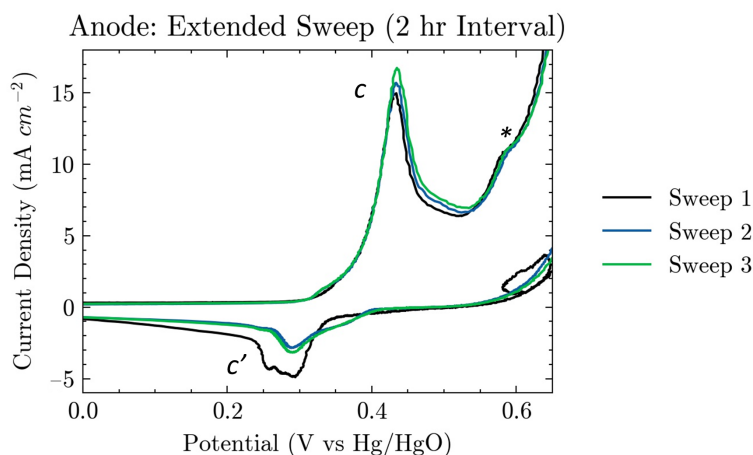


Figure 4.9: Cyclic voltammetry profiles of the anode after four 0.5 hr charge intervals. * denotes a new peak formed, which can be NiOO_2 [32, 50]. Full CV in Figure I.1. Scanning rate = 20 mV s^{-1} . Voltage Range = 3.1 to -1 V (cell potential)

4.2.3.3. Cathode Deactivation Mechanism

Figure 4.10 shows the cathodic potentials at 30 mA cm^{-2} . The following key observations are made:

- **Hysteresis of 0.3 V emerges within 0.5-hr:** A pronounced hysteresis effect becomes evident after the 0.5-hr electrolysis interval, compared to observations at the 0-hr interval. Over the three sweeps at the 0.5-hr interval, the magnitude of hysteresis diminishes progressively with each subsequent sweep. This observation suggests that the sustained hysteresis effect predominantly arises from extended durations at elevated loads.

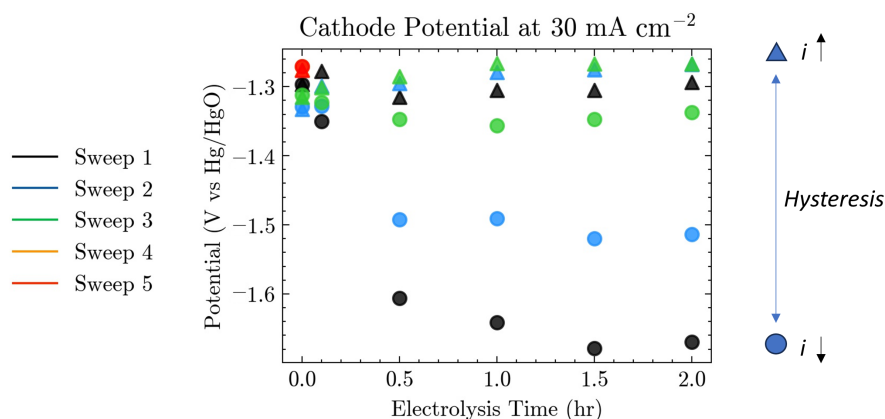


Figure 4.10: The cathodic potentials corresponding to 30 mA cm^{-2} during the CV sweep. Triangles denote an increasing electrolysis extent, while circles a decreasing one.

Moreover, the hysteresis grows beyond the initial 0.5-hr, implying that its full manifestation is not achieved within this timeframe. The complete extent and duration of the deactivation remain uncertain, given the potential influence of the sweeps occurring between the electrolysis intervals on the deactivation process.

Figure 4.11 showcases voltammograms from each interval. Comparing these to the 0-hr interval's final sweep (black line), which lacks significant hysteresis, provides insights. Notably, two peaks appear in the post-electrolysis intervals that are absent in the 0-hr interval:

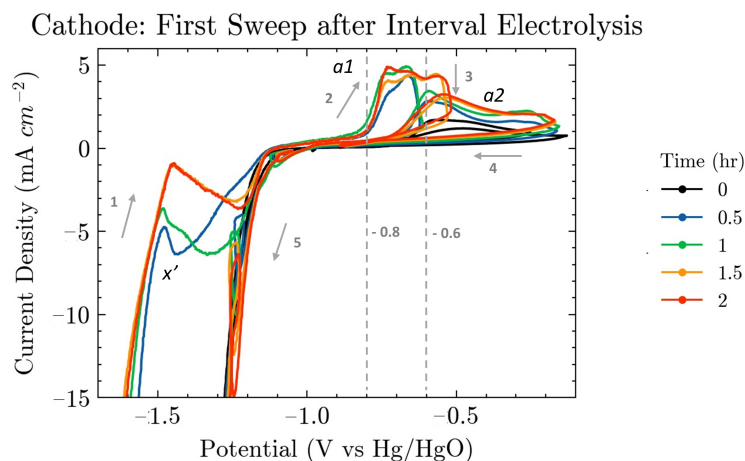


Figure 4.11: Cyclic voltammetry profiles of the cathode, utilizing the last sweep at the 0 hr electrolysis interval and employing the first sweep after each electrolysis interval (0.5, 1, 1.5, and 2 hr). Scanning rate = 20 mV s^{-1} . Voltage range = 3.1 to -1 V (cell potential)

- **Peak x'**: A reductive peak emerges between -1.5 and -1.2 V vs. Hg/HgO after the electrolysis interval. The β NiH decomposition within this voltage range is estimated (Table 2.3). Researchers have long suspected this species as the cause of substantial deactivation of nickel cathodes [17, 20, 34–36]. The observed reductive peak indicates that the peak corresponds to a decomposition process resulting in the formation of H_2 rather than H_2O , as the latter is associated with an oxidation process [36].
- **Peak a1**: As elaborated in Section 4.2.3.1, the cathodic peak a plays a pivotal role in circuit completion when the anode aims to reduce oxidized species. This demand for oxidizing currents arises twice during the sweep.

After the electrolysis interval, the first appearance of peak a, termed peak a1, is observed at a more negative potential of -0.8 V vs. Hg/HgO. The second time oxidative currents are required, the peak emerges at its typical value of -0.6 V vs. Hg/HgO, referred to as Peak a2. This behavior resembles the oxidation of metallic nickel [28].

At the potential corresponding to peak a1, the decomposition of α NiH is inferred, as detailed in Table 2.3. If peak x' indeed represents the β phase, the existence of the α phase, which is characterized by reduced hydrogen content in the nickel lattice, is possible [33]. Observing oxidative currents during the α phase decomposition suggests water generation.

- **Recoverable hysteresis and deactivation:** For the cathode, recovery is noticeable in both deactivation and hysteresis. Consistent potentials are observed upon crossing the 30 mA cm^{-2} threshold when increasing electrolysis, as depicted by the triangle markers. Similarly, a decrease in the observed difference when crossing the threshold suggests a recovery from hysteresis when comparing consecutive cycles after similar electrolysis intervals.

The recovery during the sweeps suggests that a reduction process causes the deactivation even as the hysteresis. Figure 4.12 illustrates the three CVs measured after the last electrolysis. Over subsequent cycles, both peak x' and peak a1 diminish. The decline in peaks x' and a1 coincides with the observed recovery in performance, attributed to the presence of NiH.

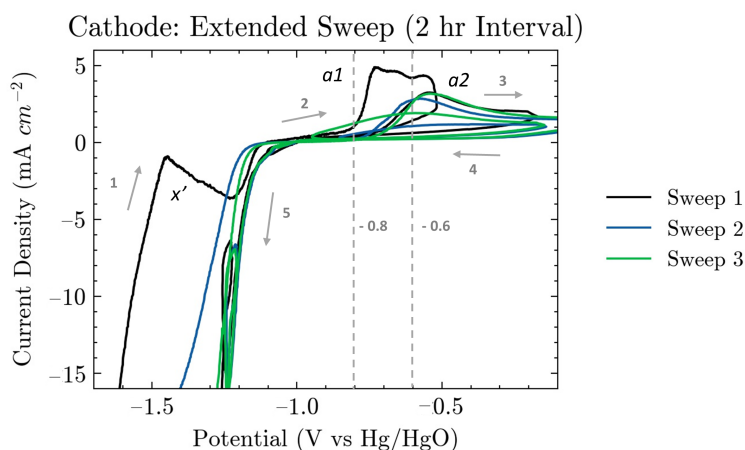


Figure 4.12: Cyclic voltammetry profiles of the anode after the last electrolysis interval. Scanning rate = 20 mV s^{-1} . Voltage range = 3.1 to -1 V (cell potential)

4.2.4. Interval Test: Tafel Slopes

The interval test employs increasing and decreasing voltage steps to derive polarization curves. The primary objective during this test is to obtain the kinetic parameters b (Tafel slope) and i_0 (exchange current density) from these polarization curves and examine their correlation with deactivation.

The subsequent section presents the outcomes of the extraction method applied to retrieve polarization curves from the voltage steps. Following that, the discussion focuses on the polarization curve of the anode, exploring the possible extraction of kinetic parameters. The succeeding subsection replicates this process for the cathode.

4.2.4.1. Extraction of Polarization Curves

This section provides the extraction method to obtain the polarization curves from the voltage steps. Figure 4.13 illustrates the period between the electrolysis intervals. This interval commences with cell voltage steps of 0.1 V for 15 seconds, ranging from 3.2 to 1.8 V. Subsequently, EIS measurements are conducted at a constant current density of 0.05 A cm^{-2} (refer to Section 4.2.5), followed by a similar step sequence with an increase in potential.

In Figure 4.13, the red dots represent the averaged potentials derived from the last 5 seconds of each step. A similar methodology is applied to extract the current values. The polarization curves are then constructed using these extracted points. It is important to note that the anode and cathode influence each other as the potential is controlled on the whole cell, not the individual electrode potentials.

The recorded data is not IR-corrected, as only the total cell resistance was measured. Consequently, at high currents, values may exhibit an upward deviation, reflecting the absence of correction for individual electrode resistances.

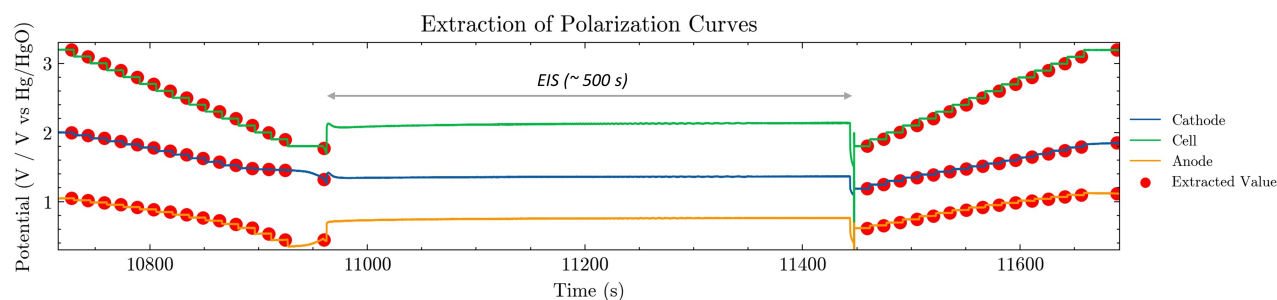


Figure 4.13: The time interval during electrolysis intervals 2 and 3, each lasting 0.5 hours at a current density of 1 A cm^{-2} . The red dots illustrate the potentials used for the polarization curves. The potential of the cathode is multiplied by minus 1 for visualization purposes.

4.2.4.2. Anode

Figure 4.14 (a) presents the polarization curves of the anode, with the dotted line representing the curve measured from decreasing potential steps and the continuous line from increasing potential steps. Notably, the anode's increasing curves commence at a higher potential than their decreasing counterparts, resulting from the interplay between the cathode and anode. Since the cathode appears to be the primary factor contributing to this disparity, a detailed discussion will follow in Section 4.2.4.3.

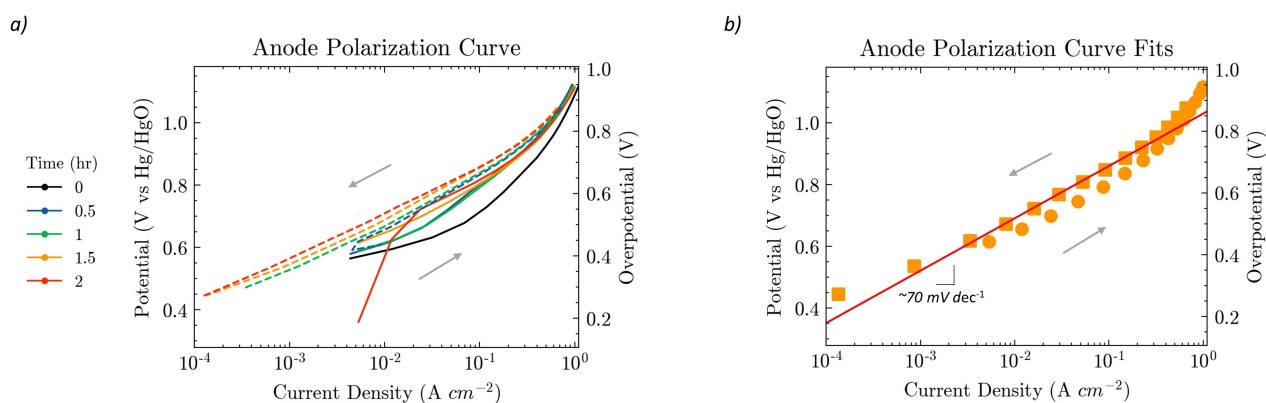


Figure 4.14: (a) Polarization curves of the anode with increasing (continuous lines) and decreasing (dotted lines) voltage measurements. (b) Fitting procedure for the decreasing polarization curve after the second electrolysis interval. Squares represent decreasing voltage measurements, while circles represent increasing ones.

Notably, the increasing curves lack a clear Tafel regime, as seen from the absence of a linear part in the log current density plot. The first curve (black continuous line) displays a significant deviation compared to the subsequent curves. This deviation is attributed to the initial overcharging experience of the electrode, leading to numerous oxidation reactions. These reactions contribute to the diverging shape of the first curve in contrast to the subsequent ones.

On the contrary, the decreasing curves exhibit a straight segment. At higher current densities, the deviation of the straight line is most likely due to ohmic effects. The fitted b values, representing the slope of the curves, are illustrated in Figure 4.15. The Tafel slope decreases after each electrolysis interval, dropping from 76 to 64 mV dec^{-1} . As shown in Table 2.2 from Chapter 2, a potential rate-determining step within this range of Tafel slopes involves the reaction:



In summary, exposure to 0.5-hour electrolysis intervals at 1 A cm^{-2} reduces the Tafel slope (b) for decreasing curves, while increasing curves lack a distinct Tafel regime. Based on the Tafel slope alone, insufficient information is available to determine the source of deactivation.

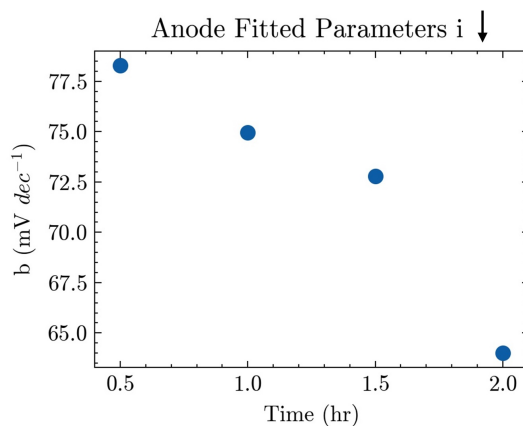


Figure 4.15: The fitted Tafel slopes (b) extracted from the decreasing curves after each electrolysis interval.

4.2.4.3. Cathode

Figure 4.16 (a) displays the polarization curves of the cathode, where the dotted line corresponds to measurements taken during decreasing potential steps, and the continuous line represents those from increasing potential steps. The dissimilarity in shape between the increasing and decreasing curves necessitates distinct approaches for extracting kinetic parameters from each set of curves.

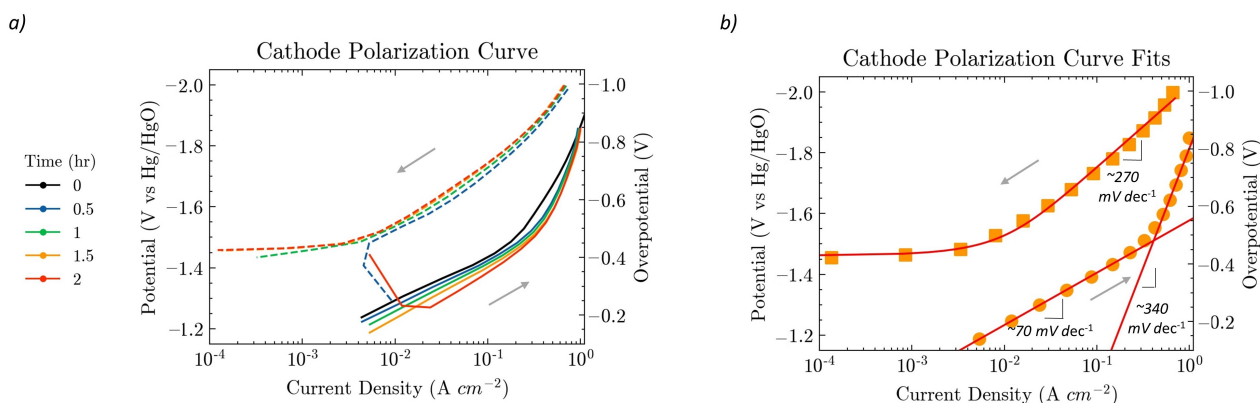


Figure 4.16: (a) Polarization curves of the cathode with increasing (continuous lines) and decreasing (dotted lines) voltage measurements. (b) Fitting procedure for the polarization curves after the 1-hr electrolysis interval. Squares represent decreasing voltage measurements fitted to Equation 4.2, while circles represent increasing ones fitted to the Tafel Equation 2.7.

Following electrolysis, a noticeable shift in equilibrium potential becomes evident. The inability of the decreasing curves to reach above -1.4 V vs. Hg/HgO indicates the establishment of this new equilibrium state. Only the curve measured after the initial electrolysis interval surpasses this value. The newly determined equilibrium potentials after electrolysis fall within the range of -1.3 to -1.5 V vs. Hg/HgO, coinciding with the appearance of the new CV peak attributed to β NiH.

The decreasing curve can be described using a function that reflects the potential's behavior near equilibrium, assuming the charge transfer coefficient is 0.5:

$$\eta = E_{\text{eq}} + \frac{b}{2.3} \cdot \operatorname{asinh}\left(\frac{i}{2 \cdot i_0}\right) \quad (4.2)$$

b is given in V dec⁻¹. Figure 4.16 (b) illustrates a fit example of this function to the experimental data, while Figure 4.17 (a) presents the extracted parameters following each electrolysis interval. The most notable difference emerges between the first and second charge intervals. After the first interval, the collapse of the newly found equilibrium potential suggests a less extensive formation of β NiH. The absence of this collapse indicates a more profound formation.

The discussion of the fitted parameters begins with the exchange current density. There is a notable reduction, halving from 0.00168 to 0.00859 A cm⁻² when comparing the first and second electrolysis intervals. The new

equilibrium potential exhibits a 20 mV increase, suggesting that a more enhanced or fully formed hydride leads to a higher equilibrium potential. Lastly, the Tafel slopes decrease from 299 to 261 mV dec^{-1} , exceeding typical HER values [43]. Soares et al. [17] linked similar high slopes to hydride-induced changes in reaction mechanisms. Thus, hydride formation likely influences the observed electrochemical behavior.

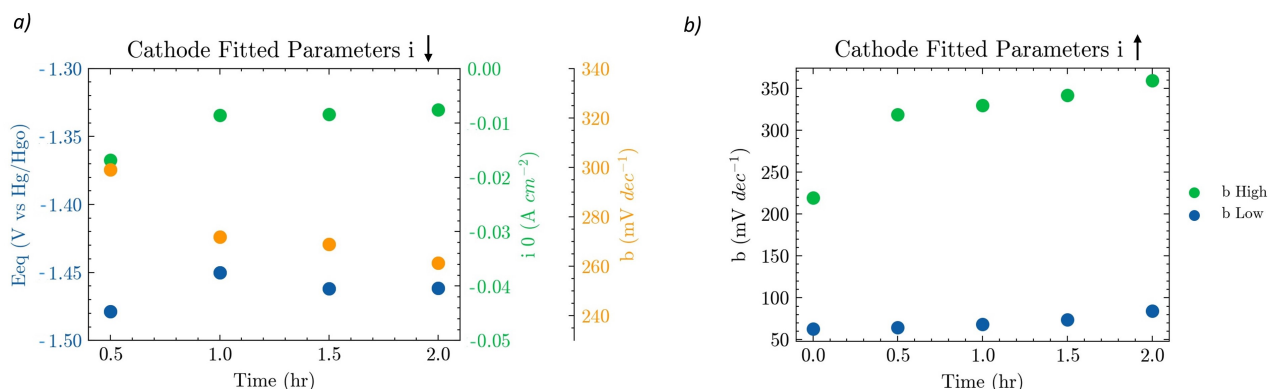


Figure 4.17: (a) The parameters from Equation 4.2 fitted to decreasing polarization curves of the cathode after each electrolysis interval. (b) The fitted Tafel slopes from the increasing curves of the cathode fitted as visualized in Figure 4.16 (b) by extracting the slope in two regions.

The increasing curve exhibits two straight segments, indicating two Tafel regions. In Figure 4.16, the fitting of this region demonstrates how the curve's slope yields both a low and a high Tafel slope. Figure 4.17 (b) outlines the fitted Tafel slopes for these regions. The low Tafel slopes increase from 62 to 84 mV dec^{-1} , while the high Tafel slopes increase from 219 to 349 mV dec^{-1} . Typical Tafel slopes for the HER are observed in the lower region [43]. For the higher region, Tafel slopes in similar order of magnitude are found as for the decreasing curves. The higher region starts from the newly established equilibrium potential and suggests that a similar underlying process is occurring, likely linked to the mechanism involving NiH.

The last increasing curve (red continuous line) initiates at a potential near the new equilibrium potential after electrolysis and lowers throughout the steps. This declining trend in potential suggests that the hydride is still decomposing, lowering the potential. When comparing the increasing curves over the course of electrolysis, a rising activity trend becomes evident, yet the exact cause remains unknown.

In summary, the cathode polarization curves revealed distinctive behavior, indicating the formation of a new equilibrium potential of -1.45 V vs Hg/HgO after electrolysis. The formation of β NiH was associated with a significant decrease in exchange current density and an increase in equilibrium potential. Post-electrolysis, activity slightly improved as NiH decomposed, enhancing H_2 production.

4.2.5. Interval Test: EIS

The interval test utilizes EIS to investigate the evolution of charge transfer resistance, ohmic resistance, and double-layer capacitance. The EIS measurements are conducted at a current density of 0.05 A cm^{-2} . The test protocol involves two consecutive measurements to ensure the system's stability and reliability. Subsequent sections will cover the validation and fitting of data, the results for ohmic resistance, and the outcomes for the anodic and cathodic processes. Determining which RC circuit corresponds to the anode and cathode is based on the measured potentials during the EIS measurements.

4.2.5.1. Validation and Fitting of Data

In this section, the validation and fitting process consists of examining the data's compliance with the Kramers and Kronig test, removing outliers, and fitting it to an equivalent circuit. The data undergoes a Kramers and Kronig test using the built-in function in Z-plot. Outlying data points are removed due to test failure. Figure I.3 illustrates an example of the raw data. The frequency range from 10 kHz to 1 Hz complies with Kramers and Kronig criteria. The constrained upper-frequency limit is unsurprising, given the increased error margin beyond 10 kHz for the low-impedance system, as depicted in the accuracy contour plot (Figure 3.7). The 1 Hz lower limit is implemented to avoid impedance data drift from an unstable system.

Figure 4.18 displays the Nyquist plots before and after the first electrolysis interval. The two semicircles observed before electrolysis merge after the electrolysis interval, suggesting a similar time scale for the electrodes. This merging introduces some uncertainty in parameter extraction. Fitting the data involves utilizing the equivalent circuit depicted in Figure 2.4. Figure I.4 and I.5 show the impedance data of Figure 4.18 with the fit.

Figure 4.20 (a) presents the extracted capacitances and (b) the resistances, with values corrected for the reactive surface area of the electrodes. Circles represent the first measurement, and triangles represent the second EIS measurement. While the in-sequence measurements show some instability, the data is deemed usable, given the slight differences between the triangles and the circles.

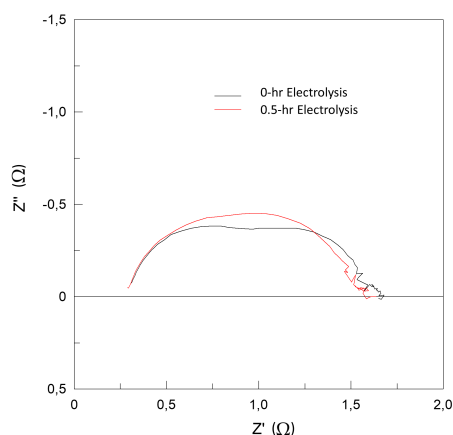


Figure 4.18: Kramers-Kronig compliant cell impedance data of the first cycles during the interval test at 0-hr and 0.5-hr electrolysis interval presented in a Nyquist plot. Current density: 0.05 A cm^{-2} . AC amplitude: 0.5 mA cm^{-2} .

4.2.5.2. Ohmic Resistance

The ohmic resistance remains relatively stable throughout the test at $0.30 \text{ } \Omega$ ($0.15 \text{ } \Omega \text{ cm}^{-2}$ when corrected for electrode area). This resistance primarily arises from the diaphragm and solution resistances, as expressed by:

$$R_{\text{ohm}} = R_{\text{zirfron}} + R_{\text{sol}} = 0.30 \text{ } \Omega \quad (4.3)$$

The Zirfron diaphragm's resistance is approximately $0.16 \text{ } \Omega \text{ cm}^2$ at $50 \text{ } ^\circ\text{C}$ [66]. The resistance of the solution is estimated by dividing the separation length between the two electrodes (1.2 cm) by the conductivity. The electrolyte conductivity is $95.3 \text{ } \Omega^{-1} \text{ m}^{-1}$ according to Equation 2.11 at 323 K and 6.9 M KOH ($30 \text{ wt}\%$).

The only unknown is the area where the current travels through between the electrodes (A):

$$\left(0.16 \text{ } \Omega \text{ cm}^2 + \frac{1.2 \text{ cm}}{0.953 \text{ } \Omega^{-1} \text{ cm}^{-1}}\right) \cdot \frac{1}{A} = 0.3 \text{ } \Omega \quad (4.4)$$

Solving Equation 4.4 yields an area of 4.7 cm^2 , notably exceeding the reactive area of 2 cm^2 . This spread in the current path is expected, as the diaphragm holder accommodates an 8.3 cm^2 hole within the PMMA, as illustrated in Figure 4.19. This simplification provides insight into the lower measured ohmic resistance.

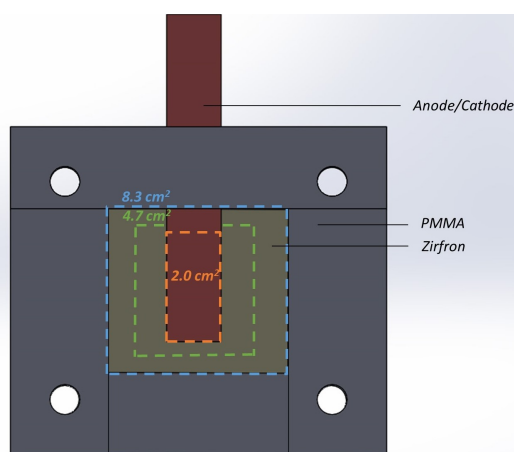


Figure 4.19: The electrode-diaphragm configuration shows distinct areas: Orange represents the electrode's reactive region, green illustrates the spread of the current path, and blue denotes the hole in the PMMA membrane holder.

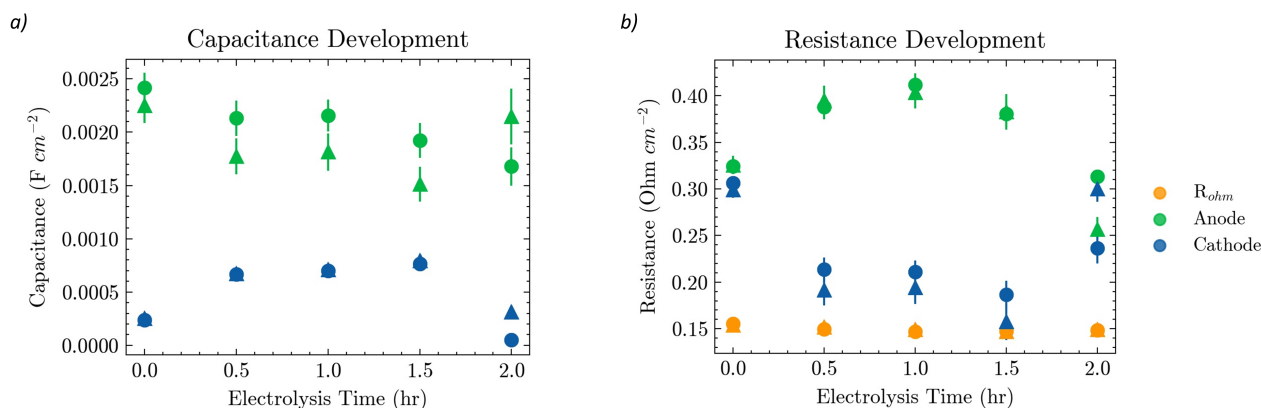


Figure 4.20: After each electrolysis interval of 1 A cm^{-2} , EIS measurements at 0.05 A cm^{-2} with an AC amplitude of 0.5 mA cm^{-2} provide the extracted parameters and fit errors. The capacitance and resistances displayed in subfigures (a) and (b), respectively, are corrected by the reactive area of 2 cm^2 . Circles represent the first measurement, and triangles represent the second EIS measurement.

4.2.5.3. Anode Results

The anodic potentials recorded during the EIS measurements were 0.68, 0.77, 0.76, 0.77, and 0.78 V vs. Hg/HgO, corresponding to the 0, 0.5, 1, 1.5, and 2-hour electrolysis intervals. The increasing trend in potentials suggests a decline in efficiency over time. In Figure 4.20, the green dots represent the anode, as the general increase in resistance mirrors the observed decrease in performance indicated by the anodic potentials.

However, an unexpected deviation from this trend becomes apparent after the last electrolysis interval. A decrease in charge transfer resistance is observed instead of an expected increase based on the potential trend. The decrease in charge transfer resistance aligns with the observed decrease in overpotential of the increasing tafel line after the last electrolysis interval (red continuous line in Figure 4.14 (a)). This consistency with the tafel analysis supports the accuracy of the EIS measurements.

The capacitance in Figure 4.20 is corrected for the geometrical reactive area. However, it is essential to note that due to the presence of pores, the total area is estimated at 7.3 cm^2 rather than 2 cm^2 (Appendix B). This adjustment in area has implications for the derived capacitance values. For the anode, the capacitance between 400 and $600 \mu\text{F cm}^{-2}$ is obtained when considering the total area, still exceeding the typical value for double-layer capacitance (20 - $40 \mu\text{F cm}^{-2}$ [8]). However, larger values between 200 to $1000 \mu\text{F cm}^{-2}$ are found in literature for nickel oxides and could be attributed to a large surface roughness [30, 67].

Figure 4.20 (a) shows that the anodic capacitances reduce slightly over the electrolysis intervals. Medway et al. [28] observed a similar trend and linked this to the thickening of NiO layer. They explained this by a simple Helmholtz layer model, illustrated in Figure 4.21. According to the model, the presence of the NiO layer restricts ion access to the nickel electrode. Conversely, hydrated forms of nickel ($\text{Ni}(\text{OH})_2$ or NiOOH) facilitate ion penetration, leading to an accumulation of counter ion charge. This charge separation correlates with the observed decrease in capacitance, given a constant dielectric constant (ϵ) for NiO ($C \propto \frac{\epsilon}{d}$).

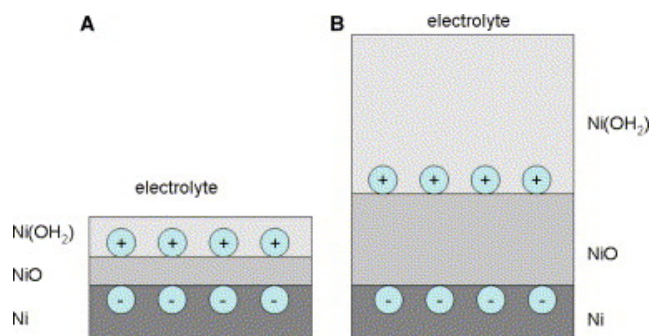


Figure 4.21: A schematic diagram of the simple Helmholtz model used to explain the drop in the anodic double layer capacitance. Source: Medway et al., 2006 [28]

In conclusion, the measured double-layer capacitance surpasses typical values by an order of magnitude, suggesting pronounced surface roughness or measurement errors. Although a slight decrease in capacitance hints at NiO layer thickening, its minimal magnitude prevents definitive conclusions.

4.2.5.4. Cathode Results

The cathodic potentials recorded during the EIS measurements are -1.39, -1.38, -1.36, -1.36, and -1.65 V vs. Hg/HgO after the 0, 0.5, 1, 1.5, and 2-hour electrolysis intervals. The increasing trend in the first four measurements suggests an enhancement in efficiency over time. In Figure 4.20, the blue dots represent the cathode as the decrease in resistance mirrors the increased activity. After the last electrolysis interval, a significantly more negative potential is seen, aligning with an increase in resistance. Tafel analysis (Section 4.2.4.3) speculates that the β NiH persists even after the EIS measurement. The presence of β NiH during the EIS measurement after the last electrolysis interval can explain the higher potentials of -1.65 compared to around -1.4 V vs. Hg/HgO.

Figure 4.20 (a) shows an increase in capacitance after each electrolysis interval for the first four measurements. An increase in capacitance can be due to growing surface roughness. Unfortunately, the SEM pictures were not made for the cathode. After correcting for the total estimated surface area (see Appendix B), the capacitance ranges between 70 and 200 $\mu\text{F cm}^{-2}$. This remains higher than the standard double-layer capacitance. However, such an elevated value could be attributed to factors like surface roughness or errors in the EIS measurement or estimation of the area. Hence, drawing conclusions from the EIS measurements is challenging.

4.2.6. Galvanostatic Long-Duration Tests

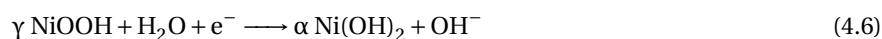
Examining voltage development over time at 1 A cm⁻², the galvanostatic long-duration tests aim to identify various deactivation timescales. The test comprises two cycles of 2.5 hours of electrolysis, each followed by a 15-minute rest. Three test series are utilized, with two featuring a 1-hour exposure time to the electrolyte before the current insertion and the other 20 hours. As demonstrated in Section 4.1, this exposure period does not significantly affect the deactivation trend; hence, all these tests are assumed to be similar.

Subsequent sections delve into the voltage development of the anode and cathode, focusing on identifying potential sources of material deactivation. The exclusion of double-layer capacitance from this analysis stems from the graph's data starting point at 0.1 seconds, which surpasses its relevant timescale [8]. Gas-related effects, such as bubbles obstructing ion pathways and covering portions of the reactive area, still play a role in early potential development [37, 38]. However, the estimation of their influence is minor because of the design, which allows the gas to escape very easily.

4.2.6.1. Anode Voltage-Time Development

This section analyzes the anode voltage-time evolution in the galvanostatic long-duration test, describing distinct timescales and proposing deactivation mechanisms. A comparison of the first and second electrolysis cycles reveals distinct regions in short, mid, and long timescales, as shown in Figure 4.23. The first cycle exhibits more profound deactivation in the short scale than the second round, while both cycles' mid and high timescales appear approximately similar. The rest period between the electrolysis cycles is examined to understand the differences in the cycle's initial state. Subsequently, the timescales are discussed, and a potential deactivation mechanism is proposed for each scale.

The decay tests after each cycle provide insights into the oxidized state of the electrode. The relatively slow decay behavior indicates that, in addition to the stored charge in the double layer, the additional charge is stored in the form of a higher oxidized state and adsorbed species on the surface [35, 36]. As the anodes experience large overcharging for 2.5 hours at high current densities, the outer surface is expected to consist of NiO, γ -NiOOH, higher oxidized species, and reaction intermediates. The decay process observed in Figure 4.22 is assumed to be the reduction of all these oxidized species. The reaction to complete the circuit is the anodic OER [68]. Considering the reduction of γ NiOOH, a potential redox couple is:



Equation 4.7 by Conway et al. [36] suggests a voltage decay by a tafel reaction. The formula illustrates the decay of the potential linearly with $\log(t + \tau)$, with τ a time delay. Within the first second, high slopes are observed in the order of 120 mV dec⁻¹. Up to 200 seconds, Tafel slopes around 85 mV dec⁻¹ are detected, indicating a shift in the rate-determining step or in surface coverage of the OER reaction intermediates [43].

$$V(t) \sim -b \cdot \log(t + \tau) \tag{4.7}$$

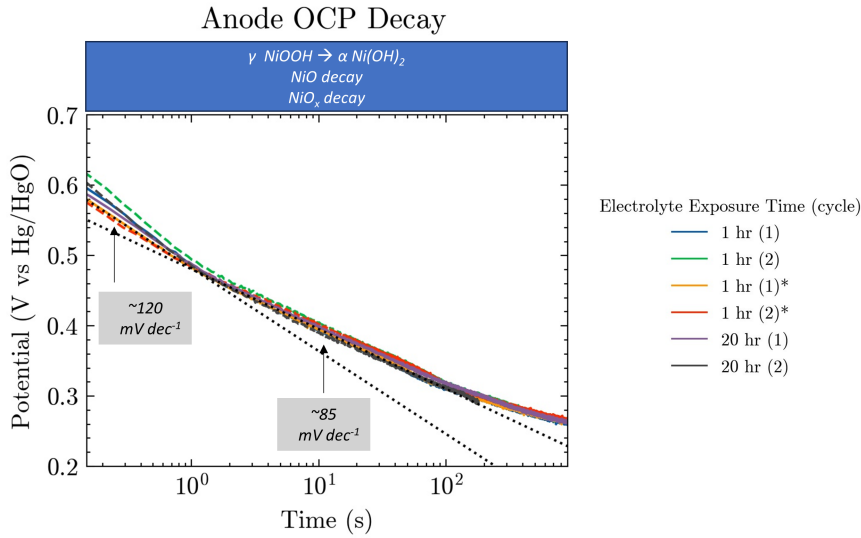


Figure 4.22: Anodic potential development after the long-duration test at 1 A cm^{-2} and $50 \text{ }^\circ\text{C}$, transitioning to open circuit conditions by removal of the current. The electrolyte exposure time is either 1 hour or 20 hours. The * denotes a duplicate test. Dotted lines visualize the second cycle. Smaller dotted lines represent the fits to obtain the slopes of the lines.

The decay curve flattens after 200 seconds but continues to decrease. According to Barnard et al. [31], the equilibrium potential is independent of the oxidation state between 12 and 60% of $\text{Ni(OH)}_2/\text{NiOOH}$. The absence of a sudden drop in potential, as observed in a similar decay curve after galvanostatic charging at 0.3 A cm^{-2} (Figure I.2), suggests that the oxidation state has not yet exceeded the lower limit of 12%. The potential has yet to stabilize; it is not expected that the oxidation state has reached the upper limit of 60%.

In summary, the distinction between the initial states of the cycles lies in the heightened oxidation state of the second cycle, primarily in the form of $\gamma\text{-NiOOH}$. This insight serves as a foundation for exploring distinct timescales in the voltage development during the subsequent electrolysis cycles at 1 A cm^{-2} shown in Figure 4.23:

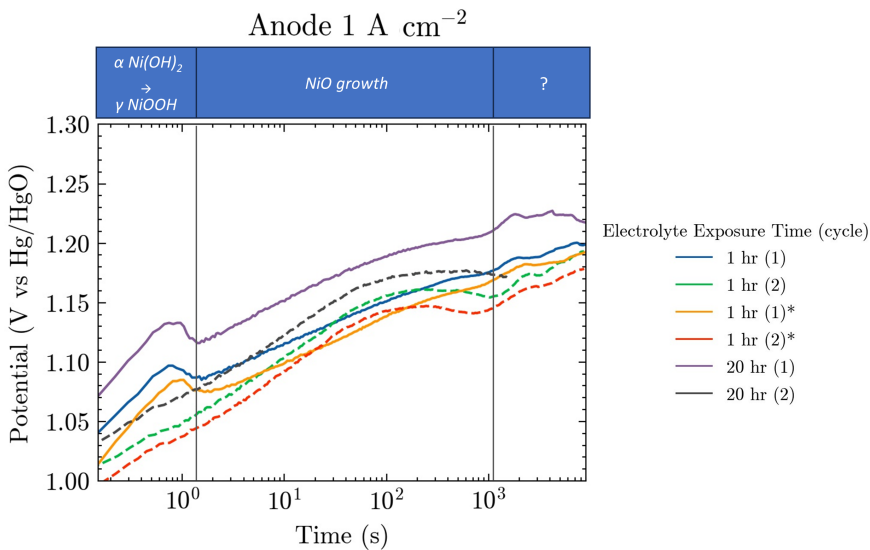


Figure 4.23: Charging period within the long-duration test of the anode at 1 A cm^{-2} at $50 \text{ }^\circ\text{C}$. The electrolyte exposure time is either 1 hour or 20 hours. The * denotes a duplicate test. Dotted lines visualize the second cycle.

- **0.1-1 Second Range:** The graph exhibits a rapid increase in overpotential for the first second, followed by a brief decrease. This region is notably less pronounced in the second cycle. The key distinction lies in the oxidation state between the initial states of the first and second cycles. The dominant process within this timescale is assumed to be the oxidation of $\text{Ni}(\text{OH})_2$ to NiOOH .
- **1 to 1000-Second Range:** Both cycles exhibit a similar trend in this range, indicating a deactivation process that recovers during the OCP period between the cycles. Deactivation due to impurities is unlikely because of this observed recovery. The initial potential increase followed by a flattening suggests NiO growth. Medway et al. [28] proposed that thickening of the oxide layer leads to self-limiting oxide growth, supporting the flattening behavior.
- **1000-9000 Second Range:** In the final segment of the charging curves, a systematic pattern features a sequential increase in potential, flattening, and another increase. The specific cause remains unknown. Kim et al. [24] explained the deactivation, activation, and deactivation pattern in their results by iron impurity leaching, causing cracks that enable the electrolyte to reach the unexposed nickel, leading to enhanced growth. However, the reversible deactivation in our case suggests a different mechanism that is less dependent on the presence of impurities due to limited amounts.

4.2.6.2. Cathode Voltage-Time development

A comparison of the first and second electrolysis cycles for the cathode reveals four distinct regions, as shown in Figure 4.25. Although the second cycle exhibits similar regions for various tests, their synchronization is no longer observed. The OCP period between the electrolysis cycles is examined to understand the difference between the initial state of the two cycles. Subsequently, the different regions of the voltage development over time are discussed, and a potential deactivation mechanism is proposed for each scale.

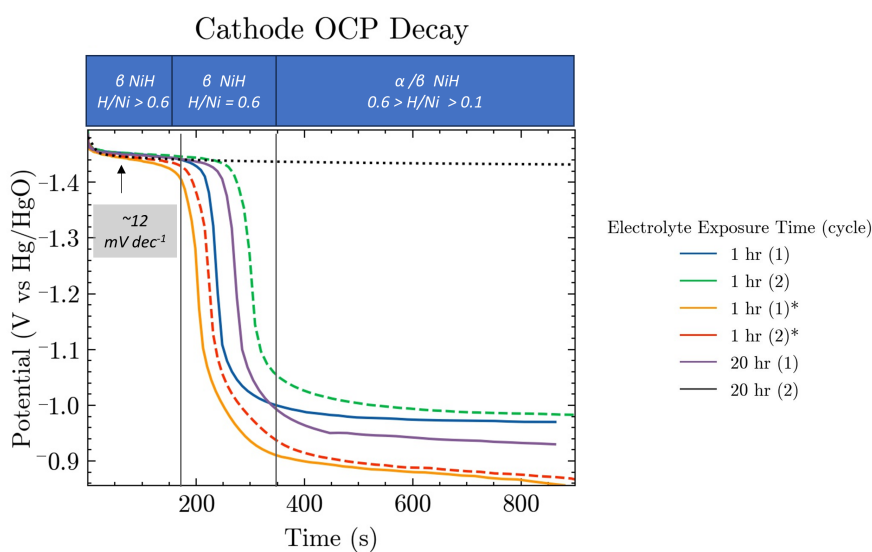


Figure 4.24: Cathodic potential development during the long-duration test of the cathode at 1 A cm^{-2} and 50°C , transitioning to open circuit conditions by removal of the current. The electrolyte exposure time is either 1 hour or 20 hours. The * denotes a duplicate test. Dotted lines visualize the second cycle.

The decay tests after each electrolysis cycle provide insights into the surface state of the cathode. The voltage during the rest period consists of a logarithmic decay, followed by a rapid potential drop, and ends with a slower decay (Figure 4.24). The voltage development during the rest period uses the decomposition of hydrides as an explanation:

- **Logarithmic decay:** In this region, the potential remains at similar levels as the new equilibrium potentials attributed to β NiH found in the Tafel analysis. The slow decay of several minutes could be due to the decay of β NiH to α NiH, resulting in a mixed phase [33]. The decay slope equals 12 mV dec^{-1} for all tests, independent of the cycle. Conway et al. [35] attributed unusually low decay slopes to the decomposition of NiH according to the coupled reaction 4.8 and 4.9. In their study, they derived theoretical proof for the low decay values compared to the Tafel slope, based on a fast anodic reaction and a slower Volmer step in the HER, resulting in

a slope of $2RT/5F$. This amounts still to double of what is observed here. The difference could be in the extent and time of electrolysis, which is significantly more in this study.



- **Sudden drop:** Within this region, the potential experiences a sudden drop attributed to crossing the atomic H/Ni ratio of 0.6 [33]. The potential where it drops varies for different samples. The decay of the second cycle has some delay, corresponding to a more developed hydride with a higher ratio of hydrogen in the lattice taking longer to reach the critical ratio to fall apart.
- **Last region:** This region suggests a continuous decrease in the H/Ni ratio. The ratio of 0.1 is not expected to be crossed as an additional jump would occur [33]. The curves all cross the HER equilibrium potential of $-1.052 \text{ V vs. Hg/HgO}$. The calculated potential is based on 30 wt% KOH at 50°C and does not account for the H_2 concentration (Appendix D). The potential remains a useful assumption even though the experiment's H_2 concentration is significantly lower than in the calculation. Below this potential, another redox reaction probably becomes predominant, given the diminishing likelihood of the HER. As indicated in Table 2.3, this could involve the decomposition of NiH under the formation of H_2 coupled with the hydrogen oxidation reaction, although alternative reactions are also possible. The blue curve seems to stabilize, suggesting the hydride decomposition stalled due to the inability of the HER to proceed, and the other unknown reaction cannot take over for some reason.

The cathodes with a more negative potential at the end of the rest period are assumed to have a higher H/Ni ratio. This information will be used to clarify the several regions observed in Figure 4.25 that will be discussed in the remaining paragraphs:

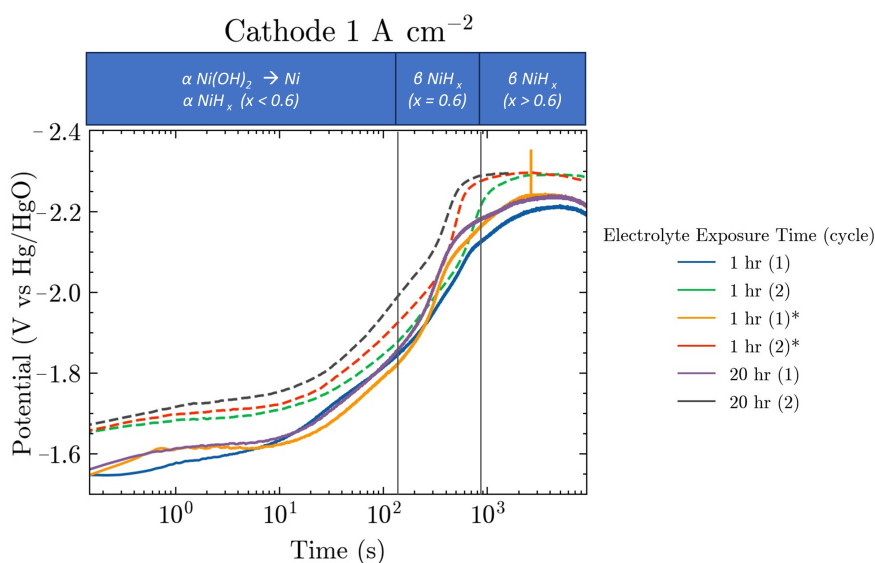


Figure 4.25: Charging period within the long-duration test of the cathode at 1 A cm^{-2} at 50°C . The electrolyte exposure time is either 1 hour or 20 hours. The * denotes a duplicate test. Dotted lines visualize the second cycle.

- **0.1-200 Second Range:** In the first region, the presence of Ni(OH)_2 reduced to metallic nickel contributes to the chaotic patterns observed in the first cycle. Contrastingly, the lines exhibit a more consistent pattern in the second cycle, where the surface lacks Ni(OH)_2 . The primary factor driving deactivation is incorporating hydrogen into the lattice of nickel. This process is prominent in the first cycle. In the second cycle, it is assumed that some NiH is already present, aligning with the initial less active state of the second cycle, as indicated by the higher potential [17].

- **200-700 Second Range:** During this period, a substantial potential jump occurs. Rommal et al. [18] observed a similar jump at current densities above 0.1 A cm^{-2} after 1000 to 10000 seconds dedicated to the formation of $\beta \text{ NiH}$. The difference in timing could be due to a lower temperature ($37 \text{ }^\circ\text{C}$) or intrinsic differences in the nickel electrodes used. Furthermore, a delay in the second cycle of the three tests is observed. It cannot be explained by initial hydrogen concentration as it does not align with the occurrence of delay established in the OCP analysis.
- **200-9000 Second Range:** In the last period, the curve flattens and becomes slightly negative towards the end. Juskenas et al. [34] suggested that the further absorption of hydrogen is done by converting the remaining α to $\beta \text{ NiH}$, causing a slight increase in potential in this region.

4.3. Effect of Current Density on the Voltage Losses over Time

This section delves into the relationship between current density and voltage losses over extended durations for nickel anodes and cathodes. The galvanostatic long-duration test was employed to assess the performance of fresh electrodes under constant industry-relevant current densities of 0.3, 0.5, and 1 A cm^{-2} (see Section 3.2.1). The analysis links the behavior of the electrolysis curves with subsequent rest period to the proposed deactivation mechanisms laid out in Section 4.2.6.

4.3.1. Anode

The charging curves during the long-duration test for the anode under various current densities are illustrated in Figure 4.26. A noticeable delay in deactivation is evident as the applied current density decreases. The delay is better visualized by extracting the slopes of the curves. Figure 4.27 presents these slopes plotted against time multiplied by current density resulting in charge density. Subsequent discussions will highlight patterns observed in both the first and second cycles.

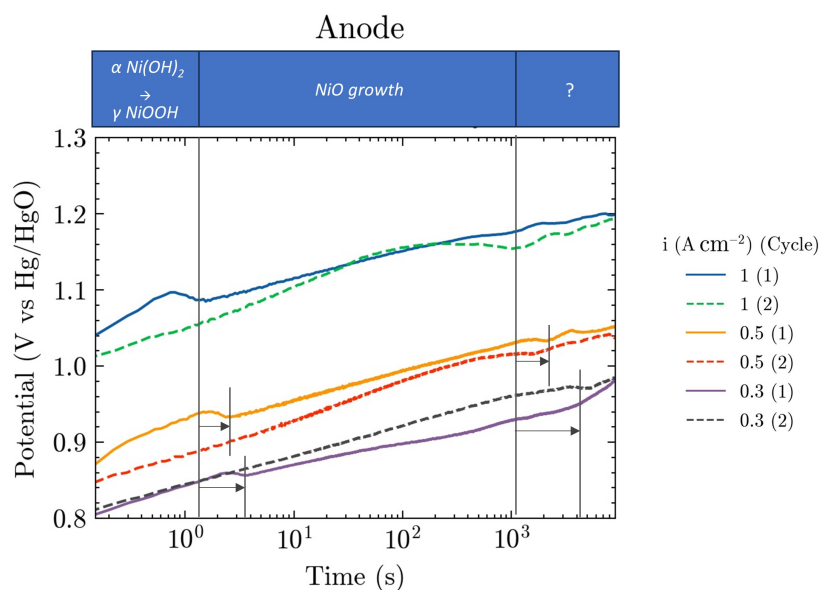


Figure 4.26: Charging period within the long-duration test of the cathode at $0.3, 0.5,$ and 1 A cm^{-2} at $50 \text{ }^\circ\text{C}$. For the 1 A cm^{-2} test, the duplicate test (*) from Figure 4.4 is selected.

In the context of the first cycle (Figure 4.27 (a)), synchronization improves when considering charge rather than time. The subsecond range is particularly noteworthy, where a slope increase is noted with higher current density. As discussed in Section 4.2.6, this behavior aligns with the proposed oxidation reaction of $\alpha \text{ Ni(OH)}_2$ to $\gamma \text{ NiOOH}$. This reaction is expected to occur at a higher current density when the electrolysis rate increases, resulting in a higher potential. Within the last region, the slope of the curves decreases with increasing current density. As there is no proposed mechanism here, this phenomenon remains unexplained.

Moving on to the second cycle (Figure 4.27 (b)), some delay in deactivation persists. A difference in oxidation state at the beginning of the second cycle could cause this enduring delay. Therefore, the following paragraphs focus on the decay periods after the first and second cycles to identify discrepancies.

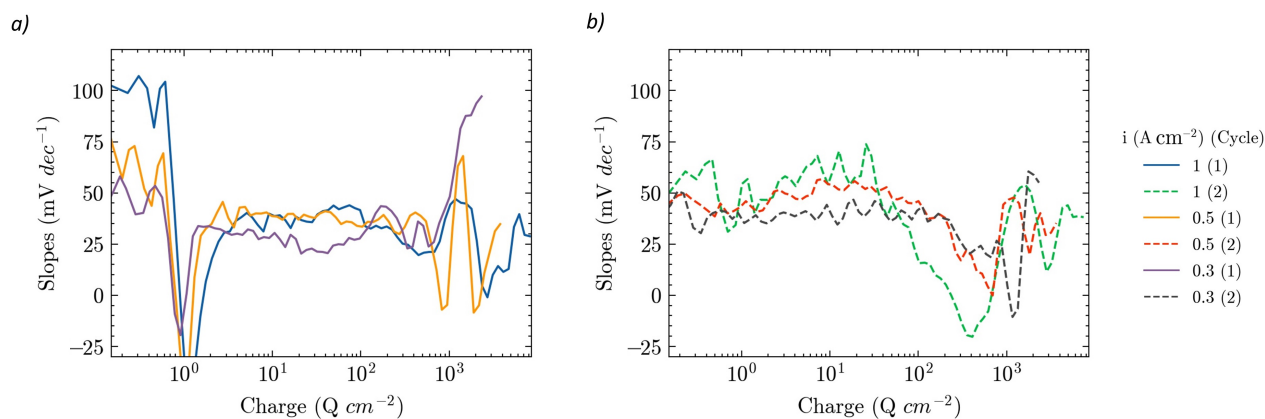


Figure 4.27: The voltage slopes with logarithmic in time of the charging period within the long-duration test of the anode at 0.3, 0.5, and 1 A cm⁻² at 50 °C. For the 1 A cm⁻² test, the duplicate test (*) from Figure 4.4 is selected.

Figure 4.28 shows the decay period of the first and second cycles. Significant differences emerge within the first 10 seconds, especially when comparing 0.3 A cm⁻² with the other two current densities. The former seems not to experience decay within this period and remains approximately stable around 0.42 V vs. Hg/HgO. The absence of decay after 0.3 A cm⁻² shows that the species that causes decay at the higher current density tests either decayed prior to the plotted period or was not formed. The exact identity of these species remains uncertain.

In summary, the anode's deactivation mechanisms are charge-dependent. Additionally, lower current densities (0.3 A cm⁻²) show either no formation or significantly lower quantities of unidentified species compared to the 0.5 and 1 A cm⁻² tests.

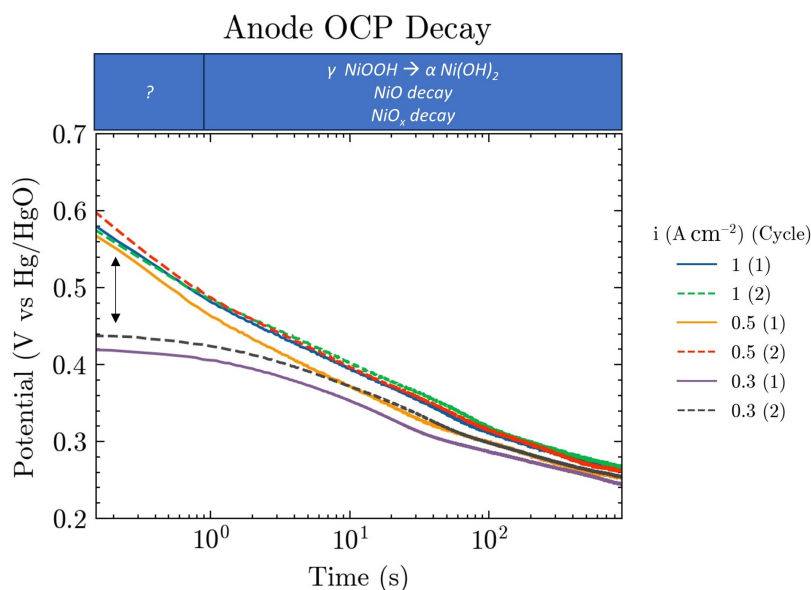


Figure 4.28: Anode potential development after a 2.5-hour electrolysis period at 0.3, 0.5, and 1 A cm⁻², transitioning to open circuit conditions by switching off the current. For each current density, fresh electrodes are used and exposed to two cycles of electrolysis. For the 1 A cm⁻² test, the duplicate test (*) from Figure 4.4 is selected.

4.3.2. Cathode

Figure 4.29 displays the charging curves for the long-duration test at 0.3, 0.5, and 1 A cm⁻². The three distinct deactivation regions observed in the cathode curves are present across all tests. Given the subtle trends and variations seen in the duplicate tests, as discussed in Section 4.2.6, conclusive remarks regarding the impact of current density on deactivation timing are not given. Nevertheless, similar deactivation mechanisms are at play, with deactivation extent increasing with higher current density — 0.65, 0.60, and 0.55 for 1, 0.5, and 0.3 A cm⁻², respectively.

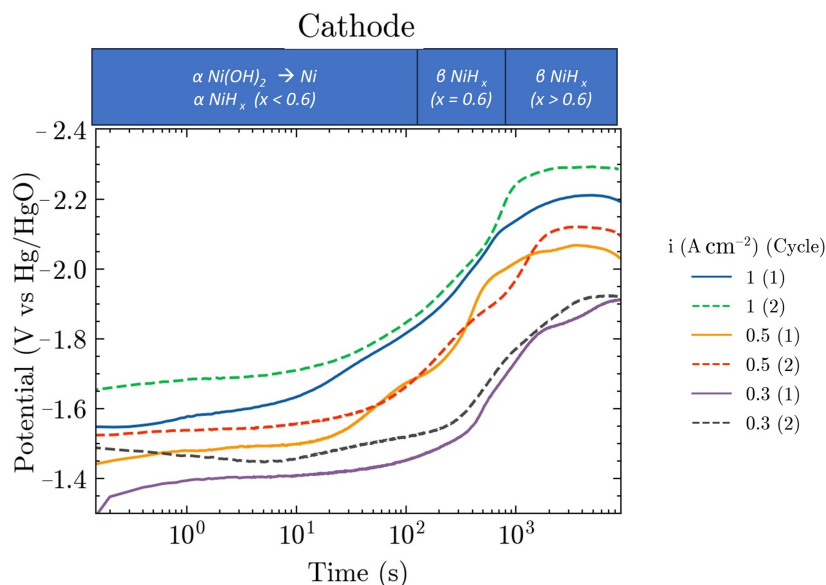


Figure 4.29: The voltage slopes with logarithmic in time of the charging period within the long-duration test of the cathode at 0.3, 0.5, and 1 A cm⁻² at 50 °C. For the 1 A cm⁻² test, the duplicate test (*) from Figure 4.4 is selected.

Figure 4.30 shows the potential after the current is switched off, with the proposed decay sequence annotated above the figure. Similar to the charging curves, the duplicate tests exhibit some variability in extent and timing in the OCP development after charging (refer to Section 4.2.6). This randomness complicates drawing specific conclusions about the impact of current density differences. However, the observed similar trends in all curves suggest that the proposed hydride-decomposing mechanism may be valid.

In summary, for current densities of 0.3, 0.5, and 1 A cm⁻² in the galvanostatic long-duration test, the cathode's deactivation mechanism appears similar, and the extent of deactivation is slightly higher for higher current densities.

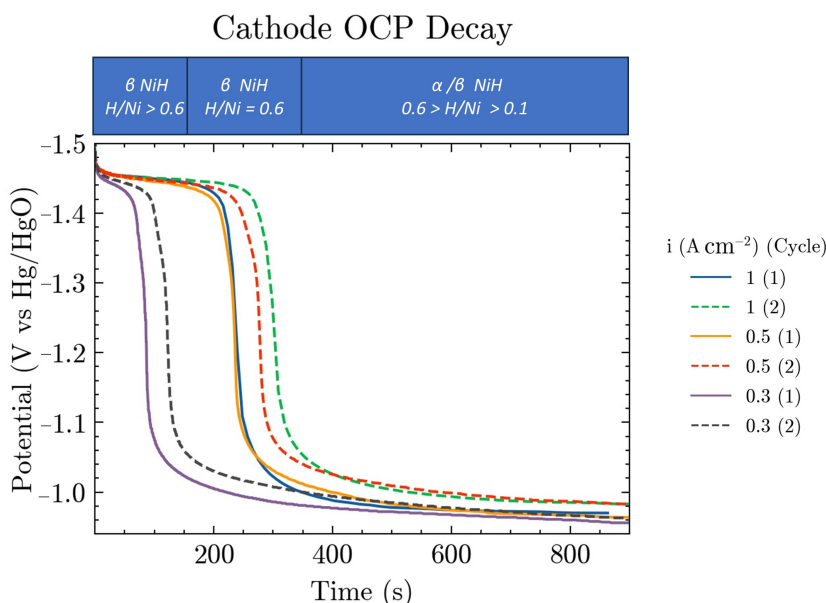


Figure 4.30: Cathode potential development after a 2.5-hour electrolysis period at 0.3, 0.5, and 1 A cm⁻², transitioning to open circuit conditions by switching off the current. For each current density, fresh electrodes are used and exposed to two cycles of electrolysis. For the 1 A cm⁻² test, the duplicate test (*) from Figure 4.2 is selected. Black dotted line represents fit with slope 12 mV dec⁻¹.

Conclusions and Recommendations

This study aimed to create a better understanding of the deactivation phenomena and their corresponding timescales in nickel electrodes during alkaline water electrolysis under near industry-relevant conditions. Three key research questions were addressed:

- **Can untreated, fresh nickel electrodes in alkaline water electrolysis yield reproducible results?**

The overall trend in the performance of untreated nickel electrodes proves reproducible (Section 4.1). However, caution is urged due to minor variations in constant voltage offsets during anodic charging. Precise conclusions about the timing of cathode deactivation require careful consideration due to observed deviations within the tests. A steady-state value for the anode is not achieved within 2.5 hours, whereas the cathode appears to stabilize within 10^3 seconds at a current density of 1 A cm^{-2} .

- **What deactivation phenomena are observed in nickel electrodes during galvanostatic charging in alkaline water electrolysis at an industry-relevant current density of 1 A cm^{-2} ? What are the corresponding timescales of these deactivation phenomena?**

Anode: Recoverable deactivation processes dominate, excluding impurities as the primary deactivation mechanism (Section 4.2.3.2 and 4.2.6.1). Figure 4.23 shows that initial deactivation, within a subsecond range, is linked to the formation $\gamma \text{ NiOOH}$ from $\alpha \text{ Ni(OH)}_2$. Deactivation from 1 to 1000 seconds is attributed to the growth of the NiO layer. Beyond 1000 seconds, uncertainties persist, warranting additional research.

Cathode: Recoverable deactivation processes dominate, with the primary cause identified as the formation of $\beta \text{ NiH}$ (Section 4.2.3.3, 4.2.4.3 and 4.2.6.2). Figure 4.25 shows that the first 200 seconds involve deactivation through the reduction of Ni(OH)_2 to less active metallic nickel, accompanied by the significant effect of hydrogen incorporation into the nickel lattice, forming $\alpha \text{ NiH}$. A substantial potential jump arises between 200 and 700 seconds due to the formation of $\beta \text{ NiH}$. Further hydrogen uptake occurs, continuing the deactivation. Future research could explore factors contributing to the unexplained activation observed at the test's end.

- **How does the current density impact the voltage losses of a nickel anode and cathode over galvanostatic long-duration tests at industry-relevant current densities?**

For the anode, deactivation trends align consistently with the inserted charge density (Section 4.3.1). The cathode exhibits a slightly higher deactivation extent at higher current densities (Section 4.3.2). Due to the lack of reproducible timing in duplicate experiments for the anode and reproducible extent in the cathode, these are the primary conclusions (Section 4.1).

The following recommendations aim to enhance understanding and provide valuable insights for practical applications in alkaline water electrolysis.:

- **Extended Testing Duration:** Conduct longer-duration tests to capture deactivation trends and assess whether steady-state conditions are achieved. The tests in this study only extended up to 2.5 hours, where a stable potential was not always reached for the anode steady state.
- **Temperature Variation:** Given the industry's standard temperature of $80 \text{ }^\circ\text{C}$, future investigations should explore deactivation phenomena at this higher temperature instead of $50 \text{ }^\circ\text{C}$.
- **Characterization after Different Electrolysis Intervals:** Structural changes in the interval of electrochemical characterization tests, currently after only 0.5 hours of charging, could provide insights into the extent of deactivation after a specific time.

- **Explore Additional Current Densities:** Test a broader range of current densities, beyond the examined 0.3, 0.5, and 1 A cm⁻², for a more comprehensive understanding of deactivation behavior. Especially higher current densities are of interest to see if this can accelerate the stabilization time.
- **Zero Gap Configuration:** Conduct experiments using a zero gap configuration to determine if the material's performance is affected by intensified gas effects.
- **Diaphragm Consistency:** Investigate the consistency of the Zirfron diaphragm, as notable variations were observed in its performance throughout this study.

Bibliography

- [1] “Monthly Global Climate Report for Annual 2022,” NOAA National Centers for Environmental Information, Tech. Rep., Jan. 2023. [Online]. Available: <https://www.ncei.noaa.gov/access/monitoring/monthly-report/global/202213>
- [2] S. Griffiths, B. K. Sovacool, J. Kim, M. Bazilian, and J. M. Uratani, “Industrial decarbonization via hydrogen: A critical and systematic review of developments, socio-technical systems and policy options,” *Energy Research & Social Science*, vol. 80, p. 102208, Oct. 2021. [Online]. Available: <https://www.sciencedirect.com/science/article/pii/S2214629621003017>
- [3] V. A. Panchenko, Y. V. Daus, A. A. Kovalev, I. V. Yudaev, and Y. V. Litti, “Prospects for the production of green hydrogen: Review of countries with high potential,” *International Journal of Hydrogen Energy*, vol. 48, no. 12, pp. 4551–4571, Feb. 2023. [Online]. Available: <https://www.sciencedirect.com/science/article/pii/S0360319922047309>
- [4] V. M. Maestre, A. Ortiz, and I. Ortiz, “Challenges and prospects of renewable hydrogen-based strategies for full decarbonization of stationary power applications,” *Renewable and Sustainable Energy Reviews*, vol. 152, p. 111628, Dec. 2021. [Online]. Available: <https://www.sciencedirect.com/science/article/pii/S1364032121009035>
- [5] B. N. van Haersma Buma, M. Peretto, Z. M. Matar, and G. van de Kaa, “Towards renewable hydrogen-based electrolysis: Alkaline vs Proton Exchange Membrane,” *Heliyon*, vol. 9, no. 7, p. e17999, Jul. 2023. [Online]. Available: <https://www.ncbi.nlm.nih.gov/pmc/articles/PMC10395340/>
- [6] M. Gong and H. Dai, “A mini review of NiFe-based materials as highly active oxygen evolution reaction electrocatalysts,” *Nano Research*, vol. 8, no. 1, pp. 23–39, Jan. 2015. [Online]. Available: <https://doi.org/10.1007/s12274-014-0591-z>
- [7] Y. Deng, W. Lai, and B. Xu, “A Mini Review on Doped Nickel-Based Electrocatalysts for Hydrogen Evolution Reaction,” *Energies*, vol. 13, no. 18, Jan. 2020. [Online]. Available: <https://www.mdpi.com/1996-1073/13/18/4651>
- [8] A. J. Bard and L. R. Faulkner, *Electrochemical methods: fundamentals and applications*, 2nd ed. New York: Wiley, 2001.
- [9] J. H. Lim, J. Hou, J. Chun, R. D. Lee, J. Yun, J. Jung, and C. H. Lee, “Importance of Hydroxide Ion Conductivity Measurement for Alkaline Water Electrolysis Membranes,” *Membranes*, vol. 12, no. 6, p. 556, Jun. 2022. [Online]. Available: <https://www.mdpi.com/2077-0375/12/6/556>
- [10] Fraunhofer, “Elektrolyse,” 2023. [Online]. Available: <https://www.ifam.fraunhofer.de/de/Ueberuns/Standorte/Dresden/Wasserstofftechnologie/elektrolyse.html>
- [11] X. G. Jiang, Y. P. Zhang, C. Song, Y. C. Xie, T. K. Liu, C. M. Deng, and N. N. Zhang, “Performance of nickel electrode for alkaline water electrolysis prepared by high pressure cold spray,” *International Journal of Hydrogen Energy*, vol. 45, no. 58, pp. 33 007–33 015, Nov. 2020. [Online]. Available: <https://www.sciencedirect.com/science/article/pii/S036031992033411X>
- [12] Y. Zhang, Y. Liu, M. Ma, X. Ren, Z. Liu, G. Du, A. M. Asiri, and X. Sun, “A Mn-doped Ni₂P nanosheet array: an efficient and durable hydrogen evolution reaction electrocatalyst in alkaline media,” *Chemical Communications*, vol. 53, no. 80, pp. 11 048–11 051, Sep. 2017. [Online]. Available: <https://pubs.rsc.org/en/content/articlelanding/2017/CC/C7CC06278H>
- [13] W. Zhu, X. Yue, W. Zhang, S. Yu, Y. Zhang, J. Wang, and J. Wang, “Nickel sulfide microsphere film on Ni foam as an efficient bifunctional electrocatalyst for overall water splitting,” *Chemical Communications*, vol. 52, no. 7, pp. 1486–1489, Nov. 2016. [Online]. Available: <https://pubs.rsc.org/en/content/articlelanding/2016/CC/C5CC08064A>

- [14] S.-Y. Lee, H.-J. Oh, M. Kim, H.-S. Cho, and Y.-K. Lee, "Insights into enhanced activity and durability of hierarchical Fe-doped Ni(OH)₂/Ni catalysts for alkaline oxygen evolution reaction: In situ XANES studies," *Applied Catalysis B: Environmental*, vol. 324, p. 122269, May 2023. [Online]. Available: <https://www.sciencedirect.com/science/article/pii/S0926337322012103>
- [15] J. Huang, S. Wen, G. Chen, W. Chen, G. Wang, H. Fan, D. Chen, C. Song, M. Li, X. Wang, L. Li, M. Tao, B. Li, X. Wang, and K. K. Ostrikov, "Multiphase Ni-Fe-selenide nanosheets for highly-efficient and ultra-stable water electrolysis," *Applied Catalysis B: Environmental*, vol. 277, p. 119220, Nov. 2020. [Online]. Available: <https://www.sciencedirect.com/science/article/pii/S0926337320306354>
- [16] J. D. Holladay, J. Hu, D. L. King, and Y. Wang, "An overview of hydrogen production technologies," *Catalysis Today*, vol. 139, no. 4, pp. 244–260, Jan. 2009. [Online]. Available: <https://www.sciencedirect.com/science/article/pii/S0920586108004100>
- [17] D. M. Soares, O. Teschke, and I. Torriani, "Hydride Effect on the Kinetics of the Hydrogen Evolution Reaction on Nickel Cathodes in Alkaline Media," *Journal of The Electrochemical Society*, vol. 139, no. 1, p. 98, Jan. 1992. [Online]. Available: <https://iopscience.iop.org/article/10.1149/1.2069207/meta>
- [18] H. E. G. Rommal and P. J. Morgan, "The Role of Absorbed Hydrogen on the Voltage-Time Behavior of Nickel Cathodes in Hydrogen Evolution," *Journal of The Electrochemical Society*, vol. 135, no. 2, pp. 343–346, Feb. 1988. [Online]. Available: <https://iopscience.iop.org/article/10.1149/1.2095612>
- [19] R. M. Abouatallah, D. W. Kirk, and J. W. Graydon, "Long-term electrolytic hydrogen permeation in nickel and the effect of vanadium species addition," *Electrochimica Acta*, vol. 47, no. 15, pp. 2483–2494, Jun. 2002. [Online]. Available: <https://www.sciencedirect.com/science/article/pii/S0013468602001081>
- [20] M. Bernardini, N. Comisso, G. Davolio, and G. Mengoli, "Formation of nickel hydrides by hydrogen evolution in alkaline media," *Journal of Electroanalytical Chemistry*, vol. 442, no. 1, pp. 125–135, Jan. 1998. [Online]. Available: <https://www.sciencedirect.com/science/article/pii/S0022072897004920>
- [21] J. P. Diard, B. LeGorrec, and S. Maximovitch, "Etude de l'activation du degagement d'hydrogene sur electrode d'oxyde de nickel par spectroscopie d'impedance," *Electrochimica Acta*, vol. 35, no. 6, pp. 1099–1108, Jun. 1990. [Online]. Available: <https://www.sciencedirect.com/science/article/pii/0013468690900496>
- [22] J. P. Diard, P. Landaud, B. Le Gorrec, and C. Montella, "Calculation, simulation and interpretation of electrochemical impedance: Part II. Interpretation of Volmer-Heyrovsky impedance diagrams," *Journal of Electroanalytical Chemistry and Interfacial Electrochemistry*, vol. 255, no. 1, pp. 1–20, Nov. 1988. [Online]. Available: <https://www.sciencedirect.com/science/article/pii/0022072888800019>
- [23] M. F. Kibria, M. S. Mridha, and A. H. Khan, "Electrochemical studies of a nickel electrode for the hydrogen evolution reaction," *International Journal of Hydrogen Energy*, vol. 20, no. 6, pp. 435–440, Jun. 1995. [Online]. Available: <https://www.sciencedirect.com/science/article/pii/0360319994000739>
- [24] J. E. Kim, T. H. Kim, C. S. Park, K. Jung, J. Yoon, K. B. Lee, and K. S. Kang, "Probing the (de)activation of Raney nickel-iron anodes during alkaline water electrolysis by accelerated deactivation testing," *Electrochemistry Communications*, vol. 157, p. 107601, Dec. 2023. [Online]. Available: <https://www.sciencedirect.com/science/article/pii/S1388248123001753>
- [25] M. Demnitz, Y. M. Lamas, R. L. Garcia Barros, A. de Leeuw den Bouter, J. van der Schaaf, and M. Theodorus de Groot, "Effect of iron addition to the electrolyte on alkaline water electrolysis performance," *iScience*, vol. 27, no. 1, p. 108695, Jan. 2024. [Online]. Available: <https://www.sciencedirect.com/science/article/pii/S2589004223027724>
- [26] L. F. Huang, M. J. Hutchison, R. J. J. Santucci, J. R. Scully, and J. M. Rondinelli, "Improved Electrochemical Phase Diagrams from Theory and Experiment: The Ni-Water System and Its Complex Compounds," *The Journal of Physical Chemistry C*, vol. 121, no. 18, pp. 9782–9789, May 2017. [Online]. Available: <https://doi.org/10.1021/acs.jpcc.7b02771>
- [27] M. E. G. Lyons, R. L. Doyle, I. Godwin, M. O'Brien, and L. Russell, "Hydrous Nickel Oxide: Redox Switching and the Oxygen Evolution Reaction in Aqueous Alkaline Solution," *Journal of The Electrochemical Society*, vol. 159, no. 12, p. H932, Oct. 2012. [Online]. Available: <https://iopscience.iop.org/article/10.1149/2.078212jes/meta>

- [28] S. L. Medway, C. A. Lucas, A. Kowal, R. J. Nichols, and D. Johnson, "In situ studies of the oxidation of nickel electrodes in alkaline solution," *Journal of Electroanalytical Chemistry*, vol. 587, no. 1, pp. 172–181, Feb. 2006. [Online]. Available: <https://www.sciencedirect.com/science/article/pii/S0022072805005693>
- [29] A. J. Tkalych, K. Yu, and E. A. Carter, "Structural and Electronic Features of $-\text{Ni}(\text{OH})_2$ and $-\text{NiOOH}$ from First Principles," *The Journal of Physical Chemistry C*, vol. 119, no. 43, pp. 24 315–24 322, Oct. 2015. [Online]. Available: <https://doi.org/10.1021/acs.jpcc.5b08481>
- [30] M. E. G. Lyons and M. P. Brandon, "The Oxygen Evolution Reaction on Passive Oxide Covered Transition Metal Electrodes in Aqueous Alkaline Solution. Part 1-Nickel," *Int. J. Electrochem. Sci.*, vol. 3, no. 12, pp. 1386–1424, Jun. 2008. [Online]. Available: [https://doi.org/10.1016/S1452-3981\(23\)15531-3](https://doi.org/10.1016/S1452-3981(23)15531-3)
- [31] R. Barnard, C. F. Randell, and F. L. Tye, "Studies concerning charged nickel hydroxide electrodes I. Measurement of reversible potentials," *Journal of Applied Electrochemistry*, vol. 10, no. 1, pp. 109–125, Jan. 1980. [Online]. Available: <https://doi.org/10.1007/BF00937345>
- [32] L. Trotochaud, S. L. Young, J. K. Ranney, and S. W. Boettcher, "Nickel–Iron Oxyhydroxide Oxygen-Evolution Electrocatalysts: The Role of Intentional and Incidental Iron Incorporation," *Journal of the American Chemical Society*, vol. 136, no. 18, pp. 6744–6753, Apr. 2014. [Online]. Available: <https://pubs.acs.org/doi/10.1021/ja502379c>
- [33] Z. Szklarska-Smialowska and M. Smialowski, "Electrochemical Study of the Nickel-Hydrogen System," *Journal of The Electrochemical Society*, vol. 110, no. 5, p. 444, Jun. 1963. [Online]. Available: <https://iopscience.iop.org/article/10.1149/1.2425783>
- [34] R. Jusknas, A. Selskis, and V. Kadziauskien, "In situ X-ray diffraction investigation of nickel hydride formation during cathodic charging of Ni," *Electrochimica Acta*, vol. 43, no. 12, pp. 1903–1911, May 1998. [Online]. Available: <https://www.sciencedirect.com/science/article/pii/S0013468697003046>
- [35] B. E. Conway, H. Angerstein-Kozłowska, M. A. Sattar, and B. V. Tilak, "Study of a Decomposing Hydride Phase at Nickel Cathodes by Measurement of Open-Circuit Potential Decay," *Journal of The Electrochemical Society*, vol. 130, no. 9, pp. 1825–1836, Sep. 1983. [Online]. Available: <https://iopscience.iop.org/article/10.1149/1.2120106>
- [36] B. E. Conway, L. Bai, and D. F. Tessier, "Data collection and processing of open-circuit potential-decay measurements using a digital oscilloscope: Derivation of the H-capacitance behaviour of H_2 -evolving, Ni-based cathodes," *Journal of Electroanalytical Chemistry and Interfacial Electrochemistry*, vol. 161, no. 1, pp. 39–49, Feb. 1984. [Online]. Available: <https://www.sciencedirect.com/science/article/pii/S002207288480248X>
- [37] J. W. Haverkort and H. Rajaei, "Voltage losses in zero-gap alkaline water electrolysis," *Journal of Power Sources*, vol. 497, p. 229864, Jun. 2021. [Online]. Available: <https://www.sciencedirect.com/science/article/pii/S037877532100402X?via%3Dihub>
- [38] X. Deng, F. Yang, Y. Li, J. Dang, and M. Ouyang, "Quantitative study on gas evolution effects under large current density in zero-gap alkaline water electrolyzers," *Journal of Power Sources*, vol. 555, p. 232378, Jan. 2023. [Online]. Available: <https://www.sciencedirect.com/science/article/pii/S0378775322013556>
- [39] A. E. Mauer, D. W. Kirk, and S. J. Thorpe, "The role of iron in the prevention of nickel electrode deactivation in alkaline electrolysis," *Electrochimica Acta*, vol. 52, no. 11, pp. 3505–3509, Mar. 2007. [Online]. Available: <https://www.sciencedirect.com/science/article/pii/S0013468606011029>
- [40] K. J. Vetter, *Electrochemical Kinetics: Theoretical and Experimental Aspects*. Academic Press, 1967.
- [41] C. Henao, K. Agbossou, M. Hammoudi, Y. Dubé, and A. Cardenas, "Simulation tool based on a physics model and an electrical analogy for an alkaline electrolyser," *Journal of Power Sources*, vol. 250, pp. 58–67, Mar. 2014. [Online]. Available: <https://ui.adsabs.harvard.edu/abs/2014JPS...250...58H>
- [42] N. Mahmood, Y. Yao, J.-W. Zhang, L. Pan, X. Zhang, and J.-J. Zou, "Electrocatalysts for Hydrogen Evolution in Alkaline Electrolytes: Mechanisms, Challenges, and Prospective Solutions," *Advanced Science*, vol. 5, no. 2, p. 1700464, Nov. 2018. [Online]. Available: <https://onlinelibrary.wiley.com/doi/abs/10.1002/advs.201700464>

- [43] T. Shinagawa, A. T. Garcia-Esparza, and K. Takanabe, "Insight on Tafel slopes from a microkinetic analysis of aqueous electrocatalysis for energy conversion," *Scientific Reports*, vol. 5, no. 1, p. 13801, Sep. 2015. [Online]. Available: <https://www.nature.com/articles/srep13801>
- [44] N. Krstajić, M. Popović, B. Grgur, M. Vojnović, and D. Šepa, "On the kinetics of the hydrogen evolution reaction on nickel in alkaline solution: Part I. The mechanism," *Journal of Electroanalytical Chemistry*, vol. 512, no. 1, pp. 16–26, Oct. 2001. [Online]. Available: <https://www.sciencedirect.com/science/article/pii/S0022072801005903>
- [45] G. Kreysa, B. Hakansson, and P. Ekdunge, "Kinetic and thermodynamic analysis of hydrogen evolution at nickel electrodes," *Electrochimica Acta*, vol. 33, no. 10, pp. 1351–1357, Oct. 1988. [Online]. Available: <https://www.sciencedirect.com/science/article/pii/0013468688801257>
- [46] I. J. Godwin and M. E. G. Lyons, "Enhanced oxygen evolution at hydrous nickel oxide electrodes via electrochemical ageing in alkaline solution," *Electrochemistry Communications*, vol. 32, pp. 39–42, Jul. 2013. [Online]. Available: <https://www.sciencedirect.com/science/article/pii/S1388248113001318>
- [47] S. Anantharaj, S. Kundu, and S. Noda, "'The Fe Effect': A review unveiling the critical roles of Fe in enhancing OER activity of Ni and Co based catalysts," *Nano Energy*, vol. 80, p. 105514, Feb. 2021. [Online]. Available: <https://www.sciencedirect.com/science/article/pii/S2211285520310880>
- [48] D. Friebe, M. W. Louie, M. Bajdich, K. E. Sanwald, Y. Cai, A. M. Wise, M.-J. Cheng, D. Sokaras, T.-C. Weng, R. Alonso-Mori, R. C. Davis, J. R. Bargar, J. K. Nørskov, A. Nilsson, and A. T. Bell, "Identification of Highly Active Fe Sites in (Ni,Fe)OOH for Electrocatalytic Water Splitting," *Journal of the American Chemical Society*, vol. 137, no. 3, pp. 1305–1313, Jan. 2015. [Online]. Available: <https://doi.org/10.1021/ja511559d>
- [49] N. Elgrishi, K. J. Rountree, B. D. McCarthy, E. S. Rountree, T. T. Eisenhart, and J. L. Dempsey, "A Practical Beginner's Guide to Cyclic Voltammetry," *Journal of Chemical Education*, vol. 95, no. 2, pp. 197–206, Nov. 2017. [Online]. Available: <https://pubs.acs.org/doi/10.1021/acs.jchemed.7b00361>
- [50] K. Juodkazi, J. Juodkazytė, and R. Vilkauskaitė, "Nickel surface anodic oxidation and electrocatalysis of oxygen evolution | SpringerLink," *Journal of solid state chemistry*, vol. 12, pp. 1469–1479, Jan. 2008. [Online]. Available: <https://link.springer.com/article/10.1007/s10008-007-0484-0>
- [51] D. S. Hall, C. Bock, and B. R. MacDougall, "The Electrochemistry of Metallic Nickel: Oxides, Hydroxides, Hydrides and Alkaline Hydrogen Evolution," *Journal of The Electrochemical Society*, vol. 160, no. 3, p. F235, Jan. 2013. [Online]. Available: <https://iopscience.iop.org/article/10.1149/2.026303jes/meta>
- [52] A. Lasia, *Electrochemical Impedance Spectroscopy and its Applications*. New York, NY: Springer, Jun. 2014. [Online]. Available: <https://link.springer.com/10.1007/978-1-4614-8933-7>
- [53] A. C. Lazanas and M. I. Prodromidis, "Electrochemical Impedance Spectroscopy A Tutorial," *ACS Measurement Science Au*, vol. 3, no. 3, pp. 162–193, Jun. 2023. [Online]. Available: <https://doi.org/10.1021/acsmeasuresciau.2c00070>
- [54] B. Boukamp and J. Rossmacdonald, "Alternatives to Kronig-Kramers transformation and testing, and estimation of distributions," *Solid State Ionics*, vol. 74, no. 1-2, pp. 85–101, Dec. 1994. [Online]. Available: <https://linkinghub.elsevier.com/retrieve/pii/0167273894904405>
- [55] B. A. Boukamp, "A Linear Kronig-Kramers Transform Test for Immittance Data Validation," *Journal of The Electrochemical Society*, vol. 142, no. 6, pp. 1885–1894, Jun. 1995. [Online]. Available: <https://iopscience.iop.org/article/10.1149/1.2044210>
- [56] "Potassium hydroxide ACS reagent," Sep. 2024. [Online]. Available: <https://www.sigmaaldrich.com/NL/en/product/sigald/221473>
- [57] "1287A | Potentiostat Galvanostat | Solartron Analytical." [Online]. Available: <https://www.ameteksi.com/products/potentiostats/single-channel/12xx-series/1287a-potentiostat-galvanostat>
- [58] T. Malkow, A. Pilenga, and G. Tsotridis, "EU harmonised test procedure: electrochemical impedance spectroscopy for water electrolysis cells," *JRC Publications Repository*, Mar. 2019. [Online]. Available: <https://publications.jrc.ec.europa.eu/repository/handle/JRC107053>

- [59] "USB-6001 Specifications - NI." [Online]. Available: <https://www.ni.com/docs/en-US/bundle/usb-6001-specs/resource/374369a.pdf>
- [60] "1255B | Frequency Response Analyzer | Solartron Analytical." [Online]. Available: <https://www.ameteksi.com/products/frequency-response-analyzers/1255b-frequency-response-analyzer>
- [61] K. Kawashima, R. A. Márquez, Y. J. Son, C. Guo, R. R. Vaidyula, L. A. Smith, C. E. Chukwuneke, and C. B. Mullins, "Accurate Potentials of Hg/HgO Electrodes: Practical Parameters for Reporting Alkaline Water Electrolysis Overpotentials," *ACS Catalysis*, vol. 13, no. 3, pp. 1893–1898, Feb. 2023. [Online]. Available: <https://doi.org/10.1021/acscatal.2c05655>
- [62] M. Yu, E. Budiyanto, and H. Tüysüz, "Principles of Water Electrolysis and Recent Progress in Cobalt-, Nickel-, and Iron-Based Oxides for the Oxygen Evolution Reaction," *Angewandte Chemie International Edition*, vol. 61, no. 1, p. e202103824, Jun. 2022. [Online]. Available: <https://onlinelibrary.wiley.com/doi/abs/10.1002/anie.202103824>
- [63] J. G. Baker, J. R. Schneider, J. A. Garrido Torres, J. A. Singh, A. J. M. Mackus, M. Bajdich, and S. F. Bent, "The Role of Aluminum in Promoting Ni–Fe–OOH Electrocatalysts for the Oxygen Evolution Reaction," *ACS Applied Energy Materials*, vol. 2, no. 5, pp. 3488–3499, May 2019. [Online]. Available: <https://doi.org/10.1021/acsaem.9b00265>
- [64] J. Kubisztal and A. Budniok, "Study of the oxygen evolution reaction on nickel-based composite coatings in alkaline media," *International Journal of Hydrogen Energy*, vol. 33, no. 17, pp. 4488–4494, Sep. 2008. [Online]. Available: <https://www.sciencedirect.com/science/article/pii/S0360319908007386>
- [65] M. Salahshoor and Y. Guo, "Biodegradable Orthopedic Magnesium-Calcium (MgCa) Alloys, Processing, and Corrosion Performance," *Materials*, vol. 5, pp. 135–155, Dec. 2012. [Online]. Available: <https://www.ncbi.nlm.nih.gov/pmc/articles/PMC5448945/>
- [66] M. de Groot and A. Vreman, "Ohmic resistance in zero gap alkaline electrolysis with a Zirfon diaphragm," *Electrochimica Acta*, vol. 369, p. 137684, Dec. 2020. [Online]. Available: http://www.vremanresearch.nl/deGroot_Vreman_EA2021_OhmicResistanceZeroGapAlkalineElectrolysis.pdf
- [67] A. C. Garcia, T. Touzalin, C. Nieuwland, N. Perini, and M. T. M. Koper, "Enhancement of Oxygen Evolution Activity of Nickel Oxyhydroxide by Electrolyte Alkali Cations," *Angewandte Chemie International Edition*, vol. 58, no. 37, pp. 12 999–13 003, Jun. 2019. [Online]. Available: <https://onlinelibrary.wiley.com/doi/abs/10.1002/anie.201905501>
- [68] B. V. Tilak and B. E. Conway, "Overpotential decay behavior—I. Complex electrode reactions involving adsorption," *Electrochimica Acta*, vol. 21, no. 10, pp. 745–752, Oct. 1976. [Online]. Available: <https://www.sciencedirect.com/science/article/pii/0013468676850050>
- [69] J. N. Hausmann, B. Traynor, R. J. Myers, M. Driess, and P. W. Menezes, "The pH of Aqueous NaOH/KOH Solutions: A Critical and Non-trivial Parameter for Electrocatalysis," *ACS Energy Letters*, vol. 6, no. 10, pp. 3567–3571, Oct. 2021. [Online]. Available: [https://doi.org/10.1021/acsenergylett.1c01693](https://doi.org/10.1021/acseenergylett.1c01693)
- [70] J. A. Richardson and A. A. Abdullahi, "Corrosion in Alkalis," in *Reference Module in Materials Science and Materials Engineering*. Elsevier, Jan. 2018. [Online]. Available: <https://www.sciencedirect.com/science/article/pii/B978012803581810520X>
- [71] Choi, H. Cho, Moon, J.-W. Kang, Oh, and K. Lee, "Recent Developments in the Recycling of Spent Selective Catalytic Reduction Catalyst in South Korea," *Catalysts*, vol. 10, p. 182, Feb. 2020. [Online]. Available: <https://www.mdpi.com/2073-4344/10/2/182>
- [72] M. Fousová, V. Valesova, and D. Vojtech, "Corrosion of 3D-printed AlSi9Cu3Fe alloy," *Manufacturing Technology*, vol. 19, pp. 29–36, Mar. 2019. [Online]. Available: https://www.researchgate.net/publication/331722518_Corrosion_of_3D-printed_AlSi9Cu3Fe_alloy
- [73] M. Haghani and S. Daneshpazhuh, "A Novel Multi-Step Purification Method for Production of Profitable Food Grade Phosphoric Acid and Ammonium Based Fertilizers from a Sedimentary Ore," *International Journal of Environmental Analytical Chemistry*, vol. 7, no. 4, pp. 2380–2391, Sep. 2020.

A

Electrolyte Impurities

	Type	Weight Percentage (wt%)
Impurities	Water	10-15
	Potassium Carbonate	≤ 2.0
	Nitrogen Compounds	≤ 0.001
Cation Traces	Calcium	≤ 0.005
	Iron	≤ 0.001
	Magnesium	≤ 0.002
	Sodium	≤ 0.005
	Nickel	≤ 0.001
	Heavy Metals	≤ 0.001
Anion Traces	Chloride	≤ 0.01
	Phosphate	$\leq 5\text{ppm}$
	Sulphate	≤ 0.003

Table A.1: Impurities present KOH pellets from ACS reagent with a purity level exceeding 85 wt% [56].

B

Veco Electrode Specifications

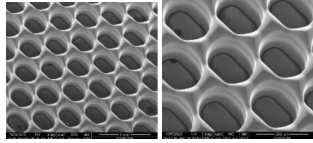
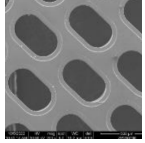
Number	Aperture dimensions	Open area	Thickness	Pillar side	Flat side
ZP200736	0.27 x 0.14 mm	41 %	0.6 mm		

Table B.1: Veco electrode specifications.

Estimation of total reactive surface area: Due to the porous structure of the material, as illustrated in Table B.1, the effective surface area exceeds the 2 cm² geometric area. Figure B.1 (b) shows that the pores can be conceptualized as two half circles and a square. The area and circumference of a single pore are calculated as:

$$\text{Area} = \pi \cdot \left(\frac{0.014}{2}\right)^2 + 0.014 \cdot 0.027 = 0.00053 \text{ cm}^2 \quad (\text{B.1})$$

$$\text{Circumference} = (0.014\pi + 0.027 \cdot 2) \cdot 0.06 = 0.0059 \text{ cm}^2 \quad (\text{B.2})$$

The area is subtracted twice for each pore, but the circumference area compensates for this removal. Thus, considering 41% as the open area, the net increase in area due to the pores is:

$$2 \cdot 0.41 \cdot \frac{0.0059}{2 \cdot 0.00053} = 4.6 \text{ cm}^2 \quad (\text{B.3})$$

Taking into account the area without the pores and the edges of the reactive zone, the estimated total surface area is:

$$4.6 + 2 \cdot 2 \cdot (1 - 0.41) + 0.06 \cdot (2 + 1 + 2) = 7.3 \text{ cm}^2 \quad (\text{B.4})$$

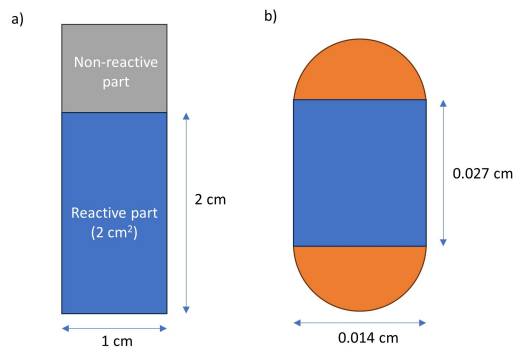


Figure B.1: (a) The geometry of the electrode. (b) The geometry of a single pore which is present in the electrode.

C

Problems with NI DAQ 6008

The original idea was to measure the potential of the electrodes with the NI DAQ 6008. However, problems were observed with the measurements involving a Hg/HgO reference electrode. In figure C.1, a sudden potential drop after 440 seconds is seen in the signals cathode vs. reference electrode 1 (cathodic side), anode vs. reference electrode 1, and the reference electrode 2 (anodic side) vs. reference electrode 1 (dRE). Reference electrodes have a high impedance compared to the electrodes part of the water-splitting reaction. The high impedance of reference electrodes prevents large currents from running through the reference electrode, which can damage them [61]. It is suggested that the input impedance of the DAQ was too low, causing a current distribution of the measured signal and the input impedance.

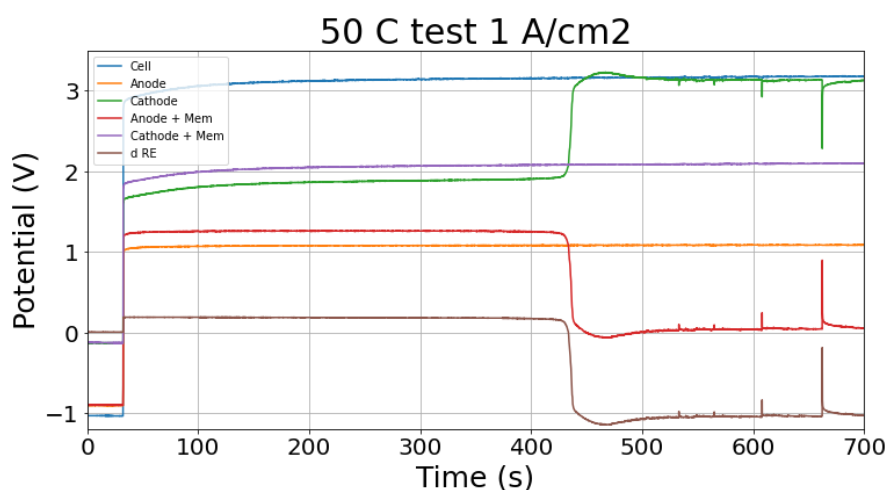


Figure C.1: Data visualizing the failure of the DAQ 6008 of National Instruments altering bypassing the measuring circuit due to a too low input impedance of the DAQ.

When the input impedance of the measuring device is of the same magnitude as the signal to be measured, part of the measurement current is split over the two parallel paths. The splitting of current means that part of the measuring current flows through the input resistance, affecting the potential. The following observations strengthen this hypothesis: The measurement current was 20 mA before the potential drop. When the drop happened, the measurement current dropped to 13 mA, indicating that the part of the current was bypassing this path. When the NI DAQ 6001 was installed, this phenomenon was not present. The input impedance of this device is around 1 G Ohm instead of 144 k Ohm [59].

What is still uncertain is the delay before the collapse of the potential, indicating a specific capacitance is in the system. An explanation could be the liquid junction of ions that form over the glass frit [61]. Inside the reference electrode, a 1 M NaOH solution is present. A glass frit separates this solution from the 30 wt% KOH electrolyte. Due to the concentration and type of ion difference, a junction forms with capacitive behavior. However, this is expected to happen in a shorter time scale than is experienced. Another explanation could be a capacitor inside the DAQ itself.

D

Conversion of Reference Electrode Potentials

The anode and cathode potentials are measured versus a Hg/HgO reference electrode. Potentials of reactions that are relevant are often mentioned versus another reference electrode. The conversion of the literature mentioned references to the Hg/HgO reference are given [61]:

$$E_{\text{Hg/HgO}} = E_{\text{RHE}} - \frac{2.303RT}{F} \cdot \text{pH} - E_{0 \text{ Hg/HgO}} = E_{\text{RHE}} - \frac{2.303RT}{F} - 0.108$$

$$E_{\text{Hg/HgO}} = E_{\text{SHE}} - E_{0 \text{ Hg/HgO}} = E_{\text{SHE}} - 0.108$$

$$E_{\text{Hg/HgO}} = E_{\text{SCE}} + E_{0 \text{ SCE}} - E_{0 \text{ Hg/HgO}} = E_{\text{SCE}} + 0.241 - 0.108 = E_{\text{SCE}} + 0.133$$

Where R is the gas constant of $8.314 \text{ J mol}^{-1} \text{ K}^{-1}$, T is the temperature in K, and F is the Faraday constant of 96485 C mol^{-1} . $E_{0 \text{ Hg/HgO}}$ is the standard electrode reduction potential of Hg/HgO and depends on the internal solutions composition and concentration. A 1 M NaOH internal solution equals around 0.108 V, which is the solution used. $E_{0 \text{ SCE}}$ is the standard electrode reduction potential of the saturated calomel electrode and is equal to 0.241 V.

The most important reactions in a water electrolysis cell are the HER and OER. Therefore, the equilibrium potential in the conditions in the cell will be calculated as they will be used later on. The conditions in the cell are 323 K, ambient pressure, and a concentration of 30 wt% KOH. This results in a pH of 14.8 [69]. The dependency of the OER and HER on the conditions above is:

$$E_{\text{OER}} = E_{0 \text{ OER}} - \frac{2.303RT}{F} \cdot \text{pH} - E_{0 \text{ Hg/HgO}} = 1.23 - 0.949 - 0.108 = 0.173 \text{V vs. Hg/HgO}$$

$$E_{\text{HER}} = E_{0 \text{ HER}} - \frac{2.303RT}{F} \cdot \text{pH} - E_{0 \text{ Hg/HgO}} = 0 - 0.949 - 0.108 = -1.052 \text{V vs. Hg/HgO}$$

E

Temperature of Results of Long-Duration Test

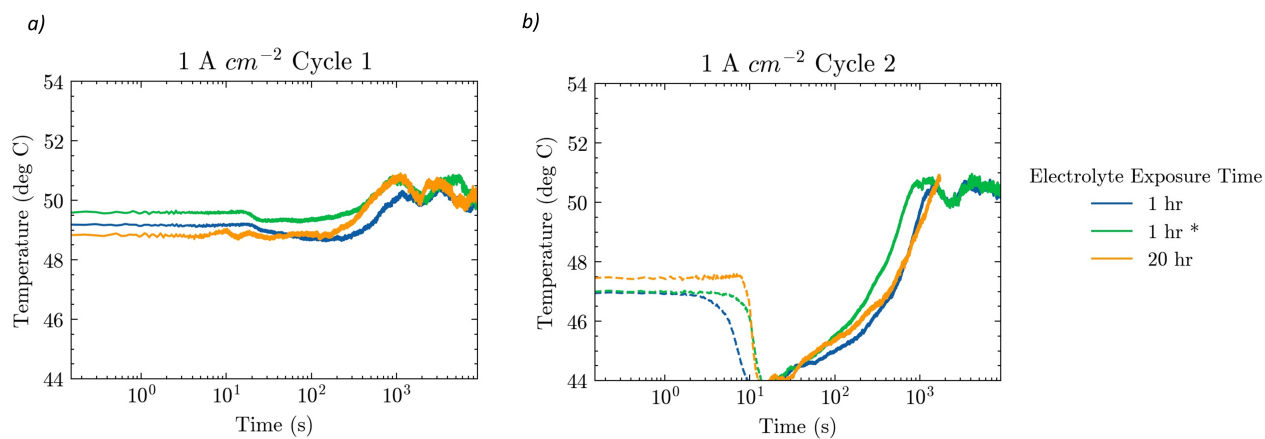


Figure E.1: The temperature of the long-duration test at 1 A cm^{-2} aimed at 50°C . Panel (a) displays the first cycle, and panel (b) the second one. The electrolyte exposure time is either 1 hour or 20 hours. The * denotes a duplicate test.

F

Pourbaix Diagrams of Impurities

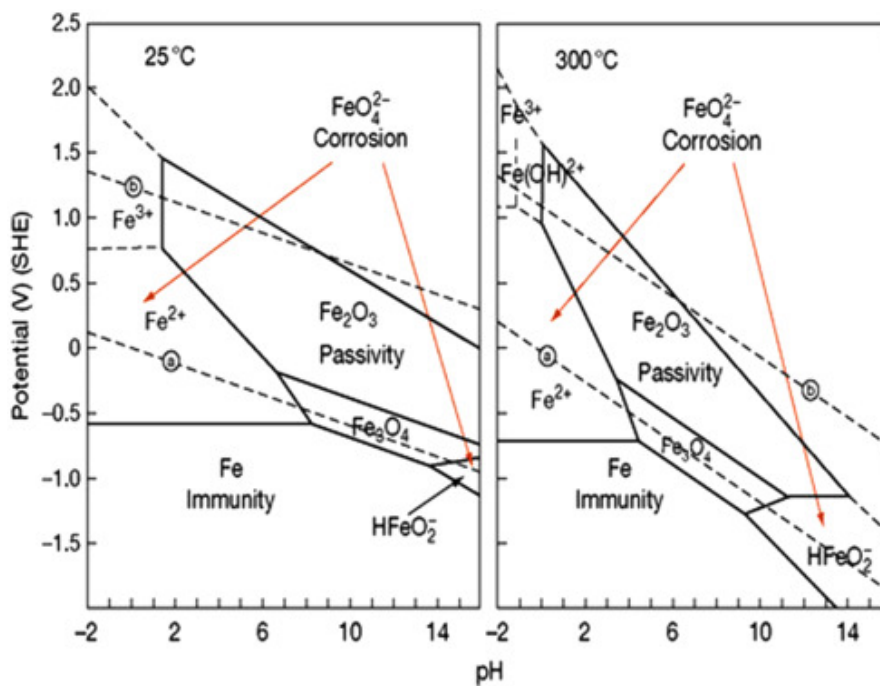


Figure F.1: Pourbaix diagram of iron in an aqueous environment at 298.15 K (left) and 573.15 K (right). Source: Richardson et al., 2018 [70].

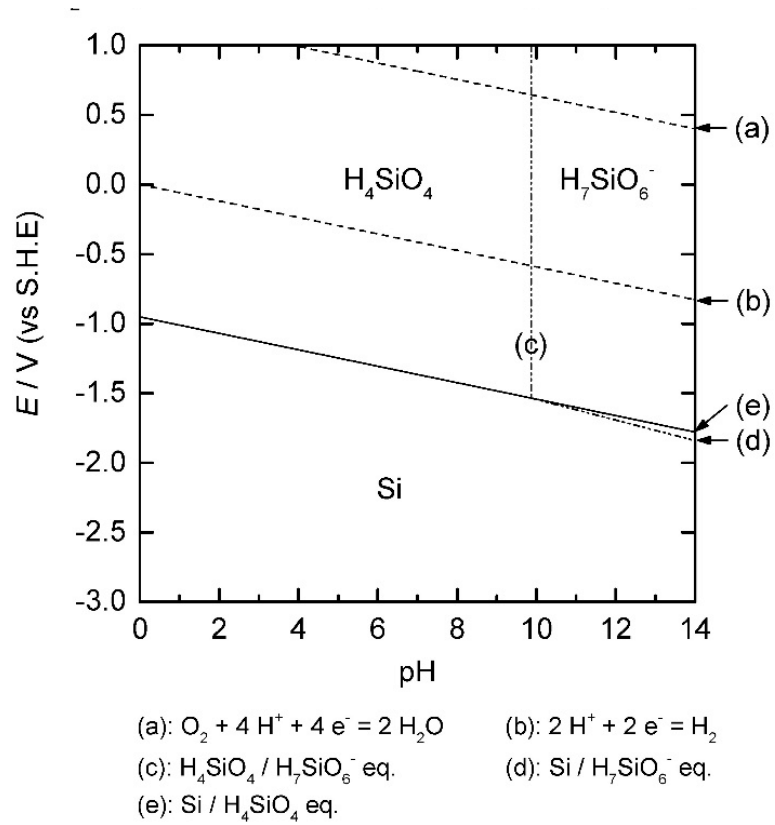


Figure E2: Pourbaix diagram of silicon in an aqueous environment at 298.15 K. Source: Choi et al., 2020 [71].

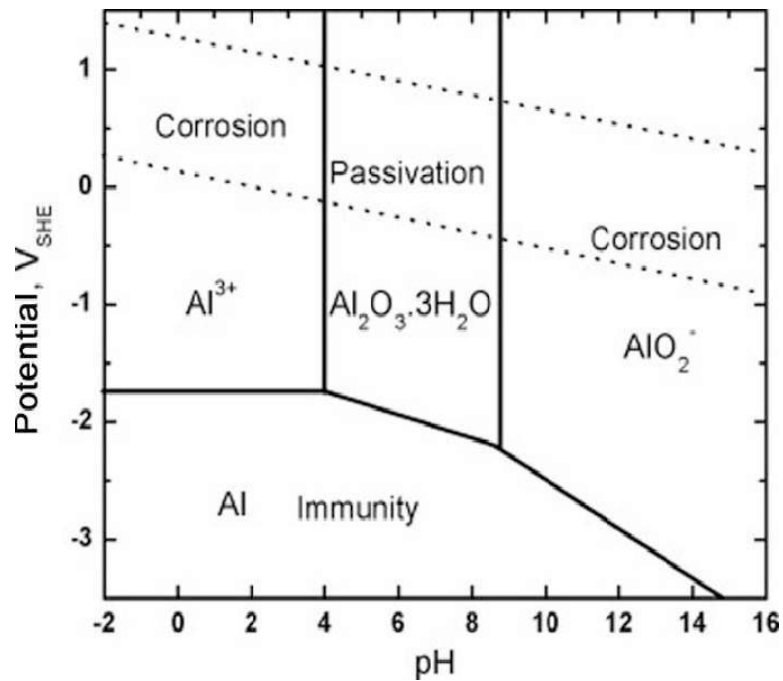


Figure E3: Pourbaix diagram of aluminium in an aqueous environment. Source: Fousova et al., 2019 [72].

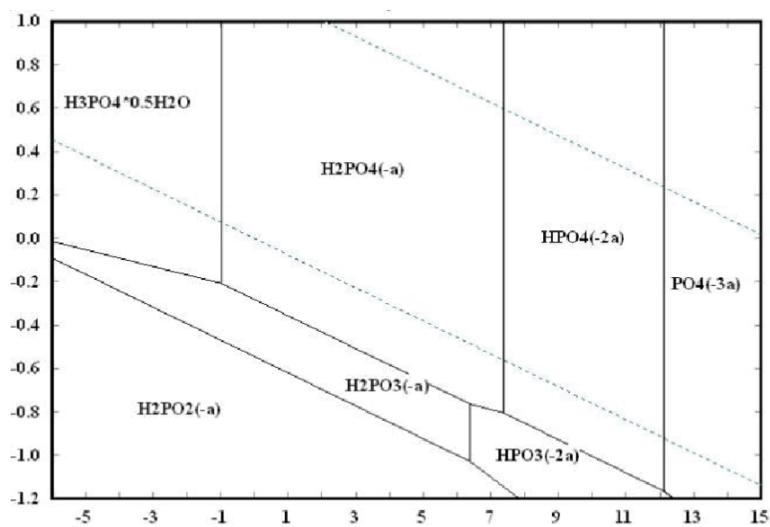


Figure E4: Pourbaix diagram of phosphorus in an aqueous environment at 298.15 K. Source: Haghani et al., 2020 [73].

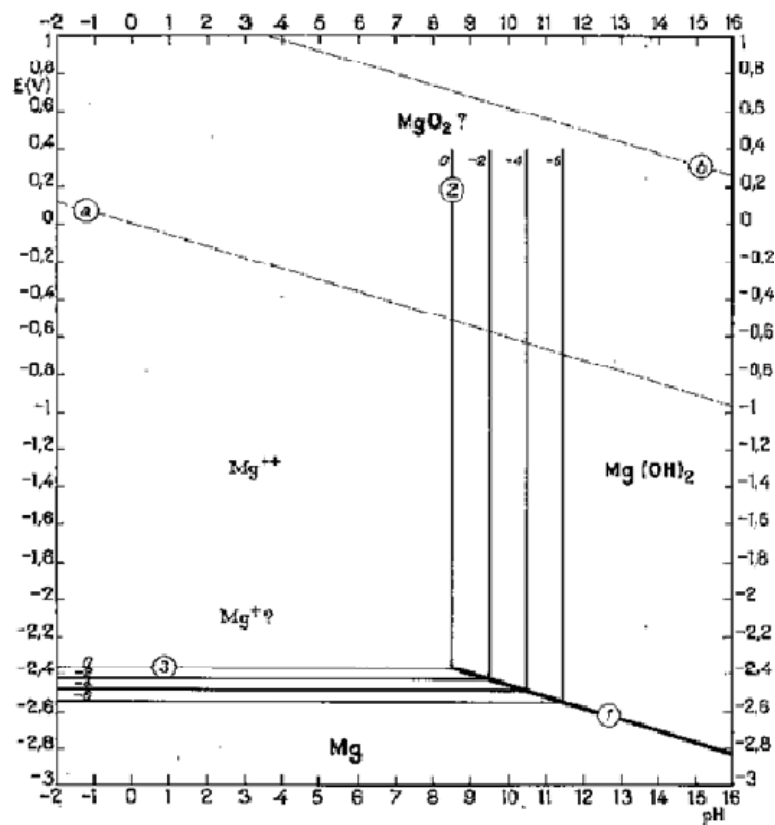


Figure E5: Pourbaix diagram of magnesium in an aqueous environment at 298.15 K. Source: Salahshoor et al., 2012 [65].

G

XRD Results

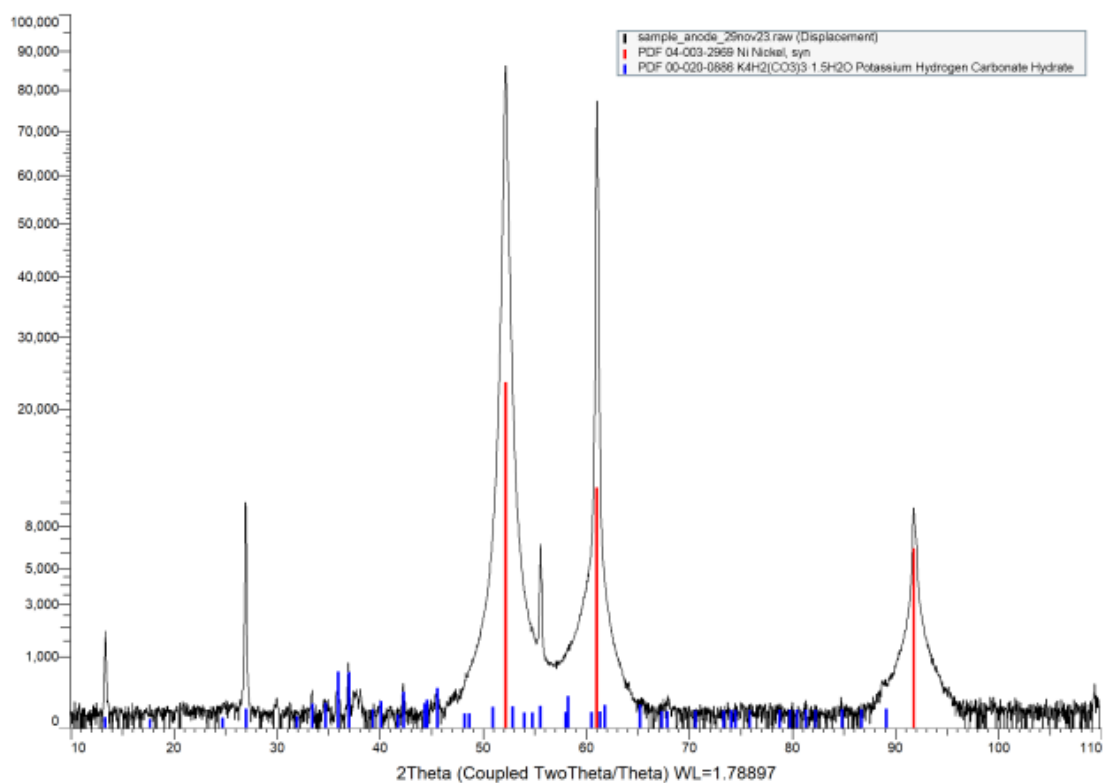


Figure G.1: XRD results of the anode of the 1 hr aged duplicate (*) exposed to the galvanostatic long duration test at 1 A cm^{-2} .

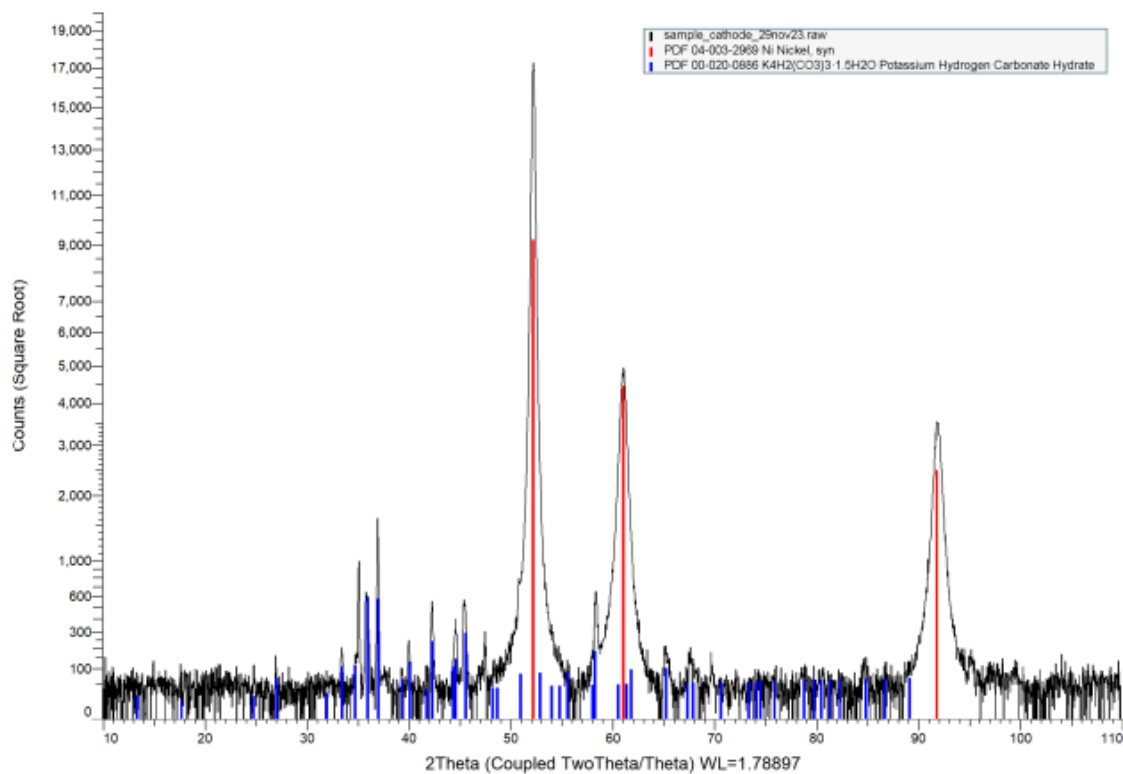


Figure G.2: XRD results of the cathode of the 1 hr aged duplicate (*) exposed to the galvanostatic long duration test at 1 A cm^{-2} .

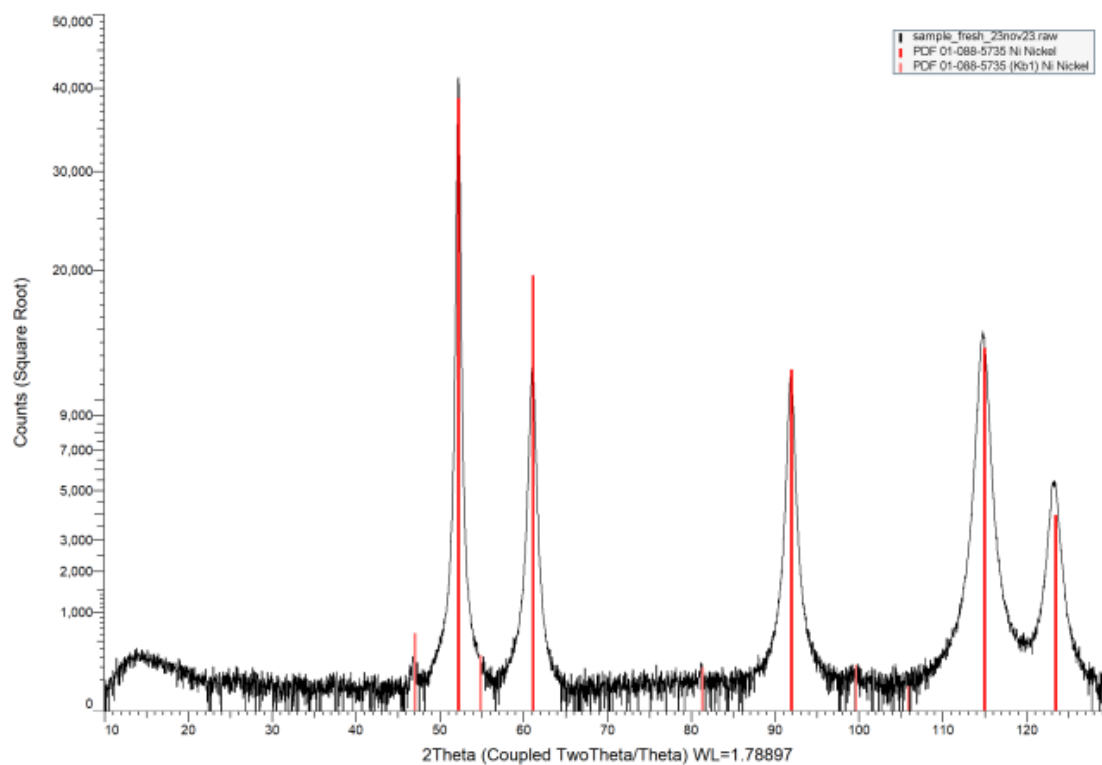


Figure G.3: XRD results of fresh nickel electrode material.

H

SEM Results

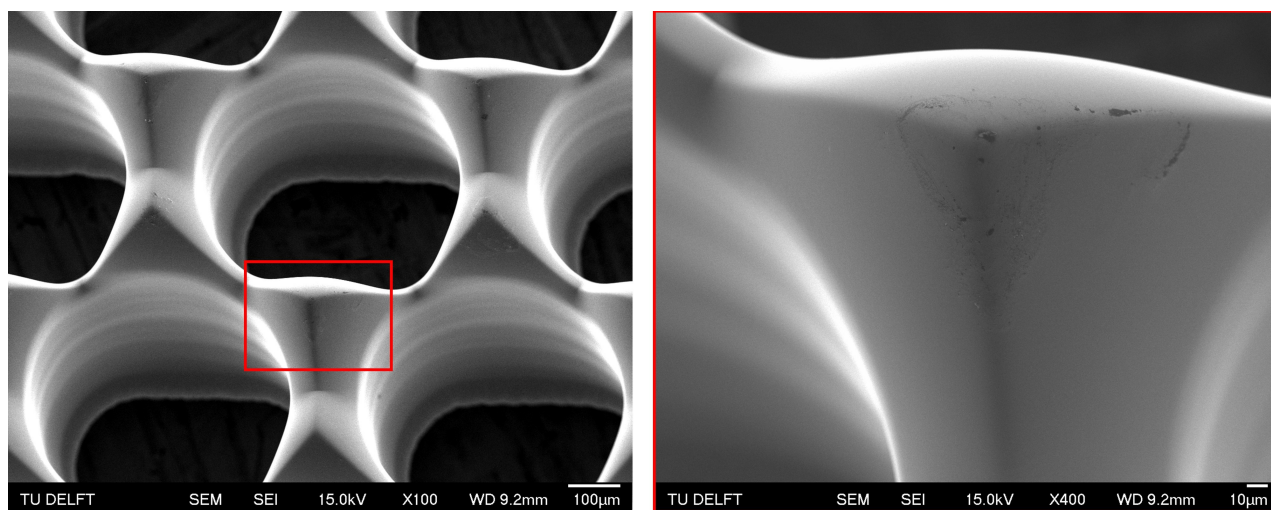


Figure H.1: SEM images of the pillar side of the fresh electrode material at different magnifications. Left: Overview at x100. Right: Zoomed-in view at x400, highlighting the region outlined in red on the left image.

Additional Electrochemical Results

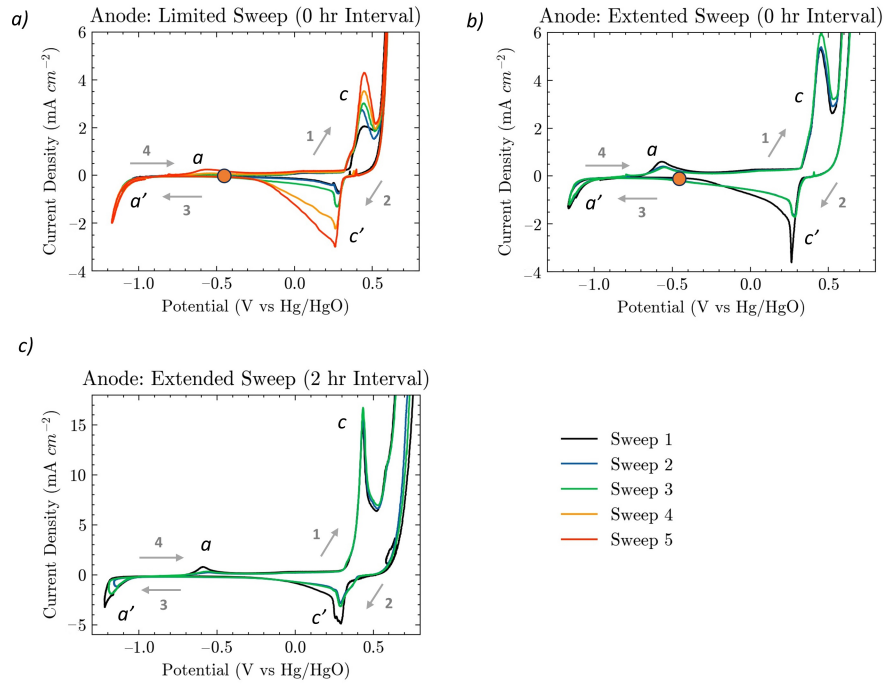


Figure I.1: Cyclic voltammograms of the anode. Subfigure (a) depicts CVs measured before any electrolysis interval at a limited range up to 0.67 V vs. Hg/HgO. Subfigure (b) illustrates CVs before any electrolysis interval at an extended range above 2 V vs. Hg/HgO. Subfigure (c) depicts CVs measured after four 0.5 hr electrolysis intervals at an extended range above 2 V vs. Hg/HgO. The numbered arrows denote the sequence of the sweeps.

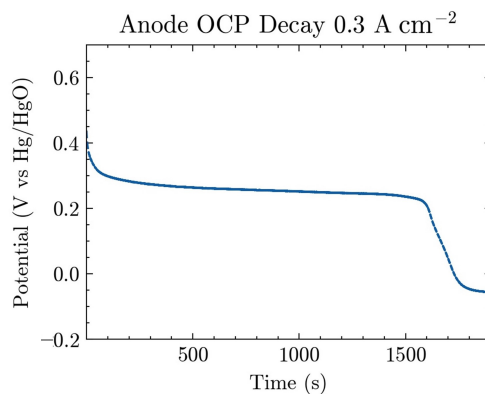


Figure I.2: Anode potential development after the second 2.5-hour charging cycle at 0.3 A cm^{-2} , transitioning to open circuit conditions by removal of the current. Conducted at 50°C with 30 wt% KOH, as detailed in Section 3.2.1. The potential drop indicates a sudden change in the surface phase.

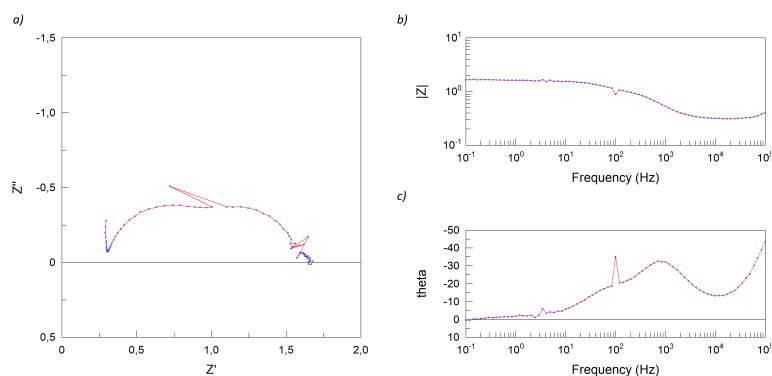


Figure I.3: Impedance data of the first cycle during the interval test at 0-hour electrolysis interval before removing data that does not comply with Kramer-Kronig criteria. Data is presented in (a) Nyquist plot and (b) Bode plots showing the magnitude of impedance and (c) phase angle. Current density: 0.05 A cm^{-2} . AC amplitude: 0.5 mA cm^{-2} .

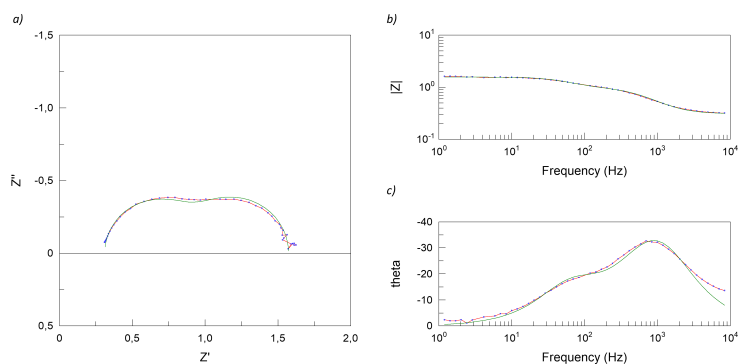


Figure I.4: Kramers-Kronig compliant impedance data of the first cycle during the interval test at 0-hr electrolysis interval presented in (a) Nyquist plot (b) and bode plots with magnitude of the impedance (c) and the phase angle. Current density: 0.05 A cm^{-2} . AC amplitude: 0.5 mA cm^{-2} .

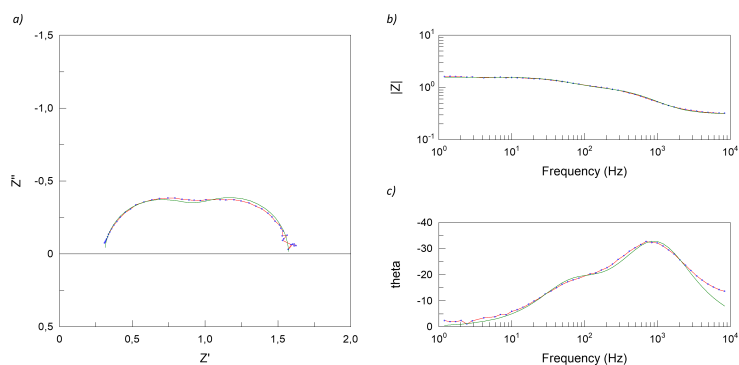


Figure I.5: Kramers-Kronig compliant impedance data of the first cycle during the interval test at 0.5-hr electrolysis interval presented in (a) Nyquist plot (b) and bode plots with magnitude of the impedance (c) and the phase angle. Current density: 0.05 A cm^{-2} . AC amplitude: 0.5 mA cm^{-2} .